Title
Mathematical Modeling of Disease Dynamics, Opinion Dynamics, and Environmental Crimes

Author
Peng, Kaiyan

Publication Date
2022

Peer reviewed|Thesis/dissertation

UNIVERSITY OF CALIFORNIA
Los Angeles

Mathematical Modeling of Disease Dynamics, Opinion Dynamics, and Environmental Crimes

A dissertation submitted in partial satisfaction
of the requirements for the degree
Doctor of Philosophy in Mathematics

by

Kaiyan Peng

2022

ABSTRACT OF THE DISSERTATION

Mathematical Modeling of Disease Dynamics, Opinion Dynamics, and Environmental Crimes

by

Kaiyan Peng
Doctor of Philosophy in Mathematics
University of California, Los Angeles, 2022
Professor Andrea Bertozzi, Co-Chair
Professor Mason Alexander Porter, Co-Chair

Mathematical models can be very useful for improving understanding of human behavior and helping forecasting it. In this thesis, we develop and explore three models of human dynamics. One is a model of disease spread coupled to opinion dynamics, another is a model of opinion dynamics, and the third is a model of illegal logging. We build models in the form of dynamical processes on networks for the first two applications and employ optimal control theory to study the third application.

We first introduce a network model of the spread of a disease under the influence of the spread of competing opinions. We describe the network structure in this model as a two-layer multilayer network. On one layer, two opinions — pro-physical-distancing and anti-physical-distancing — spread concurrently and compete with each other. On the other layer, the disease evolves and individuals are less likely (respectively, more likely) to become infected if they adopt the pro-physical-distancing (respectively, anti-physical-distancing) opinion. We explore both beneficial and harmful effects of the spread of opinions on disease transmission

with mean-field approximations and direct numerical simulations. We also examine how heterogeneous networks with specified interlayer and intralyer degree–degree correlations influence the dynamics.

We then develop an opinion-dynamics model that extends the majority-vote model to two-layer multilayer networks with community structure. We assume that neighbors from different social relationships have different abilities to change an individual's opinions. We find three patterns of steady-state opinion distributions and study phase transitions in the model with a mean-field approximation and direct numerical simulations.

Finally, we study a model of the behavior of uncontrolled loggers in the presence of law-enforcement agencies. We assume that loggers want to maximize a profit function that incorporates the benefit of logging, travel cost, and the the risk of capture by finding optimal travel trajectories and optimal logging duration. We formulate the problem as a static Hamilton–Jacobi equation, which we solve using a fast sweeping method. We use Brazilian rainforest data and demonstrate the importance of geographically targeted patrol strategies using numerical experiments.

The dissertation of Kaiyan Peng is approved.

Luminita Aura Vese

Deanna M. Hunter

Mason Alexander Porter, Committee Co-Chair

Andrea Bertozzi, Committee Co-Chair

University of California, Los Angeles

2022

To my parents

TABLE OF CONTENTS

LIST OF FIGURES

LIST OF TABLES

ACKNOWLEDGMENTS

I am extremely grateful to my incredible advisors, Andrea Bertozzi and Mason Porter, for their guidance and help. Thank you to Andrea for introducing me to many interesting projects. The amazing undergraduate research experience with Andrea was one of the most important reasons that I came to UCLA for my graduate study. Thank you to Mason for being enormously supportive and caring. Thank you for spending so much time and effort in discussing research ideas with me, teaching me scientific writing, and providing detailed comments on manuscripts.

I would like to thank all of my collaborators. I am fortunate to have Christian Parkinson lead my first research project in UCLA and continuously be a great mentor in my subsequent project. I am grateful about everything I learned from working with him. Thank you to Michael Lindstrom and Chuntian Wang for valuable insights that helped so much in improving the quality of my work. Thank you to Bohan Chen, Raymond Chu, Yixuan (Sheryl) He, Vanessa Lin, Zheng Lu, and Joseph McGuire who worked with me on various projects. It was great fun working with all of you.

I would like to thank my committee members Luminita Vese and Deanna Needell for their valuable suggestions and insights. I would like to thank Maida Bassili, Brenda Buenrostro, Martha Contreras, and Corinne Smith for providing administrative support.

I am grateful for funding support from National Science Foundation's Rapid Response Research (RAPID) Grant DMS-2027438 and from National Science Foundation Grants DMS-1737770, DMS-1922952, and DMS-2027277 through the Algorithms for Threat Detection program.

Thank you to all of my friends. I would like to thank Xia Li and Siting Liu for friendship and support. You made my Ph.D. journey much more fun. I thank Bon-soon Lin for helping with the basic qualifying exam. I thank Joel Barnett, Bohan Chen, Yurun Ge, Ziheng Ge, Dominic Yang, and many other Ph.D. students at UCLA for their help and fun times.

Finally, I would like to thank my family for their unwavering love and support. Special thanks to my cousin, Yanyan, my best friend and my academic and career mentor, who has been by my side for almost every big and small moment in my life. Without your support, I could not have made it this far. Thank you to my loving and enlightened parents, who have been so dedicated to providing me with good education opportunities and have been so supportive during my journey of pursuing my dreams. I love you all.

VITA

2014–2018 B.S. Mathematics, Nanjing University

2018–2020 M.A. Mathematics, UCLA

PUBLICATIONS

Peng, K., Lu, Z., Lin, V., Lindstrom, M.R., Parkinson, C., Wang, C., Bertozzi, A.L. and Porter, M.A., 2021. A multilayer network model of the coevolution of the spread of a disease and competing opinions. Mathematical Models and Methods in Applied Sciences, 31(12), pp. 2455–2494.

Chen, B., Peng, K., Parkinson, C., Bertozzi, A.L., Slough, T.L. and Urpelainen, J., 2021. Modeling illegal logging in Brazil. Research in the Mathematical Sciences, 8(2), pp. 1–21.

LIST OF KEY SYMBOLS

Chapters 2–4

N	Number of nodes
$\mathbb{P}$	Degree distribution
E	Mixing matrix
r	Assortativity coefficient
β, β^*, $\hat{\beta}$	Transmission rate
γ	Recovery rate
τ	Immunity-loss rate
α	Influence coefficient
S, I, R	Compartments in the physical layer
U, A, P, R	Compartments in the information layer
$\mathcal{U}, \mathcal{A}, \mathcal{P}, \mathcal{R}$	Nodes that adopt U, P, A, R opinion when they are infected
$[X]$	Expected number of nodes in state X divided by N
$\lvert X \rvert$	Cardinality of set X
$X \circ Y$	Edges connecting nodes in state X and state Y
$\mathbf{P}$	Block matrix that specifies edge probabilities for stochastic block models
f_1, f_2	Probability of changing opinions in our majoriy-vote model
μ_l	Strength of intra-layer communities on layer l
ν	Correlation of inter-layer community memberships

Chapter 5

Ω	Geological domain
P	Profit function
$\mathcal{B}$	The abstract benefit function
$\mathcal{C}$	The abstract cost function
$B(x)$	Total value of trees at location x
$d(x)$	Euclidean distance from location x to the closest major highways
$\hat{d}(x)$	Euclidean distance from location x to the closest major highways and waterways
ψ	Capture intensity function
E	Patrol budget
μ	A constant that increases the cost when patrolling deeper into the forest
$t_{\log}$	Logging time
T	Time to clear all trees in one location
τ	Travel time
v	Travel velocity
c, γ	Constants that decrease travel velocity when carrying trees
α	A dimensional function that converts time to monetary value
r, w	Constants that control the level of concentration of patrol strategies
$X_{\text{in}}, X_{\text{out}}$	Paths to and from the logging location
PA	Pristine area ratio
PB	Pristine benefit ratio
WP	Weighted profit

CHAPTER 1

Introduction

Mathematical models, through tractable formulations and rigorous reasoning, can help us understand the fundamental mechanisms of numerous real-world situations, including complex and mysterious human behavior. Through predictions and development of intervention strategies, these models can assist in decision-making and policy-making and help address social issues, mitigate disease impact, boost economic growth, and even save lives. One way to understand human behavior is by considering how humans interact with other humans, social environments, and natural environments. In this thesis, we propose models of human activities in two applications. In Chapters 3 and 4, we study the spread of opinions and infectious diseases through network analysis. Chapter 5 concerns modeling illegal logging by focusing on strategic interactions between loggers and law-enforcement agencies.

1.1 Modeling the spread of diseases and opinions on networks

The spread of infectious diseases is a major threat to human health [BC19]. Despite the improvement of medical technology and medical systems, the outbreak of COVID-19, Ebola, Zika, dengue, and other diseases continually reminds us of the vulnerability of human lives. Disease outbreaks also lead to broader social and economic consequences [MFA21]. Meanwhile, due to the ubiquity of digital and social media, the pervasive spread of opinions (especially misinformation and disinformation) affects the mental health of people and can jeopardize democracy and social justice [DBZ16]. This can lead to so-called *infodemics*, which refer to epidemics of information [GVC20, YPH21]. Among the various efforts to combat the

spread of pathogens and misinformation, mathematical models lie at the core of understanding and forecasting spreading mechanisms and patterns [CFL09, DHB12, BCC12, KMS17].

Both the spread of infectious diseases and the spread of opinions arise from interactions between individuals. Network models provide an intuitive framework to represent contact patterns in a mathematically tractable way and to study spreading processes that unfold on top of them [New18]. The study of structural properties of real-world networks (e.g., degree distribution, local clustering, community structure, and so on) and the emergence and evolution of these properties is a major research effort that attracts and benefits from researchers from many different disciplines [Est12, BP16, New18]. The influence of network structure on dynamical processes is heavily investigated [DL94, New18]. Through emphasizing the importance of contact patterns and the heterogeneity of individuals, models that incorporate network structure are more sophisticated and realistic than those that rely on well-mixed populations. These network models are able to showcase many interesting phenomena (e.g., the majority illusion [LYW16], echo chambers [CMG21] and filter bubbles [IDC22] on social media, and super-spreader events [STW06] in disease transmission) and suggest possible mechanisms for them. In Chapter 2, we briefly review structural analysis of networks and dynamical processes on networks.

During the advancement of network science, researchers have realized that using simple graphs is insufficient for modeling various situations. A variety of generalizations of traditional networks have been developed, including so-called multilayer networks [DSC13, KAB14, Man22]. Multilayer networks consist of multiple layers of networks with different layers representing different types of iterations. For example, one can construct a three-layer network with the layers representing friendship/following relationships on Facebook, Instagram, and Twitter, respectively. The contact patterns can be platform-dependent but are correlated. Moreover, information can flow both within or across platforms (i.e., layers). As another example, disease transmissions and human behavior (e.g., whether or not an individual is complying with intervention measures) are inextricably coupled [BSP21]. Because

people can influence others' behavior through online contacts even if they have never physically met, it is appropriate to construct a two-layer network with both in-person and online contacts. These examples reveal the relevance of incorporating multilayer structures when modeling contact patterns and the importance of developing tools and theories for understanding such more complicated systems. In Chapters 3 and 4, we propose two models that build on multilayer networks and study the influence of multilayer structure on dynamics.

In Chapter 2, we give a brief overview of key mathematical ideas in network science, with a focus on definitions, tools, and models that we will use in later chapters. Starting with structural features, we introduce important network measurements to effectively study qualitative features of networks. We then discuss several random-graph models that we use to generate synthetic networks with specific structural features. These models often serve as "substrates" for simulating and studying dynamics on networks. We finish our brief review of the structural side of network science by discussing the generalization of several concepts to multilayer networks. In our subsequent discussion of dynamical processes on networks, we survey classical disease models and opinion models on networks. We then discuss mean-field approximations, which give an approach for obtaining theoretical understanding of dynamical systems on networks.

In Chapter 3, we study a model of disease transmission coupled with opinion spreading. During the COVID-19 pandemic, conflicting opinions on physical distancing swept across social media, affecting both human behavior and the spread of COVID-19. Inspired by such phenomena, we construct a two-layer multilayer network for the coupled spread of a disease and conflicting opinions. We model each process as a contagion. On one layer, we consider the concurrent evolution of two opinions — pro-physical-distancing and anti-physical-distancing — that compete with each other and have mutual immunity to each other. The disease evolves on the other layer, and individuals are less likely (respectively, more likely) to become infected when they adopt the pro-physical-distancing (respectively, anti-physical-distancing) opinion. We develop approximations of mean-field type by gener-

alizing monolayer pair approximations to multilayer networks. These approximations agree well with Monte Carlo simulations for a broad range of parameters and several network structures. Through numerical simulations, we illustrate the influence of opinion dynamics on the spread of the disease from complex interactions both between the two conflicting opinions and between the opinions and the disease. We find that lengthening the duration that individuals hold an opinion may help suppress disease transmission, and we demonstrate that increasing the cross-layer correlations or intralayer correlations of node degrees may lead to fewer individuals becoming infected with the disease. This chapter consists of work that was done in collaboration with Zheng Lu, Vanessa Lin, Michael R. Lindstrom, Christian Parkinson, Chuntian Wang, Andrea L. Bertozzi, and Mason A. Porter in Ref. [PLL21].

In Chapter 4, we investigate a majority-vote model [Lig85] — a type of opinion model — on multilayer networks with community structure [POM09]. In our majority-vote model, each layer represents one social relationship and an individual changes their opinion based on the majority opinions of their neighbors in each layer. To capture the fact that different relationships often have different levels of importance, we introduce a layer-preference parameter, which determines the probability of adopting an opinion when different layers have different majority opinions. We build our networks so that each individual is a member of one community on each layer. Individuals tend to have more connections with people from the same community than with people from different communities. We study how the correlation of memberships across layers influences the formation of consensus. Through numerical simulations, we find that when individuals who belong to the same community in one layer tend to belong to the same community in other layer(s), different communities may ultimately have different mean opinions. As the correlation decreases, each community may ultimately have the same mean opinion. We develop mean-field approximations of the dynamical system and reveal critical conditions where there is a transition between the above two behaviors.

1.2 Modeling illegal logging

Deforestation is a major threat to global environmental wellness [Fea05, MRB08, LV15], with illegal logging as one of the major causes [Reb13]. Recently, there has been increased effort to model environmental crime, with the goal of assisting law-enforcement agencies in deterring these activities [FJT13, KFD15, FNP17, KFG17]. In Chapter 5, we present a model for illegal logging that is applicable to regions of arbitrary geometry. We model the practice of loggers in the presence of law-enforcement agencies using tools from multiobjective optimal control theory and consider non-instantaneous logging events and load-dependent travel velocity. We calibrate our model using real deforestation data from the Brazilian rainforest and demonstrate the importance of geographically targeted patrol strategies. This chapter consists of work that was done in collaboration with Bohan Chen, Christian Parkinson, Andrea L. Bertozzi, Tara Lyn Slough, and Johannes Urpelainen in Ref. [CPP21].

CHAPTER 2

Background on Structural Analysis of Networks and Dynamical Systems on Networks

2.1 Networks

A network is a natural approach for modeling relationships between entities [New18]. The simplest type of network is a *graph* $G = (V, E)$. We also call this type of networks *monolayer networks*. The entities V (e.g., humans, websites, airports, neurons, and so on) are called *nodes* or *vertices*. The pairwise relationships $E \subseteq V \times V$ (e.g., friendship relationships, citation relationshisp, direct flight connections, and so on) are given by *edges*, which connect two vertices. In its simplest form, the existence or absence of an edge corresponds to the existence or absence of a relationship. One can use directed edges to encode asymmetric relationships [BG09] and associate edges with weights to model connection strengths [BBP04]. Because networks lie at the heart of numerous complex systems (e.g., human societies, transportation systems, neural networks, and so on), there is considerable interest in network science from the social, physical, biological and information sciences and the development of network science has borrowed ideas from all of these fields [Bar05, BP16, New18]. In the rest of this section, we briefly discuss several basic network structures and representative random-graph models that we use in Chapter 3 and Chapter 4. We then discuss multilayer networks, which are generalizations of ordinary networks.

2.1.1 Network structures

Network measurements can yield important insights into the functionality, history, and future evolution of networked systems. Network structures can be described from local (e.g., nodes and edges), global (e.g., degree distribution and diameter) and mesoscale (e.g., community structure [POM09, FH16] and core–periphery structure [RPF17]) perspectives [New18].

The most basic measure is the *degree* of a node, which is defined as the number of edges that are attached to the node. A network can have a wide range of degrees. For example, at the time of writing this thesis, the most followed account on Twitter is @BarackObama, which has about 130 million followers. The *degree distribution*, which is a probability distribution $\mathbb{P}(k)$, describes the fraction of nodes with degree k. Alternatively, $\mathbb{P}(k)$ represents the probability that a uniformly randomly chosen node has degree k. Many real-world networks possess a heavy-tailed degree distribution [BA99, CSN09], with a small number of entities having a large number of connections.

Node degrees are sometimes correlated with the existence or absence of edges [New18]. Many nodes in a network are connected preferentially to other nodes of similar degrees. This pattern is called *assortative mixing by degree* [New02, NG03] or simply *assortativity*. Conversely, networks can be mixed disassortatively by degree if large-degree nodes tend to be adjacent to small-degree nodes. To quantify assortativity, we use a *degree–degree correlation matrix* E (which is also called a *mixing matrix*) that specifies the joint distribution of degrees at both ends of an edge that we choose uniformly at random. Given a mixing matrix E, the degree distribution is $\mathbb{P}(k) = \left(\sum_{k'} \frac{E_{k,\,k'}}{k}\right) \Big/ \left(\sum_{k,\,k'} \frac{E_{k,\,k'}}{k}\right)$. For a network with N nodes, the expected number of edges that connect nodes with degrees k and k' is $\mathcal{E}_{k,\,k'} = E_{k,k'} \sum_k (k p_k) N/2$. In Chapter 3, we investigate how assortativity can influence the dynamics.

One of the most commonly studied mesoscale structures is *community structure* [POM09, FH16]. Loosely speaking, a community is a set of nodes in a network that are densely con-

nected to each other and have few connections to the rest of the network [New18]. Communities are ubiquitous in social networks and biological networks. The existence of community structures is closely related with network functionality [BP16] and can affect how opinions and diseases spread. In Chapter 4, we generalize community structure to multilayer networks and investigate its influence on an opinion model called the majority-vote model [Lig85].

2.1.2 Random-graph models

A *random-graph model* defines a distribution over possible networks in which some network properties are fixed and the networks are random in other aspects [New18]. Random-graph models are important tools for studying the emergence of network structures and for understanding dynamical processes on networks [Gre21]. In the following paragraphs, we discuss several popular random-graph models that we use in later chapters.

The *Erdős–Rényi (ER) network model* [SR51, ER59, ER60, ER61] is one of the simplest random-graph models and is sometimes called simply "the" random graph. An ER network $G(N, p)$ is an ensemble of networks with N nodes in which every pair of distinct nodes is connected with uniform, independent probability p. In contrast to common observations from real networks, the expected degree distribution of an ER network approximately follows a Poisson distribution when N is large.

A *configuration-model network* [FLN18] overcomes the shortcoming of the unrealistic degree distribution of the $G(N, p)$ ER model and offers the flexibility of configuring degree distributions. In one version of a configuration-model network, one specifies a degree sequence. A configuration model defines a uniform distribution over all networks with the given degree sequence. Sometimes, we are interested in a specific degree distribution instead of a degree sequence. In this case, we first sample degree sequences from the degree distribution of interest and then generate random graphs with the sampled degree sequences. There are many ways to generalize configuration models. In Chapter 3, we generate networks with degree–degree correlations using a generalized configuration-model network.

A *stochastic block model* (SBM) [HLL83, Pei19] is a common generative model for introducing modules (such as communities) into networks. The simplest type of SBM generalizes ER networks by assigning nodes to disjoint groups (e.g., communities) and sampling edges based on group labels. More specifically, one defines a matrix $\mathbf{P}$, where $\mathbf{P}_{i,j}$ represents the probability that a node in group i is adjacent to a node in group j. The *planted-partition model* is a special type of SBM with $\mathbf{P}_{i,i} = \mathbf{P}_{\text{in}}$ and $\mathbf{P}_{i,j} = \mathbf{P}_{\text{out}}$ for $i \neq j$. In our numerical experiments in Chapter 4, we consider $\mathbf{P}_{\text{in}} = 3\mathbf{P}_{\text{out}}$, so that nodes are much more likely to be adjacent when they belong to the same group than when they belong to different groups. Therefore, the constructed networks have strong community structure.

2.1.3 Multilayer networks

In most social and natural systems, the relationships between entities are time-dependent and multiplex. To improve our understanding of such complicated systems, it is useful to consider network structures that are more elaborate than ordinary graphs. A *multilayer network* [KAB14, AM19] has layers in addition to nodes and edges; different layers encode different types of interactions. A node can exist in one or multiple layers. The instantiation of an entity in a layer is called a *state node*. The set of all state nodes of the same entity corresponds to a *physical node*. In the most general form, any two state nodes can be connected. The *interlayer edges* (i.e., edges that run across layers) introduce new structural correlations between the layers and introduce a fundamental feature that is absent in monoplayer networks. In this thesis, we focus on a special type of multilayer networks, called *multiplex networks*, in which interlayer edges can only connect state nodes that correspond to the same physical node. Edges in different layers (i.e., *intralayer edges*) can form different patterns. For example, a node can have different neighboring nodes in different layers and the number of neighboring nodes can also be different. The patterns of edges in different layers can depend on each other [PHP20]. There has been a lot of work on generalizing concepts from monolayer networks to multilayer networks [AM19]. For example, a variety

of random-graph models of multilayer networks have been proposed [KBS16, BJA20].

2.2 Dynamical processes on networks

One fundamental reason for the huge interest in network analysis is the inextricable coupling between network structures and dynamics on networks. The importance of network structures to dynamical processes has long been recognized [DL94], and there has been extensive research on how contact patterns can shape the spread of infectious diseases [PCV15], social dynamics [CFL09], percolation processes [LLL21], synchronization of coupled oscillators [DB14, RPJ16], and so on. Dynamical processes can also affect the dynamics of a network [GB08]. For example, a person may stop following a Twitter account because of disagreement with that account's viewpoint. Likewise, they may start to follow other accounts and even actively retweet the content from those accounts because they share similar views. In this thesis, we only consider time-independent networks for simplicity. However, time-evolving networks are often a more accurate way to model real situations. To study the behavior of a dynamical process, it is common to study them on random graphs. By simulating dynamical processes on random graphs and real-world networks, one can observe discrepancies between different dynamical processes and explore what network structures are essential for certain dynamical processes.

With the importance of network structure in mind, we now discuss the modeling of dynamical processes. One first defines a set of possible states of each node. The state of a node can take a discrete value (e.g., individuals can be either susceptible or infected) or a value in a continuous space (e.g., an individual's political ideology is a real number between -1 and 1). After assigning each node an initial state, one needs to specify how node states update with time. The state evolution with time can be either discrete or continuous. State changes may be spontaneous (e.g., self-recovery from illness) or arise from contacting one or more neighbors or other sources of influence (e.g., people may change opinions because

of media broadcasts). When making such choices, one needs to balance model complexity and tractability. For example, modeling opinions as taking discrete values is typically an oversimplification, but discrete-valued opinions is generally easier to analyze than continuous-valued opinions. Therefore, we consider discrete opinion states in this thesis. We discuss typical models of disease dynamics and opinion dynamics in Section 2.2.1 and Section 2.2.2, respectively. In Section 2.2.3, we discuss mean-field calculations, which are commonly used to approximate the population-level behavior of dynamical processes.

2.2.1 Disease dynamics

The mathematical modeling of the spread of infectious diseases has a long history [AM92, PCV15, KMS17]. In the most common type of model, it is assumed that individuals are assigned to different *compartments* and that people in the same compartment are in the same state [AM92, BCC12]. For example, people can be susceptible or infected, which we denote by S and I, respectively. Depending on the nature of the disease, people who are infected are not necessarily infectious. However, in this thesis, we treat infected and infectious states as the same for simplicity. The recovered or removed compartment (which we denote by R) is another commonly used class; it includes individuals who either have recovered or have died after contracting a disease and are thus removed from disease transmission. Other compartments (e.g., an asymptomatic state) can also be included to make models more realistic. Transitions between different states govern disease transmission and recovery. They are best described as stochastic events and are often assumed to follow a Poisson process for simplicity [Dur19]. Under this assumption, one obtains a system that possesses the Markovian property [Lig10]. With the Markovian assumption, a continuous-time formulation of a model of disease spread assumes that a susceptible individual contracts a disease from an infectious neighbor at rate β, which is called the *disease transmission rate*. The probability that an individual is infected by a disease depends on the number of their infectious neighbors. It is thus important to incorporate contact patterns into models of disease spread. An

infected individual recovers spontaneously with rate γ, which is called the *recovery rate*. It is usually assumed that the transmission rate and the recovery rate are time-independent.

Classical works on disease transmission assume that the population in which the disease spreads is fully mixed, which means that each individual has an equal probability to contact any other individual in the population [AM92, BCC12]. In these classical models, one tracks the evolution of the expected number of individuals in each compartment. This approach leads to a deterministic system that can be described by a small set of coupled ordinary differential equations (ODEs). As an example, the population-level deterministic equations for the susceptible–infected–recovered (SIR) process [KM27] is

$$\begin{aligned} \frac{d}{dt}[|S|] &= -\beta[|I|][|S|]\,, \\ \frac{d}{dt}[|I|] &= \beta[|I|][|S|] - \gamma[|I|]\,, \\ \frac{d}{dt}[|R|] &= \gamma[|I|]\,, \\ [|S|]+[|I|] + [|R|] &= 1\,, \end{aligned} \tag{2.1}$$

where we use $|\cdot|$ to denote cardinality and $[X] = \mathbb{E}[X]/N$ is the expectation of the random variable X divided by the population size N. Equation (2.1) demonstrates one type of mean-field approximation, which we will discuss further in Section 2.2.3. An essential question about disease models is whether or not an epidemic outbreak will occur. From (2.1), the early-time behavior of the I compartment is approximately $I(0)e^{(\beta-\gamma)t}$; at early times, the number of infected people grows exponentially if $\beta/\gamma > 1$. This observation connects the quantity β/γ, which is the *basic reproduction number* for (2.1) and is commonly denoted by R_0, with the concept of an *epidemic threshold*. The basic reproduction number R_0 measures the mean number of secondary infections that arise from a single infectious individual in a fully susceptible population [DHM90, BCF19]. An epidemic outbreak occurs, with a finite fraction of an infinitely large population becoming infected, if $R_0 > 1$. Other models of disease spread also have epidemic outbreak thresholds and basic reproduction numbers. The

expressions for these quantities depend on the parameters of the dynamical processes and on the parameters of contact patterns.

In a real contact network, infected individuals may run out of susceptible neighbors and susceptible individuals may differ in infection risk because of heterogeneity in the number of contacts. Therefore, the assumption of a fully-mixed population is typically inadequate. It is necessary to include a faithful representation of contact patterns to obtain a better understanding of how diseases spread. In recent years, the pervasive use of Bluetooth, Wi-Fi, sensors, and mobile phones [CBB10, SVB11, SSL19] and the advancement of computation power have changed how one can measure contact and mobility networks. The availability of abundant data have supported and advanced research on agent-based disease-transmission models [MAP11, LAA18, ZLL20].

To incorporate contact networks, we represent each individual as a node and encode contacts with edges. Each node has a state that corresponds to membership in a compartment. For simplicity, we again assume that the system is Markovian. For example, in an SIR process, we assume that transmission from an infected node to a susceptible node occurs across an edge as a Poisson process with rate β that is independent of all other nodes and an infected node recovers (or is removed) as an independent Poisson process with rate γ. It is straightforward to simulate such a model using a Gillespie algorithm [KMS17], which is a well-known algorithm for performing continuous-time simulations of Markov processes. The Poisson-process assumption leads to more mathematical tractability than other general processes but there has also been many works on studying non-Markovian disease dynamics on networks [MGK13, RVK16, SGB17]. It is challenging to develop theoretical understanding of network models because the state space is very high-dimensional. There have been works that provide exact understanding of the dynamics of some models by using the Markov-chain theory [STK11, VC12]. A mean-field approach [Kue16, KMS17], however, can be applied to a broader range of models and provides a more general framework for studying dynamics on networked systems. We discuss mean-field approximations in Section 2.2.3.

Compartmental models of disease spread have also been applied to studies of many other phenomena. There is a large body of work on the spread of social phenomena [LA18], including the dissemination of information and the adoption of behaviors, which are often modeled as contagion processes that are similar to disease spread [GN64, BCK06, GGA14]. See [WMA13, HL14] for discussions of when social contagions resemble and do not resemble contagions of infectious diseases. Although the basic mechanisms for different spreading phenomena can be different, interactions between peers tend to strongly influence the dynamics that unfold on a network in all cases. By introducing ideas from classical disease models to other fields, one can take advantage of our understanding of existing models. In Chapter 3, where we study the coupled evolution of disease and opinion dynamics, we model the spread of opinions with a compartmental model that is similar to an SIR model. Having both the disease dynamics and the opinion dynamics share similar mathematical descriptions simplifies the mathematical analysis.

2.2.2 Opinion dynamics

Although compartmental models for disease transmissions are well grounded in real-life phenomena, much less is known about how to best model opinion dynamics [CFL09]. How individuals contract and recover from a disease follows a relatively simple and standard pattern. By contrast, the possession of an opinion is extremely complicated and much is unknown about how individuals change their opinions due to the influence of others. This complexity poses great difficulties for modeling the "microscopic" behavior of individuals (i.e., the mechanisms of changing opinion states). Consequently, most of the models of opinion dynamics are theoretical models that rely on huge simplifications and are often justified primarily by vague arguments; they lack empirical validation [CFL09, PKI22]. Nevertheless, these models still add value to studying opinion dynamics. Although detailed microscopic models are oversimplification of reality, one can still study population-level and community-level features and hope that the models capture important factors that contribute to trends

that we observe in real-life data. The main themes of opinion-dynamics models are the types of interaction mechanisms that promote or hinder the formation of consensus, polarization, fragmentation, extremist opinions, and so on [CFL09, NVT20]. We briefly discuss some of these models.

The *voter model* [CS73, HL75] and its variants are among the most studied models of opinion dynamics. In the standard voter model, each individual holds one of two opinions, which one can label as ± 1. This may describe a yes-or-no situation. At each time step, a pair of adjacent nodes are chosen according to some random process and one node adopts the opinion of the other. Different variants of voter models include variations in how one chooses node pairs, the number of different opinions, and other features. Generally speaking, voter models attempt to model the behavior of imitation, where each individual acts under the pressure of their neighbors. There have been many attempts to generalize or modify the voter model to make it more realistic [Red19]. Some variants include the incorporation of zealots [Mob03, MG05], multi-state opinion spaces [VKR03, CES06], memory [DC07], and inertia [STS08].

Different from standard voter models, which incorporate a local majority opinion in an average sense, the *majority-vote model* [Lig85] employs an explicit majority rule. At each time step, a uniformly randomly chosen node adopts the majority opinion of its neighbors with probability $1 - f$ and adopts the minority opinion with probability f, where f is called the noise parameter. If there is no majority opinion, which can occur if a node's neighborhood has an even number of nodes, the focal node adopts one of the two opinions with an equal probability. There is an order–disorder phase transition at a critical value f_c of the noise parameter [Oli92]; this value depends on network structure [COM03, PM05, LSS08]. A different model with a similar name is the *majority-rule model* [Gal02], which instead assumes that a group of nodes are chosen and that all members of that group adopt the majority opinion of that group. Another interesting model [KLT08] interpolates between a standard voter model and the majority-vote model; it assumes that a node adopts an opinion if at

least a fraction p of its neighbors have that opinion.

The models that we have mentioned thus far assume that opinions take discrete values. This assumption is valid in some applications, but it is inadequate in others. For example, when we describe the political position of a person, instead of classifying them as either on the Left or on the Right, it is often better to incorporate positions that lie between these extremes. In mathematical language, we let the opinion space in this example consist of an interval of numbers. An important concept that is commonly used in continuous-opinion dynamics models is *bounded confidence* [NVT20]. The idea is that two individuals will not influence each other unless their opinions are close enough to each other. Two well-known bounded-confidence models are the *Deffuant–Weisbuch model* [DNA00] and the *Hegselmann–Krause model* [HK02].

2.2.3 Mean-field approximations

Due to the high dimensionality of networked systems, theoretical analysis of dynamical processes on networks often relies on mean-field approximations [PCV15], which focus on examining the dynamics of expectations of population-scaled quantities. Many approximation methods have been developed for dynamics on monolayer networks (i.e., ordinary graphs) [KMS17]. Examples of approaches include edge-based compartmental modeling [MSV12], pair approximations [KRM97], effective-degree approximations [LMD11], and approximate master equations [Gle11, Gle13]. The essence of a mean-field approximation is to find appropriate course-grained quantities of a system (e.g., the number of nodes in each compartment in a model of disease spread) and develop differential equations that describe the evolution of mean values of these quantities. These equations are also called *rate equations* or *moment equations*. When a system of coupled differential equations is high-dimensional (even infinite-dimensional), one uses *moment closure* [Kue16] to approximate higher-order quantities with lower-order quantities to close the system [KMS17]. Different methods can track the evolution of different quantities, rely on different assumptions, and achieve results with

different levels of accuracy. In Chapter 3, we use a pair approximation [KRM97], with which we track the expected number of nodes and edges grouped by degrees and compartments. The dimension of the resulting system of equations scales as K^3, where K is the number of different node degrees. Because K is typically large, the system of equations is very high-dimensional. We rely on numerical methods to solve this system, and it is very hard to study such high-dimensional systems analytically. A key advantage, however, is that the mean-field approach can handle networks with any degree distribution and networks with degree–degree correlations. By contrast, we use a much less granular approximation in Chapter 4. In this approximation, we ignore the degree heterogeneity and only track the expected number of nodes based on their communities and opinions. Because the number of communities in a network is usually much smaller than the number of different nodes degrees, we obtain a small system that allows analytical study of steady states and phase transitions.

CHAPTER 3

Modeling the Coevolution of the Spread of a Disease and Competing Opinions

This chapter is adapted from an original paper [PLL21] that I co-authored with Zheng Lu, Vanessa Lin, Michael R. Lindstrom, Christian Parkinson, Chuntian Wang, Andrea L. Bertozzi and Mason A. Porter.

3.1 Introduction

Since the outbreak of coronavirus disease 2019 (COVID-19), researchers in numerous disciplines have used diverse approaches to analyze the spread of the disease, forecast its subsequent spread under many scenarios, and investigated strategies to mitigate it [Est20, BBC20, Ari22]. As cases of COVID-19 escalated, collective compliance with non-pharmaceutical intervention (NPI) measures were vital for dealing with the COVID-19 pandemic in the absence of effective treatments, vaccines [Per21]. As information — some of which was accurate and some of which was not — flooded social media [GVC20, YPH21], people adopted different opinions about the implementation of NPI measures [ANS21]. These opinions affect human behavior and ultimately also the spread of diseases.

It is important to understand the influence of human behavior on the spread of diseases because these two processes are inextricably coupled [VWB16, BSP21]. Past research has examined whether the spread of information can help contain an epidemic (e.g., through decreased transmission rate, fewer contacts, and/or acquired immunity) by leading to a

smaller disease prevalence and/or a smaller basic reproduction number (and hence a reduced probability of a large disease outbreak) [FSJ10, WAW15]. However, as has been striking during the COVID-19 pandemic [Zar20], how people act on information (and misinformation and disinformation) can also have a negative impact on disease propagation; this undermines the potential benefits of information. For example, there have been many anti-physical-distancing rallies in which protesters flout behavioral intervention measures such as wearing masks and practicing physical distancing. Moreover, such large gatherings can directly cause surges of infections [Gab20].

Motivated by the mixed effects of information and opinion spreading, we study a model in which disease transmission is influenced by two opposing opinions: pro-physical-distancing (which we sometimes write simply as "pro" as a shorthand) and anti-physical-distancing (which we sometimes write as "anti"). Following Ref. [GGA14], we consider a two-layer multiplex network. We model the simultaneous evolution of two competing opinions on one layer of a multiplex network as a contagion process of either susceptible–infectious–recovered (SIR) [KM27] or susceptible–infectious–recovered–susceptible (SIRS) form, with opinion adoption that occurs between susceptible and infectious individuals. Similar models have been proposed for studying competing diseases [KN11, Mil13] and ideas [WXL12]. A disease spreads on the other layer (a physical layer) of the multiplex network; the connections in this physical layer encode in-person social contacts. The disease transmission rate depends on the opinions of the individuals.

In our model, we investigate which opinion has greater influence, which we evaluate based on the disease's final epidemic size (i.e., the number of individuals who catch the disease during the disease outbreak). We generate networks using configuration-model networks [FLN18] and their extensions [MPM14]. We demonstrate complex interactions between the two opinions and (because of ensuing behavioral changes, which lead to changes in the physical layer) between the opinions and the disease. We explore how the influence of opinions is affected by various factors, including opinion-contagion parameters and network

structures.

We derive a mean-field description of our multilayer dynamical system for the expected values of population-scale quantities. We use a degree-based pair approximation [EK02] and generalize it to our multiplex system. As we discussed in Section 2.2.3, in a pair approximation, one examines the various types of pairs in a system and approximates higher-order structures using moment closure [Kue16]. Our approximation scheme incorporates dynamical correlations both within and across the layers of a multiplex network. To capture the influence of opinions on individuals' susceptibility to a disease, we also define effective transmission rates that are time-dependent functions of the distribution of opinions in populations of interest. We develop approximations of the effective transmission rates based on the numbers of various types of pairs. Our numerical simulations reveal that our approximate system is able to capture the influence of the spread of opinions on disease spread for population-scale quantities. We find that the time evolution of the expected numbers of individuals in different states in our pair approximation match very well with simulations on a variety of networks with different degree distributions and degree–degree correlations.

This chapter proceeds as follows. In Section 3.2, we briefly discuss prior work. We present our first model in Section 3.3. In this model, both the spread of the disease and the spread of opinions follow an SIR process. In Section 3.4, we assume that the SIR process occurs in a fully-mixed population, yielding a description of our system in terms of a small set of coupled ODEs. In this ODE system, we observe some influence of opinion dynamics on the spread of the disease, but this framework does not include the effects of social contacts. In Section 3.5, we incorporate social contact structures between individuals to yield a dynamical system on a network. We derive a pair approximation for this network model. In Section 3.6, we conduct stochastic simulations of this network model to investigate the influence of the contagion parameters and network structures on the dynamics of the system. In Section 3.7, we generalize our dynamical system by considering an SIRS process for opinion spreading. We conclude in Section 3.8.

3.2 Related work

To give further context for our work, we briefly mention prior investigations on the coevolution of diseases with behavior, awareness, and/or opinions on multilayer networks [WAW15, VWB16]. In particular, many researchers have examined how the spread of awareness can suppress the spread of a disease. Funk et al. [FGW09] developed a coevolution model in which individuals acquire different levels of awareness of a disease either by becoming infected or by communicating with their neighbors. In their model, individuals are less susceptible to infection by a disease when they have a higher level of awareness. Subsequently, Funk et al. [FGJ10] simplified the above model so that individuals are either aware or unaware of a disease, in analogy to the infectious and susceptible states (i.e., "compartments") of a traditional susceptible–infectious–susceptible (SIS) model of disease spread [BCF19]. A similar model was proposed by Granell et al. [GGA13, GGA14]. Subsequent research has generalized these ideas by modeling the spread of the disease and information using other dynamical systems, such as by modeling disease spread with an SIR model [WTY14] and modeling information transmission with a threshold model [GJL15, GLJ16] or a generalized Maki–Thompson rumor model [SVC19]. Other works have examined the influence of global information and mass media [GGA14, QXU20], the relative speeds of the dynamics of information spread and disease spread [SVC19, VVC20], and heterogeneous risk perceptions of disease spread [PY18, YZR20]. Researchers have also incorporated time-varying networks when studying the combined spread of disease and information, such as by coupling an activity-driven information layer with a time-independent disease layer [GLJ16] or a time-independent information layer with an adaptive physical layer [PZ21]. Additionally, evolutionary game theory has been used to study decision-making in the presence of government-mandated interventions, socioeconomic costs, socioeconomic costs, perceived infection risks, and social influence [YZR21].

Several recent works have examined competing opinion dynamics. Johnson et al. [JVR20]

studied the evolution of anti-vaccine and pro-vaccine clusters of people on Facebook. She et al. [SLS22] examined an opinion model with continuous-valued opinions to study the beliefs of different communities about the severity of disease spread with both cooperative and antagonistic opinion spreading. Epstein et al. [EHC21] used compartmental models to study the fear of infection and the fear of vaccines. Johnston and Pell [JP20] examined the fear of infection and frustration with physical distancing.

3.3 Our model

We study the spread of a disease and two competing opinions on a two-layer multiplex network with one physical layer (where the disease spreads) and one information layer (where opinions spread). We assume that all individuals are present in both layers, and we ignore demographic processes such as birth, death, and migration. We model each layer as an undirected, unweighted, simple graph; we couple the two layers to each other by connecting nodes that correspond to the same individual. Intralayer edges encode in-person contacts in the physical layer and information-exchange channels (especially on social media) in the information layer. In Section 3.6, we give further details about the network structure and we explore the influence of interlayer and intralayer structure on opinion and disease dynamics. In Sections 3.3–3.6, we use SIR dynamics for each process and associate nodes in the physical layer with individuals' health states and nodes in the information layer with their opinions about physical distancing. In Section 3.7, we extend our model by modeling the spread of opinions as an SIRS process. In all versions of our model, we treat each process as a continuous-time Markov chain. We detail how the disease-spread and opinion-spread processes operate and interact in Sections 3.3.1 and 3.3.2. In Table 3.1, we summarize the key parameters of our model.

Table 3.1: Key parameters in our model of coupled opinion adoption and disease spread. In (a), the first column gives the parameters of the opinion dynamics that are related to pro-physical-distancing and the second column gives the parameters that are related to anti-physical-distancing. We use the subscript "info" when the two opinions share parameters; we indicate these parameters in the third column. In (b), each column indicates the parameters of the disease dynamics when individuals adopt the corresponding opinions.

(a) Parameters for dynamics (of opinion adoption) on the information layer

	Pro	Anti	Shared by pro and anti
Transmission rate	β_{pro}	β_{anti}	β_{info}
Recovery rate	γ_{pro}	γ_{anti}	γ_{info}
Immunity-loss rate	τ		

(b) Parameters for dynamics (of disease spread) on the physical layer

Parameter \ Opinion	U or R_{info}	A	P
Transmission rate	β_{phy}	$\alpha_{\text{anti}}\beta_{\text{phy}}$	$\alpha_{\text{pro}}\beta_{\text{phy}}$
Recovery rate	γ_{phy}		

3.3.1 Information layer

Two competing social contagions, which model pro-physical-distancing and anti-physical-distancing opinions, spread concurrently on the information layer. We use P (respectively, A) to denote the pro-physical-distancing (respectively, anti-physical-distancing) state in which individuals both adopt the associated opinion and actively advocate the corresponding behavior. Uninformed (U) individuals are susceptible to both opinions and transition to state P or state A at rates of β_{pro} and β_{anti}, respectively, by communicating with neighbors in the corresponding states. We suppose that people who adopt either behavior can become weary of acting unusually in comparison with life without a disease epidemic, and they then become less passionate about maintaining their current conduct. We assume that individuals in state P and state A transition to the recovered (R_{info}) state at rates of γ_{pro} and γ_{anti}, respectively. After this transition occurs, these individuals practice the same behavior as individuals in the uninformed group, but they are resistant to future influence from neighbors. When the two opinions share the same parameters, we use the subscript "info" (see Table 3.1). We

make the assumption of permanent mutual immunity [KN11]: once an uninformed individual adopts one opinion, it can no longer be influenced by the other opinion. Therefore, upon recovery, it enters state R_{info}. Because the pro- and anti-physical-distancing opinions are opposing opinions, it is reasonable to assume that individuals do not adopt both behaviors simultaneously. We relax the assumption of permanent immunity in Section 3.7. In Figure 3.1, we show a compartment flow diagram of the opinion dynamics.

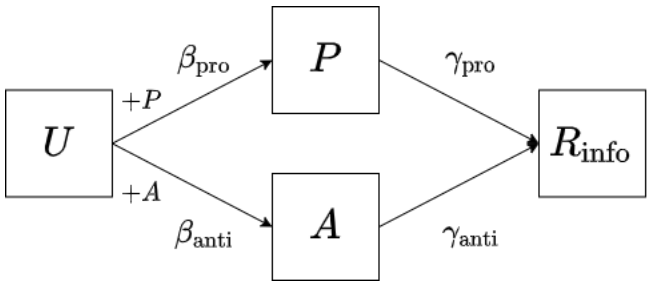

Figure 3.1: Schematic illustration of the (opinion-spreading) dynamics on the information layer of a two-layer multiplex network. There are four states in the information layer: uninformed (U), pro-physical-distancing (P), anti-physical-distancing (A), and recovered (R_{info}). Nodes in state U transition to state P (respectively, A) with a rate of β_{pro} (respectively, β_{anti}) by communicating with neighbors in state P (respectively, A). We use "$+P$" (respectively, "$+A$") to emphasize that state transitions occur under the influence of neighbors in P (respectively, A). Nodes in state P (respectively, A) transition to state R_{info} at a rate of γ_{pro} (respectively, γ_{anti}).

3.3.2 Physical layer

We model the spread of a contagious disease on the physical layer as an SIR-like process. The key difference from a standard SIR contagion is that susceptible nodes have transmission rates that depend on their opinion states [FGW09, GGA13]. We divide susceptible nodes into three types: (1) nodes that do not hold any opinion (i.e., their opinions are in state U or state R_{info}) experience the baseline transmission rate β_{phy}; (2) nodes that hold the pro-physical-distancing opinion experience a reduced transmission rate $\beta_{\text{phy, pro}} = \alpha_{\text{pro}}\beta_{\text{phy}}$, with $\alpha_{\text{pro}} \leq 1$; and (3) nodes that hold the anti-physical-distancing opinion experience an

increased transmission rate $\beta_{\text{phy, anti}} = \alpha_{\text{anti}}\beta_{\text{phy}}$, with $\alpha_{\text{anti}} \geq 1$. We refer to α_{pro} and α_{anti} as "influence coefficients". To model the effects of competing opinions on disease spread, it seems appropriate to study an adaptive network [PG16] in which structure coevolves with node states. For example, individuals who hold an anti-physical-distancing opinion may have more contacts than other people. However, it is difficult to analyze such a model. Therefore, for simplicity, we assume that individuals who hold the anti-physical-distancing opinion in our model have a higher risk of contracting the disease than the baseline through a higher transmission rate. We make an analogous assumption for individuals that hold the pro-physical-distancing opinion. Infected individuals (which we assume to be the same as infectious individuals) recover at rate γ_{phy}. We show the compartment flow diagram of the disease dynamics in Figure 3.2.

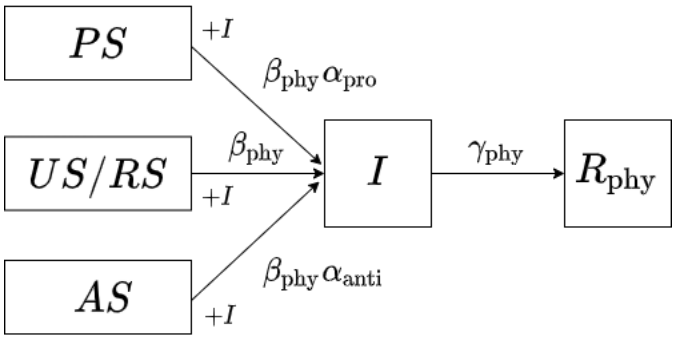

Figure 3.2: Schematic illustration of the (disease-spreading) dynamics on the physical layer of a two-layer multiplex network. There are three states in the physical layer : susceptible (S), infectious (I), and recovered (R_{phy}). Based on the opinion states of the node, we further divide the S state into PS, AS, and US/RS. Nodes in state S transition to state I through in-person social contacts with infectious neighbors (which we emphasize with "$+I$"), with rates that we mark close to the corresponding arrow. Nodes in state I recover at a rate of γ_{phy}.

Combining the dynamics on the two layers, we use two letters to describe the full profile of an individual; the first one indicates a node's opinion state, and the second one indicates its disease state. To simplify our notation, we also drop the subscript for the R compartment, as the order of the two letters in a state already indicates whether we are referring to the opinion

state or the disease state. There are a total of 12 possible states (i.e., compartments). We show the complete compartment flow diagram for our model in Figure 3.3. For convenience, we use the same notation for the state of a node and the set of nodes in a specified state throughout this chapter.

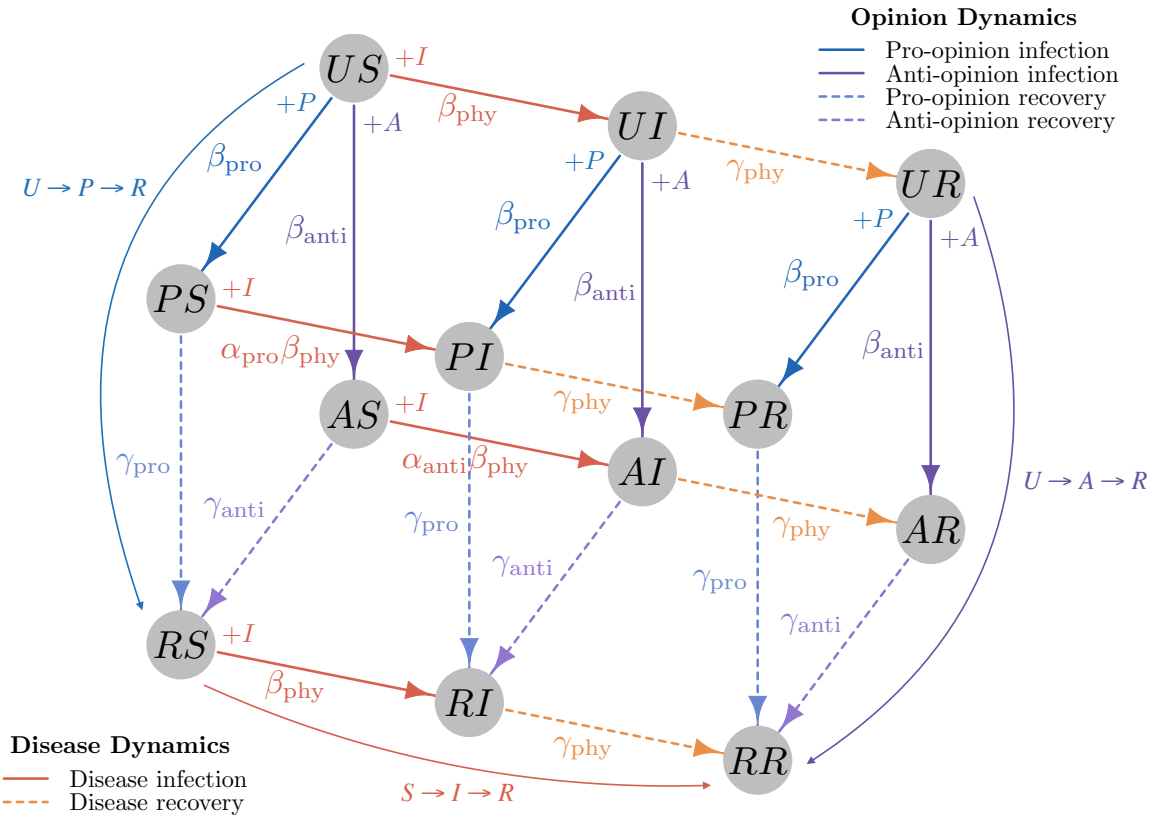

Figure 3.3: Schematic illustration of our model which has dynamics on both information and physical layers. The disks indicate the possible states (i.e., compartments) of a node. In each state, the first letter (U, P, A, or R) indicates the opinion state and the second letter (S, I, or R) indicates the disease state. The arrows mark the possible state transitions.

3.4 Dynamics for a fully-mixed population

We first study our model in a fully-mixed population, which yields a small set of coupled ODEs [BCF19]. We ignore contact patterns in both the information layer and the physical layer. Additionally, in each small time interval, we assume that each node interacts with other nodes in the same layer uniformly at random. We refer to this assumption as the "random-mixing assumption". In each time interval, we also assign each node in one layer to a counterpart node in the other layer uniformly at random (without replacement). We refer to this assumption as the "random-recoupling assumption". Recall that we use $[X] = \mathbb{E}[X]/N$ as the shorthand notation for the expectation of the random variable X divided by the population size N. Using the law of mass action, we obtain the following population-level dynamics:

$$\begin{aligned}
\frac{d}{dt}[|U|] &= -\frac{\beta_{\text{pro}}}{N}[|U| \times |P|] - \frac{\beta_{\text{anti}}}{N}[|U| \times |A|]\,, \\
\frac{d}{dt}[|P|] &= \frac{\beta_{\text{pro}}}{N}[|U| \times |P|] - \gamma_{\text{pro}}[|P|]\,, \\
\frac{d}{dt}[|A|] &= \frac{\beta_{\text{anti}}}{N}[|U| \times |A|] - \gamma_{\text{anti}}[|A|]\,, \\
\frac{d}{dt}[|R_{\text{info}}|] &= \gamma_{\text{pro}}[|P|] + \gamma_{\text{anti}}[|A|]\,, \\
\frac{d}{dt}[|S|] &= -\frac{\beta^*}{N}[|S| \times |I|]\,, \\
\frac{d}{dt}[|I|] &= \frac{\beta^*}{N}[|S| \times |I|] - \gamma_{\text{phy}}[|I|]\,, \\
\frac{d}{dt}[|R_{\text{phy}}|] &= \gamma_{\text{phy}}[|I|]\,,
\end{aligned} \tag{3.1}$$

where we use $|\cdot|$ to denote cardinality and

$$\beta^* = ([|P|]\alpha_{\text{pro}} + [|A|]\alpha_{\text{anti}} + 1 - [|A|] - [|P|])\beta_{\text{phy}}\,.$$

The first four equations in (3.1) describe the opinion dynamics. Uninformed nodes may adopt the pro- or anti-physical-distancing opinions by interacting with a node in the corresponding state. If a node adopts an opinion, it then can spread that opinion to its neighbors. The last four equations in (3.1) describe disease dynamics as a variant of the standard SIR model. The quantity β^* is the effective transmission rate; it depends on the relative prevalence of nodes in states P and A. To close the system, we approximate the expectations of products with the products of expectations. For example,

$$\frac{1}{N}[|U| \times |P|] \approx [|U|] \times [|P|] \,.$$

This provides a good approximation when N is large. Henceforth, we omit $|\cdot|$ to simplify our notation.

Consider the special case in which the transmission rate β_{pro}, recovery rate γ_{pro}, and initial population proportion of the pro-physical-distancing opinion are the same as the corresponding parameters for the anti-physical-distancing opinion. In this case, the effective transmission rate is $\beta^* = ([P](\alpha_{\text{anti}} + \alpha_{\text{pro}} - 2) + 1)\beta_{\text{phy}}$. Because $[P] \geq 0$, it follows that $\beta^* \geq \beta_{\text{phy}}$ if and only if $\alpha_{\text{anti}} + \alpha_{\text{pro}} \geq 2$. Therefore, if $\alpha_{\text{anti}} + \alpha_{\text{pro}} > 2$, the spread of opinions always leads to more individuals infected with the disease. If $\alpha_{\text{anti}} + \alpha_{\text{pro}} = 2$, the opinion dynamics has no effect on disease spread. This conclusion relies on the random-recoupling assumption, which implies that the information-layer counterpart of any physical-layer node is equally likely to be in any given opinion state. Because individuals hold an opinion for some time, the sign of $\alpha_{\text{anti}} + \alpha_{\text{pro}} - 2$ alone does not determine whether the influence of opinions leads to more infections or fewer infections when we consider the effects of network structure in Section 3.6.

Recall that the epidemic threshold in a standard SIR model of disease spread is characterized by the basic reproduction number $R_0 = \beta/\gamma$. An epidemic outbreak of the disease occurs if $R_0 > 1$. In our model, suppose that we start with a population in which most peo-

ple are susceptible and uninformed about the disease. In this case, β^* is close to β. In the limit in which the population becomes infinite with a vanishing fraction of people initially holding any opinion, the epidemic threshold is the same as in the standard SIR model and it is independent of the information layer. However, this conclusion does not hold if too many individuals hold some opinions about the disease at time 0.

Although an information contagion may not affect the epidemic threshold for the spread of a disease, it can still have a large impact on the disease's prevalence if an epidemic outbreak occurs. In Figure 3.4, we show an illustrative example to demonstrate how the information layer can affect the spread of a disease. For simplicity, we suppose that the pro- and anti-physical-distancing opinions share the same contagion parameters. Figure 3.4(a) shows an example in which we fix the parameters in the physical layer (on which the disease spreads) and investigate the effect of the opinion recovery rate on the final epidemic size (i.e., the total number of people who become infectious during the outbreak). Because we fix $\beta_{\text{info}} = 2$, the opinion contagion grows into an outbreak if γ_{info} is less than approximately 2. Consequently, all curves for the final epidemic size converge to the same value when γ_{info} is at least approximately 2. To assist our exposition, we use the term "basic size" to indicate the final epidemic size when the disease spreads independently of opinions. Because the effective transmission rate β^* satisfies $\beta^* \geq \beta_{\text{phy}}$, we expect the final epidemic size to be no smaller than the basic size.

The final epidemic size is affected by the prevalence of the nodes in states P and A and the relative spreading speeds of the opinions and the disease. As we increase γ_{info} in Figure 3.4(a), the final epidemic size tends to decrease, but it grows at first before decreasing to the basic size. To understand this, we compare the spreading dynamics on the two layers (see Figures 3.4(b) and 3.4(c)). Increasing γ_{info} leads to a reduction in the number of people in states P and A, which reduces the adverse influence from the information layer and results in fewer people becoming infected. Increasing γ_{info} also postpones the time that it takes for the physical layer to achieve herd immunity. Specifically, it takes longer for the I compartment

to reach its maximum size. We also see that increasing γ_{info} from 1 to 1.5 shortens the time difference between the opinion-prevalence peak and the disease-prevalence peak. As the two peaks become closer to each other, we observe transient growth in Figure 3.4(a). When we change the initial numbers of individuals in states A and P while fixing the initial numbers of individuals in state I in Figure 3.4(a), we effectively change the relative starting times of the opinion dynamics versus the disease dynamics, leading to differences between the curves.

3.5 Dynamics on a population with network structure

The random-mixing assumption and the random-recoupling assumption in Section 3.4 ignore contact patterns and oversimplify the dynamics of the spread of opinions and diseases. In real life, both in-person contacts and online interactions have intricate structural patterns that are far from homogeneous [New18]. Moreover, the random-recoupling assumption mixes the effects of the pro- and anti-physical-distancing opinions in a naive way and leads to features that contradict what we observe in individual-level simulations. Consequently, it is necessary to differentiate between different opinion states within the susceptible population and analyze the dynamics of the 12 compartments in Figure 3.3. Starting in this section, we incorporate network structure into our model and study the resulting dynamics in detail.

We develop a mean-field description of our system by generalizing the degree-based pair approximation model of Eames and Keeling [EK02] to our system of coupled opinion and disease dynamics. We assume that all nodes with the same degree are statistically equivalent, and we estimate the expected number of nodes and the expected number of dyads (i.e., pairs of nodes that are attached to the same edge) for each degree and each compartment [KMS17] using a closure model. We examine the dynamics of the spread of opinions and a disease using a mean of an ensemble of networks [PCV15, PG16]. We first develop an exact ODE system that involves single, pair, and triple terms based on the law of mass action. This system also depends on a set of time-dependent effective transmission rates. We close the

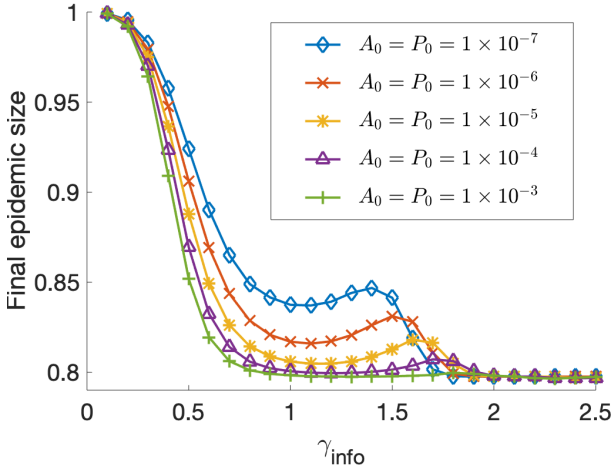

(a) Final epidemic size

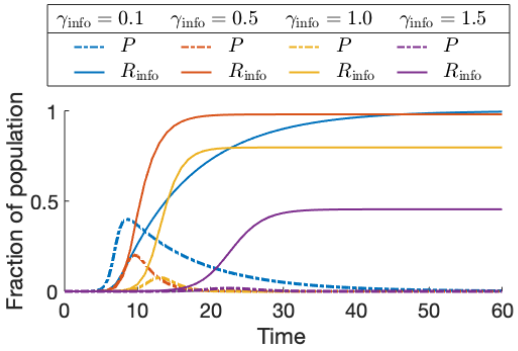

(b) Information layer

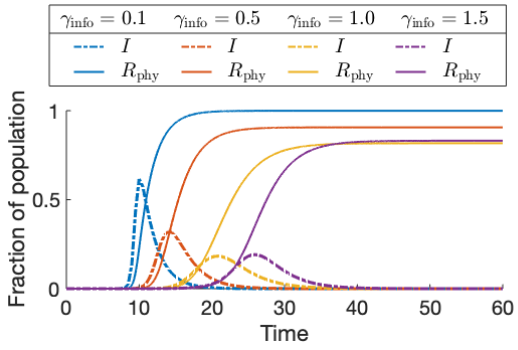

(c) Physical layer

Figure 3.4: The influence of the information layer on the physical layer depends on the opinion recovery rates. (a) Effects of γ_{info} on the final epidemic size for different initial conditions. For simplicity, we suppose that the pro- and anti-physical-distancing opinions share the same contagion parameters for all examples in the chapter. That is, $\beta_{\text{anti}} = \beta_{\text{pro}}$ (which we denote by β_{info}), $\gamma_{\text{anti}} = \gamma_{\text{pro}}$ (which we denote by γ_{info}), and $A_0 = P_0$, where $A_0 = [A](0)$ and $P_0 = [P](0)$. In the physical layer, we uniformly randomly infect a fraction $I_0 = [I](0) = 1 \times 10^{-6}$ of the population; the rest of the population starts in the susceptible state. The other parameters are $\beta_{\text{phy}} = 1$, $\gamma_{\text{phy}} = 0.5$, $\alpha_{\text{pro}} = 0.1$, $\alpha_{\text{anti}} = 10$, and $\beta_{\text{info}} = 2$. To help explain the non-monotonic curve in panel (a), we fix $P_0 = A_0 = 1 \times 10^{-6}$ and examine different values of γ_{info}. We show the ensuing dynamics of the fraction of the population in states P and R_{info} in panel (b) and the fraction of the population in states I and R_{phy} in panel (c).

system by approximating triple terms and the effective transmission rates using pair terms. The number of equations in the system depends on the number of distinct degrees and is independent of the population size.

3.5.1 Our dynamical system at the level of triples

Recall that we use two adjacent letters YX to describe the state (i.e., compartment) of an individual, where the first letter indicates the information layer and the second letter indicates the disease layer. The two intralayer degrees of a node are its numbers of neighbors in the two layers. We are interested only in intralayer degrees, so we treat our multiplex networks as edge-colored multigraphs [KAB14]. We use $Y_{k_1}X_{k_2}$ to refer to nodes in state YX with degree k_1 in the information layer and degree k_2 in the physical layer. We write the expected density of these nodes as $[Y_{k_1}X_{k_2}]$. To simplify our notation, we drop subscripts to indicate summation over all possible degrees. For example, $[YX_{k_2}] = \sum_{k_1}[Y_{k_1}X_{k_2}]$. For ease of notation, we also use one letter and thereby specify the state only in that layer when the context is clear. For example, S_{k_2} refers to susceptible nodes with degree k_2 in the physical layer and $[S_{k_2}]$ refers to the expected density of these nodes.

To track the states of the neighbors of a node, we write the expected normalized count of the dyads of nodes with states $\mathcal{S}_1$ and $\mathcal{S}_2$ as $[\mathcal{S}_1 \circ \mathcal{S}_2]$, where $\circ$ denotes an edge and the normalized count is the number of dyads divided by the population size. The layer of a dyad is clear from the context. For example, $[U_{k_1}S_{k_2} \circ I]$ represents the expected normalized count of dyads in the physical layer for which one end is attached to a $U_{k_1}S_{k_2}$ node and the other end is attached to an infectious node.

Given the above notation and definitions, the time evolution of the expected density of each compartment is

$$
\begin{aligned}
\frac{d}{dt}[U_{k_1}S_{k_2}] &= -[U_{k_1}S_{k_2} \circ I]\beta_{\text{phy}} - [U_{k_1}S_{k_2} \circ A]\beta_{\text{anti}} - [U_{k_1}S_{k_2} \circ P]\beta_{\text{pro}}\,, \\
\frac{d}{dt}[U_{k_1}I_{k_2}] &= [U_{k_1}S_{k_2} \circ I]\beta_{\text{phy}} - [U_{k_1}I_{k_2}]\gamma_{\text{phy}} - [U_{k_1}I_{k_2} \circ A]\beta_{\text{anti}} - [U_{k_1}I_{k_2} \circ P]\beta_{\text{pro}}\,, \\
\frac{d}{dt}[U_{k_1}R_{k_2}] &= [U_{k_1}I_{k_2}]\gamma_{\text{phy}} - [U_{k_1}R_{k_2} \circ A]\beta_{\text{anti}} - [U_{k_1}R_{k_2} \circ P]\beta_{\text{pro}}\,, \\
\frac{d}{dt}[A_{k_1}S_{k_2}] &= -[A_{k_1}S_{k_2} \circ I]\beta_{\text{phy}}\alpha_{\text{anti}} + [U_{k_1}S_{k_2} \circ A]\beta_{\text{anti}} - [A_{k_1}S_{k_2}]\gamma_{\text{anti}}\,,
\end{aligned}
$$

$$
\begin{aligned}
\frac{d}{dt}[A_{k_1} I_{k_2}] &= [A_{k_1} S_{k_2} \circ I]\beta_{\text{phy}}\alpha_{\text{anti}} - [A_{k_1} I_{k_2}](\gamma_{\text{phy}} + \gamma_{\text{anti}}) + [U_{k_1} I_{k_2} \circ A]\beta_{\text{anti}} \,, \\
\frac{d}{dt}[A_{k_1} R_{k_2}] &= [A_{k_1} I_{k_2}]\gamma_{\text{phy}} + [U_{k_1} R_{k_2} \circ A]\beta_{\text{anti}} - [A_{k_1} R_{k_2}]\gamma_{\text{anti}} \,, \\
\frac{d}{dt}[P_{k_1} S_{k_2}] &= -[P_{k_1} S_{k_2} \circ I]\beta_{\text{phy}}\alpha_{\text{pro}} + [U_{k_1} S_{k_2} \circ P]\beta_{\text{pro}} - [P_{k_1} S_{k_2}]\gamma_{\text{pro}} \,, \\
\frac{d}{dt}[P_{k_1} I_{k_2}] &= [P_{k_1} S_{k_2} \circ I]\beta_{\text{phy}}\alpha_{\text{pro}} - [P_{k_1} I_{k_2}](\gamma_{\text{phy}} + \gamma_{\text{pro}}) + [U_{k_1} I_{k_2} \circ P]\beta_{\text{pro}} \,, \\
\frac{d}{dt}[P_{k_1} R_{k_2}] &= [P_{k_1} I_{k_2}]\gamma_{\text{phy}} + [U_{k_1} R_{k_2} \circ P]\beta_{\text{pro}} - [P_{k_1} R_{k_2}]\gamma_{\text{pro}} \,, \\
\frac{d}{dt}[R_{k_1} S_{k_2}] &= -[R_{k_1} S_{k_2} \circ I]\beta_{\text{phy}} + [A_{k_1} S_{k_2}]\gamma_{\text{anti}} + [P_{k_1} S_{k_2}]\gamma_{\text{pro}} \,, \\
\frac{d}{dt}[R_{k_1} I_{k_2}] &= [R_{k_1} S_{k_2} \circ I]\beta_{\text{phy}} - [R_{k_1} I_{k_2}]\gamma_{\text{phy}} + [A_{k_1} I_{k_2}]\gamma_{\text{anti}} + [P_{k_1} I_{k_2}]\gamma_{\text{pro}} \,.
\end{aligned} \tag{3.2}
$$

To illustrate the equations in (3.2), we briefly discuss one of them. In the first equation, the expected number of $U_{k_1} S_{k_2}$ nodes decreases as the nodes become infectious or adopt one of the two opinions. The infection rate is proportional to the number of infectious neighbors (or, equivalently, to the number of $U_{k_1} S_{k_2} \circ I_l$ dyads). We do not track the opinion states of those infectious neighbors because we assume that those opinions do not affect the transmission rate of the $U_{k_1} S_{k_2}$ nodes. The same reasoning applies to the other dyads.

We expand the right-hand side of the system (3.2) by tracking the dynamics of node pairs, which depend on the neighbors of both nodes and thus involve triples. Let $[X \circ Y \circ Z]$ denote the expected normalized count of triples in which the center node Y is adjacent to X and to Z. Analogously to the normalized count of a dyad, we define the normalized count of a triple to be the number of triples divided by the population size. The two edges may belong to the same layer or to different layers; this is clear from the context. For example, $U_{k_1} S_{k_2} \circ S_l \circ I$ refers to triples in which the center node S_l has physical-layer neighbors with states $U_{k_1} S_{k_2}$ and I. Additionally, $P \circ U_{k_1} S_{k_2} \circ I_l$ refers to triples in which one edge connects $U_{k_1} S_{k_2}$ and P nodes in the information layer and the other connects $U_{k_1} S_{k_2}$ and I_l nodes in the physical layer. We now write the evolution of the expected normalized count of the

dyads in terms of triple terms:

$$
\begin{aligned}
\frac{d}{dt}[U_{k_1}S_{k_2}\circ I_l] &= [U_{k_1}S_{k_2}\circ S_l\circ I]\hat{\beta}_{l,\,k_2} - ([U_{k_1}S_{k_2}\circ I_l] + [I\circ U_{k_1}S_{k_2}\circ I_l])\beta_{\text{phy}} \\
&\quad - [U_{k_1}S_{k_2}\circ I_l]\gamma_{\text{phy}} - [P\circ U_{k_1}S_{k_2}\circ I_l]\beta_{\text{pro}} - [A\circ U_{k_1}S_{k_2}\circ I_l]\beta_{\text{anti}}\,, \\
\frac{d}{dt}[U_{k_1}S_{k_2}\circ S_l] &= -[U_{k_1}S_{k_2}\circ S_l\circ I]\hat{\beta}_{l,\,k_2} - [I\circ U_{k_1}S_{k_2}\circ S_l]\beta_{\text{phy}} \\
&\quad - [P\circ U_{k_1}S_{k_2}\circ S_l]\beta_{\text{pro}} - [A\circ U_{k_1}S_{k_2}\circ S_l]\beta_{\text{anti}}\,, \\
\frac{d}{dt}[U_{k_1}S_{k_2}\circ A_l] &= -[P\circ U_{k_1}S_{k_2}\circ A_l]\beta_{\text{pro}} - [U_{k_1}S_{k_2}\circ A_l]\gamma_{\text{anti}} - [I\circ U_{k_1}S_{k_2}\circ A_l]\beta_{\text{phy}} \\
&\quad + ([U_{k_1}S_{k_2}\circ U_l\circ A] - [U_{k_1}S_{k_2}\circ A_l] - [A\circ U_{k_1}S_{k_2}\circ A_l])\beta_{\text{anti}}\,, \\
\frac{d}{dt}[U_{k_1}S_{k_2}\circ P_l] &= -[A\circ U_{k_1}S_{k_2}\circ P_l]\beta_{\text{anti}} - [U_{k_1}S_{k_2}\circ P_l]\gamma_{\text{pro}} - [I\circ U_{k_1}S_{k_2}\circ P_l]\beta_{\text{phy}} \\
&\quad + ([U_{k_1}S_{k_2}\circ U_l\circ P] - [U_{k_1}S_{k_2}\circ P_l] - [P\circ U_{k_1}S_{k_2}\circ P_l])\beta_{\text{pro}}\,, \\
\frac{d}{dt}[U_{k_1}S_{k_2}\circ U_l] &= -([P\circ U_{k_1}S_{k_2}\circ U_l] + [U_{k_1}S_{k_2}\circ U_l\circ P])\beta_{\text{pro}} - [I\circ U_{k_1}S_{k_2}\circ U_l]\beta_{\text{phy}} \\
&\quad - ([A\circ U_{k_1}S_{k_2}\circ U_l] + [U_{k_1}S_{k_2}\circ U_l\circ A])\beta_{\text{anti}}\,, \\
\frac{d}{dt}[U_{k_1}I_{k_2}\circ A_l] &= ([U_{k_1}I_{k_2}\circ U_l\circ A] - [A\circ U_{k_1}I_{k_2}\circ A_l])\beta_{\text{anti}} - [P\circ U_{k_1}I_{k_2}\circ A_l]\beta_{\text{pro}} \\
&\quad + [I\circ U_{k_1}S_{k_2}\circ A_l]\beta_{\text{phy}} - [U_{k_1}I_{k_2}\circ A_l](\gamma_{\text{phy}} + \gamma_{\text{anti}} + \beta_{\text{anti}})\,, \\
\frac{d}{dt}[U_{k_1}I_{k_2}\circ P_l] &= ([U_{k_1}I_{k_2}\circ U_l\circ P] - [P\circ U_{k_1}I_{k_2}\circ P_l])\beta_{\text{pro}} - [A\circ U_{k_1}I_{k_2}\circ P_l]\beta_{\text{anti}} \\
&\quad + [I\circ U_{k_1}S_{k_2}\circ P_l]\beta_{\text{phy}} - [U_{k_1}I_{k_2}\circ P_l](\beta_{\text{pro}} + \gamma_{\text{phy}} + \gamma_{\text{pro}})\,, \\
\frac{d}{dt}[U_{k_1}I_{k_2}\circ U_l] &= [I\circ U_{k_1}S_{k_2}\circ U_l]\beta_{\text{phy}} - ([A\circ U_{k_1}I_{k_2}\circ U_l] + [U_{k_1}I_{k_2}\circ U_l\circ A])\beta_{\text{anti}} \\
&\quad - ([U_{k_1}I_{k_2}\circ U_l\circ P] + [P\circ U_{k_1}I_{k_2}\circ U_l])\beta_{\text{pro}} - [U_{k_1}I_{k_2}\circ U_l]\gamma_{\text{phy}}\,, \\
\frac{d}{dt}[U_{k_1}R_{k_2}\circ A_l] &= [U_{k_1}I_{k_2}\circ A_l]\gamma_{\text{phy}} - [U_{k_1}R_{k_2}\circ A_l]\gamma_{\text{anti}} - [P\circ U_{k_1}R_{k_2}\circ A_l]\beta_{\text{pro}} \\
&\quad + ([U_{k_1}R_{k_2}\circ U_l\circ A] - [U_{k_1}R_{k_2}\circ A_l] - [A\circ U_{k_1}R_{k_2}\circ A_l])\beta_{\text{anti}}\,, \\
\frac{d}{dt}[U_{k_1}R_{k_2}\circ P_l] &= [U_{k_1}I_{k_2}\circ P_l]\gamma_{\text{phy}} - [U_{k_1}R_{k_2}\circ P_l]\gamma_{\text{pro}} - [A\circ U_{k_1}R_{k_2}\circ P_l]\beta_{\text{anti}} \\
&\quad + ([U_{k_1}R_{k_2}\circ U_l\circ P] - [U_{k_1}R_{k_2}\circ P_l] - [P\circ U_{k_1}R_{k_2}\circ P_l])\beta_{\text{pro}}\,, \\
\frac{d}{dt}[U_{k_1}R_{k_2}\circ U_l] &= [U_{k_1}I_{k_2}\circ U_l]\gamma_{\text{phy}} - ([U_{k_1}R_{k_2}\circ U_l\circ A] + [A\circ U_{k_1}R_{k_2}\circ U_l])\beta_{\text{anti}}
\end{aligned}
$$

$$
\begin{aligned}
&\quad - ([U_{k_1}R_{k_2} \circ U_l \circ P] + [P \circ U_{k_1}R_{k_2} \circ U_l])\beta_{\text{pro}}\,, \\
\frac{d}{dt}[A_{k_1}S_{k_2} \circ I_l] &= [A \circ U_{k_1}S_{k_2} \circ I_l]\beta_{\text{anti}} - [A_{k_1}S_{k_2} \circ I_l](\gamma_{\text{phy}} + \gamma_{\text{anti}} + \beta_{\text{phy}}\alpha_{\text{anti}}) \\
&\quad + [A_{k_1}S_{k_2} \circ S_l \circ I]\hat{\beta}_{l,\,k_2} - [I \circ A_{k_1}S_{k_2} \circ I_l]\beta_{\text{phy}}\alpha_{\text{anti}}\,, \\
\frac{d}{dt}[A_{k_1}S_{k_2} \circ S_l] &= -[A_{k_1}S_{k_2} \circ S_l \circ I]\hat{\beta}_{l,\,k_2} - [I \circ A_{k_1}S_{k_2} \circ S_l]\beta_{\text{phy}}\alpha_{\text{anti}} \\
&\quad + [A \circ U_{k_1}S_{k_2} \circ S_l]\beta_{\text{anti}} - [A_{k_1}S_{k_2} \circ S_l]\gamma_{\text{anti}}\,, \\
\frac{d}{dt}[P_{k_1}S_{k_2} \circ I_l] &= [P \circ U_{k_1}S_{k_2} \circ I_l]\beta_{\text{pro}} - [P_{k_1}S_{k_2} \circ I_l](\gamma_{\text{phy}} + \gamma_{\text{anti}} + \beta_{\text{phy}}\alpha_{\text{pro}}) \\
&\quad + [P_{k_1}S_{k_2} \circ S_l \circ I]\hat{\beta}_{l,\,k_2} - [I \circ P_{k_1}S_{k_2} \circ I_l]\beta_{\text{phy}}\alpha_{\text{pro}}\,, \\
\frac{d}{dt}[P_{k_1}S_{k_2} \circ S_l] &= -[P_{k_1}S_{k_2} \circ S_l \circ I]\hat{\beta}_{l,\,k_2} - [I \circ P_{k_1}S_{k_2} \circ S_l]\beta_{\text{phy}}\alpha_{\text{pro}} \\
&\quad + [P \circ U_{k_1}S_{k_2} \circ S_l]\beta_{\text{pro}} - [P_{k_1}S_{k_2} \circ S_l]\gamma_{\text{pro}}\,, \\
\frac{d}{dt}[R_{k_1}S_{k_2} \circ I_l] &= [R_{k_1}S_{k_2} \circ S_l \circ I]\hat{\beta}_{l,\,k_2} - ([R_{k_1}S_{k_2} \circ I_l] + [I \circ R_{k_1}S_{k_2} \circ I_l])\beta_{\text{phy}} \\
&\quad - [R_{k_1}S_{k_2} \circ I_l]\gamma_{\text{phy}} + [A_{k_1}S_{k_2} \circ I_l]\gamma_{\text{anti}} + [P_{k_1}S_{k_2} \circ I_l]\gamma_{\text{pro}}\,, \\
\frac{d}{dt}[R_{k_1}S_{k_2} \circ S_l] &= -[R_{k_1}S_{k_2} \circ S_l \circ I]\hat{\beta}_{l,\,k_2} - [I \circ R_{k_1}S_{k_2} \circ S_l]\beta_{\text{phy}} \\
&\quad + [A_{k_1}S_{k_2} \circ S_l]\gamma_{\text{anti}} + [P_{k_1}S_{k_2} \circ S_l]\gamma_{\text{pro}}\,,
\end{aligned}
\tag{3.3}
$$

where $\hat{\beta}_{l,\,k_2}$ is the expected transmission rate of the center node S_l in a triple of the form $YS_{k_2} \circ S_l \circ I$.

One derives the system (3.3) using the same reasoning as in (3.2). For example, consider the first equation in (3.3). The normalized count of the dyads $U_{k_1}S_{k_2} \circ I_l$ decreases as $U_{k_1}S_{k_2}$ nodes adopt one of the two opinions at rate $[P \circ U_{k_1}S_{k_2} \circ I_l]\beta_{\text{pro}} + [A \circ U_{k_1}S_{k_2} \circ I_l]\beta_{\text{anti}}$, is infected by I_l at rate $[U_{k_1}S_{k_2} \circ I_l]\beta_{\text{phy}}$, or is infected by infectious neighbors other than I_l at rate $[I \circ U_{k_1}S_{k_2} \circ I_l]\beta_{\text{phy}}$. The normalized count of $U_{k_1}S_{k_2} \circ I_l$ increases as susceptible neighbors of $U_{k_1}S_{k_2}$ are infected by their infectious neighbors at rate $[U_{k_1}S_{k_2} \circ S_l \circ I]\hat{\beta}_{l,\,k_2}$. Each dyad in (3.3) has one node whose state we track in only one of the layers. For example, for the dyad $U_{k_1}S_{k_2} \circ S_l$, we do not know the opinion states of node S_l. We need an approximation

for the disease transmission rate $\hat{\beta}_{l,\,k_2}$ when node S_l is infected by a neighbor in state I. In principle, one can track the states of both nodes on both layers and avoid the need for this approximation. However, doing this leads to a higher-dimensional system. We discuss the approximation of $\hat{\beta}_{l,\,k_2}$ in Section 3.5.3.

In principle, one can also work out the right-hand sides for the evolution of the expected normalized counts of the triple terms. These incorporate quadruple terms, and if we expand those terms and keep expanding expressions for the evolution of progressively larger network motifs (i.e., connected subgraphs), we eventually obtain an exact dynamical system. However, it is very high-dimensional and difficult to study. Therefore, we approximate the triple terms with pair terms on the right-hand sides of (3.3) using the approach in [EK02].

3.5.2 Closure of the triple terms

For a given type of triple $X \circ Y_k \circ Z$, we assume that the neighbors of all Y_k nodes are interchangeable. Therefore, every neighbor has the same probability of being in a given state (e.g., state X).

If both edges are in the same layer, then for nodes X and Z that are adjacent to a center degree-k node in state Y in the same layer, it follows that

$$\begin{aligned}[X \circ Y_k \circ Z] &\approx k(k-1)[Y_k]\frac{[X \circ Y_k]}{k[Y_k]}\frac{[Y_k \circ Z]}{k[Y_k]} \\ &= \frac{k-1}{k}\frac{[X \circ Y_k][Y_k \circ Z]}{[Y_k]}\,. \end{aligned} \tag{3.4}$$

Intuitively, nodes in state Y_k have $k[Y_k]$ edges; an expected fraction $\frac{[X \circ Y_k]}{k[Y_k]}$ of these edges are attached to nodes in state X, and an expected fraction $\frac{[Y_k \circ Z]}{k[Y_k]}$ of these edges are attached to nodes in state Z. Therefore, if we choose a node in state Y_k uniformly at random, the probability that two uniformly random neighbors of the Y_k node are in states X and Z is approximately $\frac{[X \circ Y_k]}{k[Y_k]} \times \frac{[Y_k \circ Z]}{k[Y_k]}$ when N is large. Because there are $k(k-1)$ ways to choose

the two neighbors, we obtain (3.4). As concrete examples,

$$
\begin{aligned}
[U_{k_1} S_{k_2} \circ S_l \circ I] &\approx \frac{l-1}{l} \frac{[U_{k_1} S_{k_2} \circ S_l][S_l \circ I]}{[S_l]} \,, \\
[I \circ U_{k_1} S_{k_2} \circ S_l] &\approx \frac{k_2 - 1}{k_2} \frac{[I \circ U_{k_1} S_{k_2}][U_{k_1} S_{k_2} \circ S_l]}{[U_{k_1} S_{k_2}]} \,, \\
[A \circ U_{k_1} S_{k_2} \circ A_l] &\approx \frac{k_1 - 1}{k_1} \frac{[A \circ U_{k_1} S_{k_2}][U_{k_1} S_{k_2} \circ A_l]}{[U_{k_1} S_{k_2}]} \,.
\end{aligned}
$$

Suppose instead that the two edges that connect the center node $Y_{1,k_1} Y_{2,k_2}$ to nodes in states X and Z are in different layers. If the node in state X is in the information layer and the node in state Z is in the physical layer, we obtain

$$
\begin{aligned}
[X \circ Y_{1,k_1} Y_{2,k_2} \circ Z] &\approx k_1 k_2 [Y_{1,k_1} Y_{2,k_2}] \frac{[X \circ Y_{1,k_1} Y_{2,k_2}]}{k_1 [Y_{1,k_1} Y_{2,k_2}]} \frac{[Y_{1,k_1} Y_{2,k_2} \circ Z]}{k_2 [Y_{1,k_1} Y_{2,k_2}]} \\
&= \frac{[X \circ Y_{1,k_1} Y_{2,k_2}][Y_{1,k_1} Y_{2,k_2} \circ Z]}{[Y_{1,k_1} Y_{2,k_2}]} \,.
\end{aligned}
$$

For example,

$$
[P \circ U_{k_1} S_{k_2} \circ I_l] \approx \frac{[P \circ U_{k_1} S_{k_2}][U_{k_1} S_{k_2} \circ I_l]}{[U_{k_1} S_{k_2}]} \,.
$$

One can work out approximations for the other triple terms similarly.

3.5.3 Approximate transmission rate

To close equations (3.2)–(3.3), we need to find an approximation of $\hat{\beta}_{l,\,k_2}$, which is the expected transmission rate of the center node for triples of the form $Y S_{k_2} \circ S_l \circ I$. We need to approximate the opinion distribution in each population of interest. The random-recoupling assumption in Section 3.4 corresponds to setting

$$
\hat{\beta}_{l,\,k_2} \approx ([U] + [A]\alpha_{\text{anti}} + [P]\alpha_{\text{pro}} + [R])\beta_{\text{phy}} \,. \tag{3.5}
$$

However, it is possible to keep track of corresponding nodes in the two layers. A naive approach is to weight the influence coefficients based on the densities of nodes with different opinion states among the S_l nodes. That is,

$$\hat{\beta}_{l,\,k_2} \approx \frac{[US_l] + [AS_l]\alpha_{\text{anti}} + [PS_l]\alpha_{\text{pro}} + [RS_l]}{[S_l]}\beta_{\text{phy}}\,. \tag{3.6}$$

However, the approximation (3.6) ignores the fact that the S_l node of interest has both an intralayer neighbor in state S and an intralayer neighbor in state I. Incorporating this neighborhood information yields the approximation

$$\begin{aligned}\hat{\beta}_{l,\,k_2} \approx \Big([S_{k_2} \circ US_l \circ I] + [S_{k_2} \circ AS_l \circ I]\alpha_{\text{anti}} \\ + [S_{k_2} \circ PS_l \circ I]\alpha_{\text{pro}} + [S_{k_2} \circ RS_l \circ I]\Big) \times \frac{\beta_{\text{phy}}}{[S_{k_2} \circ S_l \circ I]}\,.\end{aligned} \tag{3.7}$$

We approximate the triples in (3.7) with our pair approximation:

$$\begin{aligned}
[S_{k_2} \circ U_k S_l \circ I] &\approx \frac{l-1}{l}\frac{[U_k S_l \circ S_{k_2}][U_k S_l \circ I]}{[U_k S_l]}\,,\\
[S_{k_2} \circ A_k S_l \circ I] &\approx \frac{l-1}{l}\frac{[A_k S_l \circ S_{k_2}][A_k S_l \circ I]}{[A_k S_l]}\,,\\
[S_{k_2} \circ P_k S_l \circ I] &\approx \frac{l-1}{l}\frac{[P_k S_l \circ S_{k_2}][P_k S_l \circ I]}{[P_k S_l]}\,,\\
[S_{k_2} \circ R_k S_l \circ I] &\approx \frac{l-1}{l}\frac{[R_k S_l \circ S_{k_2}][R_k S_l \circ I]}{[R_k S_l]}\,,\\
[S_{k_2} \circ S_l \circ I] &= [S_{k_2} \circ US_l \circ I] + [S_{k_2} \circ AS_l \circ I]\\
&\quad + [S_{k_2} \circ PS_l \circ I] + [S_{k_2} \circ RS_l \circ I]\,.
\end{aligned}$$

We expect the value of $\hat{\beta}_{l,\,k_2}$ in equation (3.6) to be smaller than its value in equation (3.5). This, in turn, leads to a smaller estimate of the disease prevalence from equation (3.6) than from equation (3.5). Intuitively, because individuals who hold the anti-physical-distancing opinion become infected at a higher rate, a typical susceptible individual is less

likely to have an anti-physical-distancing opinion than a member of the population that one selects uniformly at random. Therefore, we expect that $[A] \geq \frac{[AS_l]}{[S_l]}$. By applying analogous reasoning to individuals who hold the pro-physical-distancing opinion, we expect that $[P] \leq \frac{[PS_l]}{[S_l]}$. We do not have a mathematically rigorous understanding of how well the approximations (3.6) and (3.7) match the full stochastic system (see Section 3.3 and our code in [Pen21].) We compare the three different pair approximations of the disease prevalence that are based on equations (3.5)–(3.7) with direct numerical simulations of the full stochastic system in Figure 3.5. From this comparison, we see that the approximations (3.5) and (3.6) overestimate the infectious population and that the approximation (3.7) matches the simulations very well. These numerical results indicate that it is essential to track the coupling of the nodes' states at both ends of interlayer edges and intralayer edges to ensure accurate estimations of time evolution of disease prevalence. We use the pair approximation (3.2, 3.3, 3.7) in our experiments in Section 3.6.

3.6 Computational experiments

We now investigate our full model by simulating the stochastic system (see our code in [Pen21]) and applying the pair approximation (3.2, 3.3, 3.7), which we henceforth call our "PA". We explore the influence of competing opinion contagions on the spread of a disease for a variety of parameter values. We focus on examining different opinion contagion parameters (see Section 3.6.1) and network structures (see Sections 3.6.2 and 3.6.3). For ease of comparison, we consider the special case in which the pro- and anti-physical-distancing opinions share the same contagion parameters for all examples in this chapter. Additionally, we fix the disease contagion parameters to be $\beta_{\text{phy}} = 0.6$ and $\gamma_{\text{phy}} = 1$. Unless we specify otherwise, we set the opinion influence coefficients to be $\alpha_{\text{pro}} = 0.1$ and $\alpha_{\text{anti}} = 10$ to incorporate nontrivial influence of the corresponding opinion on the spread of the disease. This asymmetry between pro- and anti-physical-distancing opinions affects the dynamics in

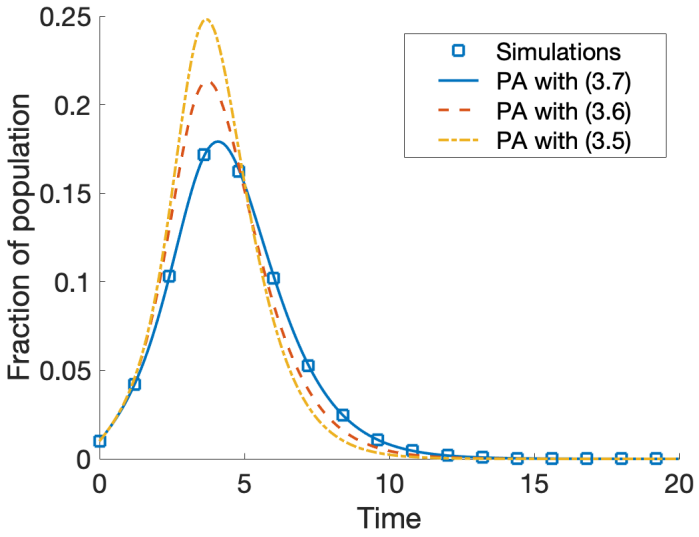

Figure 3.5: Comparison of our pair approximations (PAs) based on equations (3.5)–(3.7) (the curves) with direct numerical simulations (the markers). The trajectories show the time evolution of the infectious population. In each simulation, we generate a network with layers that consist of 5-regular configuration-model graphs (i.e., each node has degree 5). We uniformly randomly infect a fraction $I_0 = 0.01$ of the nodes, and we independently and uniformly randomly choose initial opinions such that $A_0 = P_0 = 0.005$. The displayed results are means of 100 simulations. The other parameters are $\beta_{\text{phy}} = \beta_{\text{info}} = 0.6$, $\gamma_{\text{phy}} = \gamma_{\text{info}} = 1$, $\alpha_{\text{anti}} = 10$, and $\alpha_{\text{pro}} = 0.1$.

an interesting way, as we illustrate in this section. In many of the following examples, it is helpful to separate the influence of the two opinions to gain understanding of the overall behavior. To do this, we suppress the influence of an opinion by setting its influence coefficient to be 1. In Section 3.6.1, we do a parameter sweep of the opinion transmission parameters in the range [0, 2] to illustrate that the final epidemic size can change non-monotonically as we increase the recovery rate of an opinion. This feature occurs in networks with a variety of degree distributions. Because of the issuing or lifting of stay-at-home orders, people's contact patterns in the offline world can change a lot over the course of an epidemic (and especially a pandemic) [ZLL20, FM21]. In Sections 3.6.2 and 3.6.3, we show examples that illustrate that the influence of an opinion contagion on the spread of a disease can change in important ways when we change the intralayer or cross-layer correlations of intralayer degrees.

In each computational experiment, we construct a network of $N = 10000$ nodes and simulate the dynamics on it using a Gillespie algorithm [KMS17], which is a well-known approach for performing continuous-time simulations of Markovian processes. In all experiments in this section, we report results as means of 200 simulations. In each simulation, we generate new random graphs (of a few different types, which we specify below). We uniformly randomly infect a fraction $I_0 = 0.01$ of the nodes in the physical layer, and we independently and uniformly randomly choose $A_0 = P_0 = 0.005$ nodes as anti- or pro-physical-distancing in the information layer. We set all remaining node states to S in the physical layer and to U in the information layer. Henceforth, unless we state otherwise, we use these choices of initial states in our numerical computations.

In our initial experiments, we construct each network layer from a configuration model [FLN18] and match the nodes from the two layers uniformly at random. Specifically, we specify degree distributions $\mathbb{P}_{\text{info}}$ and $\mathbb{P}_{\text{phy}}$, which need not be the same. For each layer, we sample a degree sequence $\{k_i\}$ (where $i \in \{1, \ldots, N\}$ indexes the nodes) from the corresponding degree distribution; therefore, node i has k_i ends of edges (i.e., stubs). We match these

stubs uniformly at random to form a network. Correspondingly, in the pair approximation, we have

$$[Y_{k_1}X_{k_2}](0) = Y_0 X_0 \mathbb{P}_{\text{info}}(k_1)\mathbb{P}_{\text{phy}}(k_2)\,,$$

$$[Y_{k_1}X_{k_2} \circ Z_{k_3}](0) = \begin{cases} [Y_{k_1}X_{k_2}](0) \times Z_0 \mathbb{P}_{\text{info}}(k_3) k_1 k_3 / \langle k_{\text{info}} \rangle\,, & Z \in \{U,\, P,\, A,\, R_{\text{info}}\} \\ [Y_{k_1}X_{k_2}](0) \times Z_0 \mathbb{P}_{\text{phy}}(k_3) k_2 k_3 / \langle k_{\text{phy}} \rangle\,, & Z \in \{S,\, I,\, R_{\text{phy}}\}\,. \end{cases}$$

In Figure 3.6, we compare typical disease prevalence curves (i.e., the time evolution of infectious populations) when we choose different coefficients for the influence of the opinions. The influence from the information layer changes a disease's prevalence, its peak value, and the time at which the peak number of infections occurs. Although an opinion does not alter the susceptibility of individuals to infection when the corresponding influence coefficient is 1, the spread of that opinion can still indirectly affect the overall disease dynamics, which thus can be different from the dynamics in a system with only one opinion. For example, in Figure 3.6(a), the purple curve with triangle markers (for which $\alpha_{\text{anti}} = 1$ and $\alpha_{\text{pro}} = 0.1$) has a higher disease prevalence than the green curve with plus signs (for which $\alpha_{\text{pro}} = 0.1$ and the anti-physical-distancing opinion is absent). The spread of the anti-physical-distancing opinion prevents some people from adopting the pro-physical-distancing opinion, although the anti-physical-distancing opinion has an influence coefficient of 1. We show the corresponding dynamics on the information layer in Figures 3.6(b) and 3.6(c).

3.6.1 Opinion contagion parameters

Recall from Section 3.4 that in a fully-mixed population with $\alpha_{\text{pro}} + \alpha_{\text{anti}} > 2$, the information layer leads to a larger epidemic size than when there is no influence from the information layer. We repeat the experiment that we showed in Figure 3.4, but now we have a network structure and we employ our PA. We again consider the scenario in which the anti- and pro-physical-distancing opinions have the same contagion parameter values; we denote this

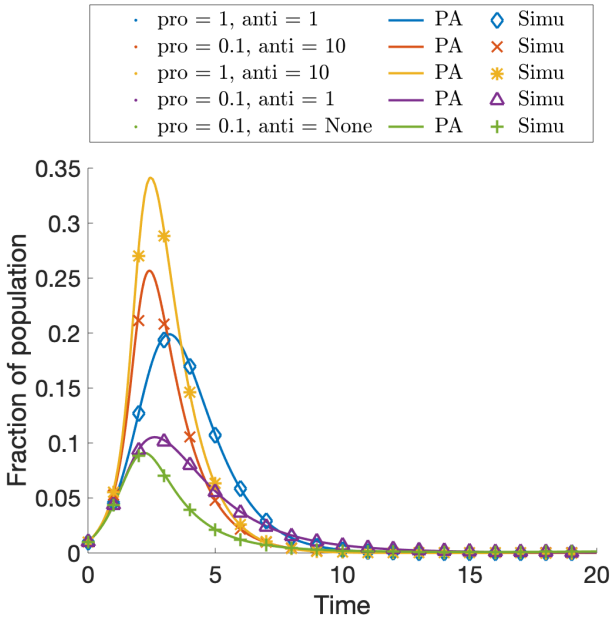

(a) Disease prevalence

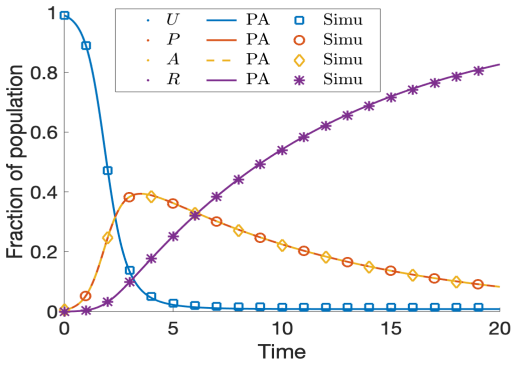

(b) Information layer; only the pro-physical-distance opinion has influence

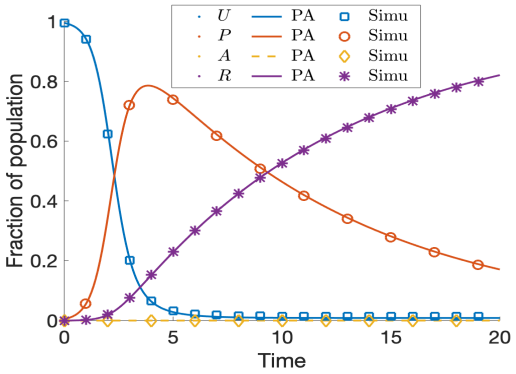

(c) Information layer; no anti-physical-distance opinion

Figure 3.6: Dynamics for different opinion influence coefficients. (a) Disease prevalence curves for different influence coefficients, including when the anti-physical-distancing opinion is absent (which we denote by "anti = None"). In (b, c), we show the dynamics on the information layer when (b) both opinions are present and (c) only the pro-physical-distancing opinion is present. We construct each layer from a configuration model with a degree sequence that we choose from a Poisson degree distribution with mean degree 5. The other parameters are $\beta_{\text{phy}} = \beta_{\text{info}} = 0.6$, $\gamma_{\text{phy}} = 1$, and $\gamma_{\text{info}} = 0.1$. The curves (respectively, markers) indicate results from the PA (respectively, from means of 200 direct simulations).

situation using the subscript "info". Figure 3.7(a) shows final epidemic sizes versus the recovery rate γ_{info} in the information layer for the following three situations: (1) all nodes have degree 5 (i.e., we consider 5-regular graphs); (2) all node degrees follow a Poisson distribution with mean 5; and (3) all node degrees follow a truncated power-law distribution with $\mathbb{P}(k = x) \propto x^{-1.32} e^{-x/35}$ for $x \leq 50$ and $\mathbb{P}(k = x) = 0$ for $x > 50$. In each situation,

we generate both layers using configuration-model networks and we independently sample degrees for each layer from the same distribution. The mean degree is roughly 5 in all three situations. In all three situations, the final epidemic size can be smaller than the corresponding basic size (i.e., without opinion spread) when γ_{info} is very small. As we increase γ_{info}, the final epidemic size first increases and surpasses the basic size before reaching a peak; it subsequently decreases to the basic size.

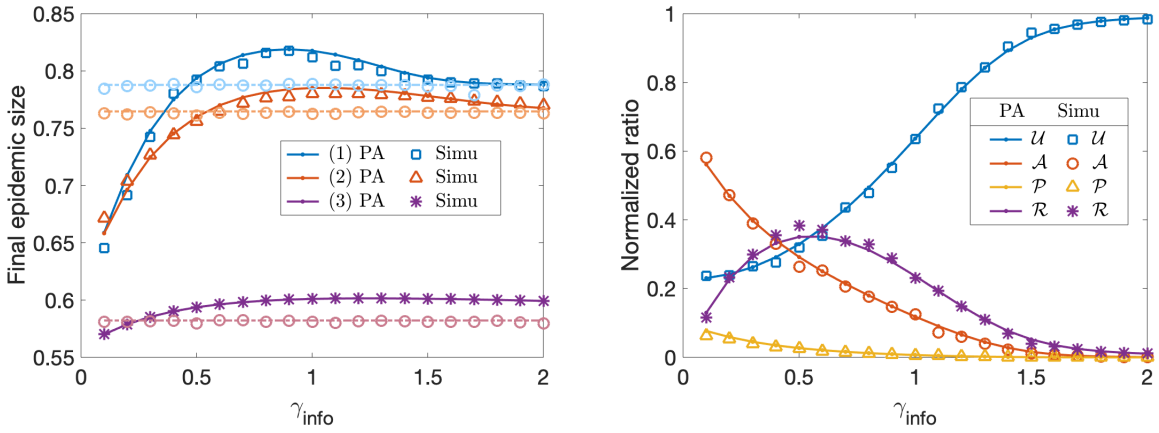

(a) Final epidemic size

(b) Decomposition of opinion states

Figure 3.7: Influence of the opinion recovery rate γ_{info} on disease prevalence and on the distribution of opinion states when people become infectious. (a) The final epidemic size for different values of γ_{info}. The solid curves and non-circle symbols mark the final epidemic sizes under influence from the information layer. The dashed curves and circles mark the basic size. We consider three situations: (1) each layer is a 5-regular graph; (2) all node degrees follow a Poisson distribution with mean 5; and (3) all node degrees follow a truncated power-law distribution with $\mathbb{P}(k = x) \propto x^{-1.32}e^{-x/35}$ for $x \leq 50$ and $\mathbb{P}(k = x) = 0$ for $x > 50$. We construct each layer from a configuration model with a degree sequence chosen from the specified degree distribution. The other parameters are $\beta_{\text{phy}} = \beta_{\text{info}} = 0.6$, $\gamma_{\text{phy}} = 1$, $\alpha_{\text{anti}} = 10$, and $\alpha_{\text{pro}} = 0.1$. (b) We group recovered people based on their opinion states when they become infectious (we use the notation $\mathcal{U}$, $\mathcal{P}$, $\mathcal{A}$, and $\mathcal{R}$ for these subpopulations) and plot the normalized size. We show results (which are means of 200 simulations) for 5-regular configuration-model graphs. The curves (respectively, markers) indicate results from the PA (respectively, direct simulations).

To explain this non-monotonic behavior, we decompose the recovered population at steady state into subpopulations based on their opinion states when they become infec-

tious and plot the relative size of each subpopulation (with a sum that is normalized to 1) in Figure 3.7(b). We use $\mathcal{U}$, $\mathcal{A}$, $\mathcal{P}$, and $\mathcal{R}$ to denote the subpopulations that become infectious when they are in the U, A, P, and R_{info} states, respectively. We show results when both layers are 5-regular graphs. Our results on networks with the Poisson and truncated power-law distributions are qualitatively the same. Because increasing opinion recovery rates results in fewer individuals adopting any opinions, the size of the $\mathcal{U}$ subpopulation increases (i.e., more people become infected while uninformed). For the same reason, the sizes of the subpopulations with the anti- and pro-physical-distancing opinions decrease with increasing opinion recovery rates. The size of the $\mathcal{R}$ subpopulation first increases as we increase γ_{info}. This occurs because when γ_{info} is very small, many individuals keep the same opinion (P or A) until the disease dies out in the population. When we start to increase γ_{info}, more individuals recover from an opinion when the disease is still actively spreading. Because individuals who abandon the pro-physical-distancing behavior increase their risk of becoming infected, the overall epidemic size may increase when they become less cautious. As γ_{info} grows, fewer individuals adopt an opinion; this, in turn, leads to a smaller $\mathcal{R}$ subpopulation and a drop in the overall epidemic size.

The non-monotonic behavior that we described above suggests that if enough individuals hold the pro-physical-distancing opinion for a sufficiently long time, the prevalence of a disease can decrease, even when the anti-physical-distancing opinion has an arbitrarily large influence coefficient. When both opinions are present, the overall influence of opinions on disease spread is not determined by the two influence coefficients alone; instead, it arises from a complex interaction between the dynamics of the two opinions.

We plot the final epidemic size minus the basic size in Figure 3.8 for different values of the opinion transmission rates and opinion recovery rates. For fixed opinion recovery rates, the final epidemic size does not change much as we vary the opinion transmission rates if the information layer has an outbreak. The results in Figure 3.8 are outputs of our PA on 5-regular configuration-model graphs.

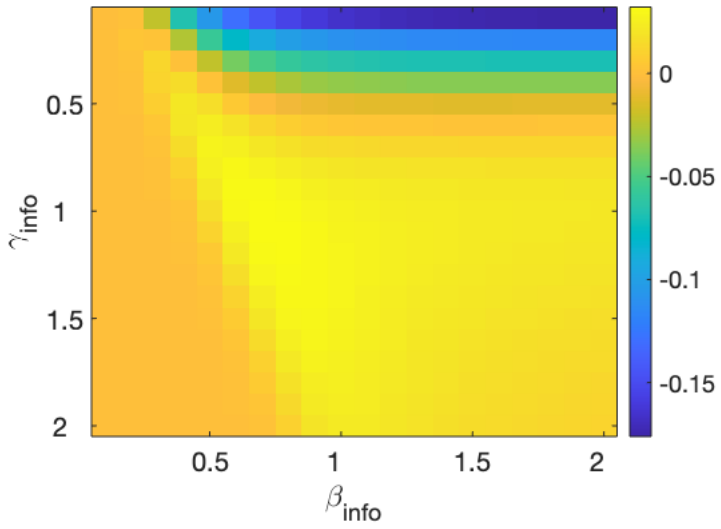

Figure 3.8: The final epidemic size minus the basic size for different values of the opinion contagion parameters for our PA on networks with layers that consist of 5-regular configuration-model graphs. We fix the other parameters to be $\beta_{\text{phy}} = 0.6$, $\gamma_{\text{phy}} = 1$, $\alpha_{\text{anti}} = 10$, and $\alpha_{\text{pro}} = 0.1$.

3.6.2 Random graphs with intralayer degree–degree correlations

Degree assortativity can have a strong impact on disease spread and other dynamical processes [KGK08, MPM14]. Assortative networks may have a core with large-degree nodes, so a disease may spread faster but terminate with a smaller final epidemic size on such a network than on a disassortative network [NG03, MGP03]. In this subsection, we investigate how differences in assortativity structure, which we encode in an intralayer degree–degree correlation matrix, can influence the dynamics of our model.

For all experiments in this subsection, we generate networks with intralayer degree–degree correlations using a model from Melnik et al. [MPM14]. For each of the two layers in the network, we start with a mixing matrix E. Recall that the number of edges that connect nodes with degrees k and k' is $\mathcal{E}_{k,\,k'} = E_{k,k'} \sum_k (kp_k) N/2$, where $p_k = \left(\sum_{k'} \frac{E_{k,\,k'}}{k}\right) \Big/ \left(\sum_{k,\,k'} \frac{E_{k,\,k'}}{k}\right)$. We first create the required number of edges that will connect node pairs with specified combinations of the degrees k and k'. We then generate nodes by selecting k ends of edges

uniformly at random from those that are prescribed to attach to degree-k nodes. We obtain networks with the desired degree–degree correlation when we finish attaching all ends of edges to nodes.

Because we track the expected number of edges with all possible degree combinations explicitly and separately in our PA system, we only need to modify the initialization step to encode the desired intralayer degree–degree correlation. For example, we let $[U_k \circ P_l](0) = \mathcal{E}_{\text{info},\,k,\,l} \times (1 - P_0 - A_0)P_0$, where $\mathcal{E}_{\text{info},\,k,\,l}$ denotes the number of edges that connect degree-k and degree-l nodes in the information layer. We initialize the physical layer and the information layer independently, so $[U_{k_1} S_{k_2} \circ P_l](0) = [U_{k_1} \circ P_l](0) \times \mathbb{P}_{\text{phy}}(k_2) \times (1 - I_0)$. We initialize the other dyads similarly.

3.6.2.1 Pedagogical example: Networks whose nodes have one of two possible degrees

To illustrate the importance of intralayer degree–degree correlations, we consider a simple example of a network whose nodes have one of two possible degrees. Its degree distribution is $\mathbb{P}(k = k_1) = p_1$ and $\mathbb{P}(k = k_2) = p_2$, where $p_1 + p_2 = 1$. The mixing matrix is

$$E = \begin{bmatrix} a & \frac{k_1 p_1}{\langle k \rangle} - a \\ \frac{k_1 p_1}{\langle k \rangle} - a & \frac{k_2 p_2 - k_1 p_1}{\langle k \rangle} + a \end{bmatrix} , \tag{3.8}$$

where $a \in \left[\max\left\{0, \frac{k_1 p_1 - k_2 p_2}{\langle k \rangle}\right\}, \frac{k_1 p_1}{\langle k \rangle} \right]$ and $\langle k \rangle$ denotes the mean degree. We calculate the assortativity coefficient r_{intra}, which is given by the Pearson correlation coefficient of the degrees at the two ends of an edge that we choose uniformly at random. Given the mixing matrix (3.8), the assortativity coefficient r_{intra} is linear in a and is given by

$$r_{\text{intra}} = \frac{a - k_1^2 p_1^2 / \langle k \rangle^2}{k_1 k_2 p_1 p_2 / \langle k \rangle^2} .$$

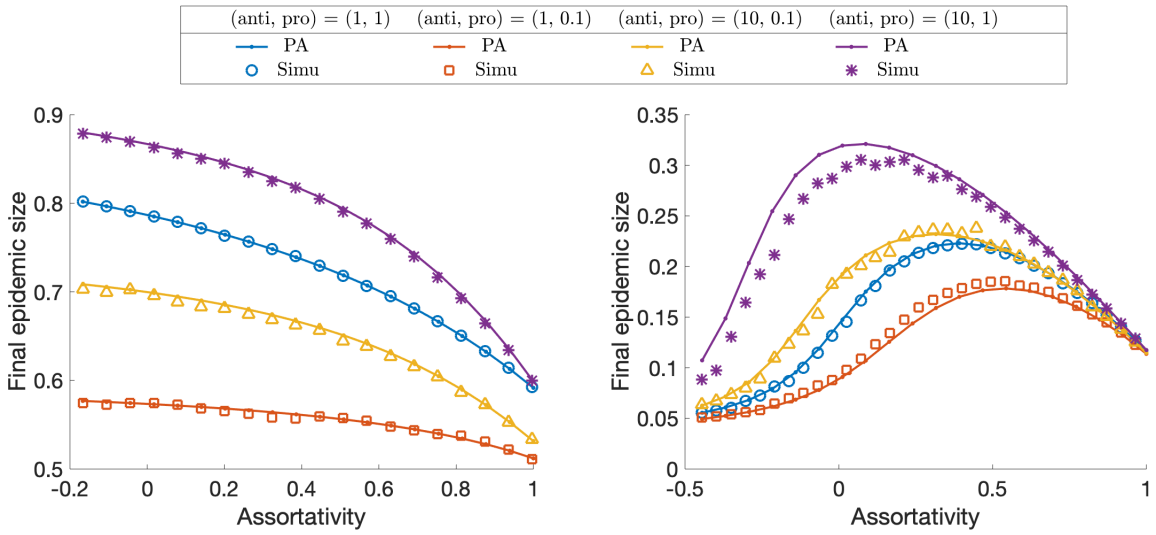

(a) $\mathbb{P}_{\text{info}}(k = 2) = \mathbb{P}_{\text{phy}}(k = 2) = 0.4$ (b) $\mathbb{P}_{\text{info}}(k = 2) = \mathbb{P}_{\text{phy}}(k = 2) = 0.9$

Figure 3.9: The final epidemic size depends on the intralayer degree–degree correlations. We generate each layer independently using a generalization of a configuration-model network with the procedure that we described in the text. Each layer consists of nodes with degrees 2 and 8, and the intralayer degree–degree correlation is the same in the two layers. The other parameters are $\beta_{\text{phy}} = \beta_{\text{info}} = 0.6$, $\gamma_{\text{phy}} = 1$, and $\gamma_{\text{info}} = 0.1$. The curves (respectively, markers) indicate results from our PA (respectively, from means of 200 direct simulations).

Figure 3.9 shows two typical sets of curves for the final epidemic size for different values of the intralayer degree–degree correlation. We fix $k_1 = 2$ and $k_2 = 8$, and we assign a fraction 0.4 of the nodes to have degree 2 in Figure 3.9(a) and a fraction 0.9 of them to have degree 2 in Figure 3.9(b). We set the intralayer degree–degree correlations to be the same in the two layers. The blue circles indicate the influence of degree assortativity on disease spread when the disease spreads independently of opinions. The decreasing trend in Figure 3.9(a) and in the right part of Figure 3.9(b) is consistent with the known result [MGP03, KGK08] that a disease tends to affect a smaller fraction of a population in an assortative network than in a disassortative network when an epidemic outbreak occurs. The increasing trend in the left part of Figure 3.9(b) arises from the fact that the disease is initially impeded from spreading because of the disassortative structure and a denser network helps the disease to

spread and persist. Similar trends also occur in the information layer, so if outbreaks do occur on both layers, an opinion contagion has a smaller impact when networks have a larger degree assortativity (as we see in both panels of Figure 3.9). In Figure 3.10, we compare the disease prevalence curves with and without the influence of each opinion for networks with $\mathbb{P}_{\text{info}}(k = 2) = \mathbb{P}_{\text{phy}}(k = 2) = 0.4$. The results demonstrate that disassortative structures tend to enhance the influence of both pro- and anti-physical-distancing opinions. When both opinions have nontrivial effects on the transmission of a disease, the overall effect of the opinion dynamics on the disease dynamics is a complicated combination of the dynamics of the opinions; in this situation, it is unclear whether an assortative or a disassortative structure promotes the spread of the disease.

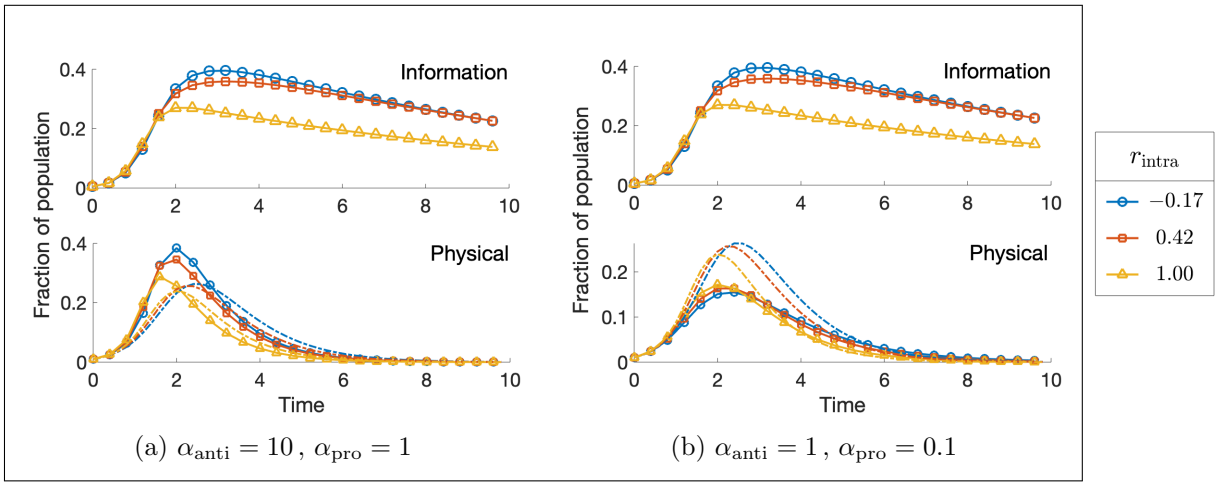

(a) $\alpha_{\text{anti}} = 10$, $\alpha_{\text{pro}} = 1$ (b) $\alpha_{\text{anti}} = 1$, $\alpha_{\text{pro}} = 0.1$

Figure 3.10: Prevalence curves from our PA for different intralayer degree–degree correlations in networks with $\mathbb{P}_{\text{info}}(k = 2) = \mathbb{P}_{\text{phy}}(k = 2) = 0.4$ and $\mathbb{P}_{\text{info}}(k = 8) = \mathbb{P}_{\text{phy}}(k = 8) = 0.6$. We generate each layer independently using a generalization of a configuration-model network with the procedure that we described in the text. The upper row shows the (identical) dynamics of the fraction of individuals in states P and A. The lower row shows the dynamics of the population in state I. The solid curves show results when (left) $\alpha_{\text{anti}} = 10$ and $\alpha_{\text{pro}} = 1$ and (right) $\alpha_{\text{anti}} = 1$ and $\alpha_{\text{pro}} = 0.1$. The dashed curves indicate results without any opinion contagion. The other parameters are $\beta_{\text{phy}} = \beta_{\text{info}} = 0.6$, $\gamma_{\text{phy}} = 1$, and $\gamma_{\text{info}} = 0.1$. Curves with the same color share all parameters except opinion influence coefficients.

The intralayer degree–degree correlations in the two layers need not be the same. Figure 3.11 shows heat maps of the final epidemic size from our PA for different values of the two

degree–degree correlations, which we vary independently in each layer. The issuance of a stay-at-home order may lead to a physical layer with many small-degree nodes, and such an order is not likely to affect the information layer (which may describe online contacts). Therefore, we also consider the case with $\mathbb{P}_{\text{info}}(k = 2) = 0.4$ and $\mathbb{P}_{\text{phy}}(k = 2) = 0.9$. We show the results for this case in the third row of Figure 3.11. In this example, the physical-layer network structures have a stronger influence on the disease dynamics than the information-layer network structures.

3.6.3 Random graphs with cross-layer correlations of intralayer degrees

We also investigate the influence of cross-layer correlations of intralayer degrees on the dynamics. We refer to such correlations as "interlayer degree–degree correlations". People who are active on social-media platforms may also have frequent offline social contacts, and vice versa [Aca08]. Let C denote the interlayer degree–degree correlation matrix, so $C_{k_1,\,k_2}$ is the probability that a node that we choose uniformly at random has degree k_1 in the information layer and degree k_2 in the physical layer. We say that these nodes are "of type $(k_1,\, k_2)$". An uncorrelated model corresponds to $C_{k_1,\,k_2} = \mathbb{P}_{\text{info}}(k_1)\mathbb{P}_{\text{phy}}(k_2)$. We uniformly randomly pair $N \times C_{k_1,\,k_2}$ degree-k_1 nodes from the information layer with the same number of degree-k_2 nodes from the physical layer to construct a network with N nodes and a specified interlayer degree–degree correlation.

A PA can deal with interlayer degree–degree correlations properly as long as we build them into the initial conditions. The modification of the PA is straightforward. For example, we write

$$\begin{aligned}
[U_{k_1} S_{k_2}](0) &= C_{k_1,k_2}(1 - A_0 - P_0)(1 - I_0)\,, \\
[U_{k_1} S_{k_2} \circ I_l](0) &= [S_{k_2} \circ I_l](0) \times \frac{C_{k_1,k_2}}{\mathbb{P}_{\text{phy}}(k_2)} \times (1 - A_0 - P_0)\,.
\end{aligned}$$

We use similar formulas for the other pairs.

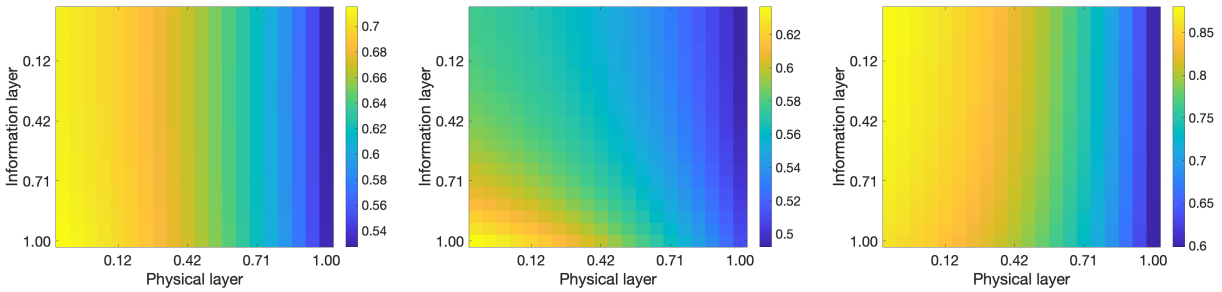

(a) $\mathbb{P}_{\text{info}}(k = 2) = \mathbb{P}_{\text{phy}}(k = 2) = 0.4$

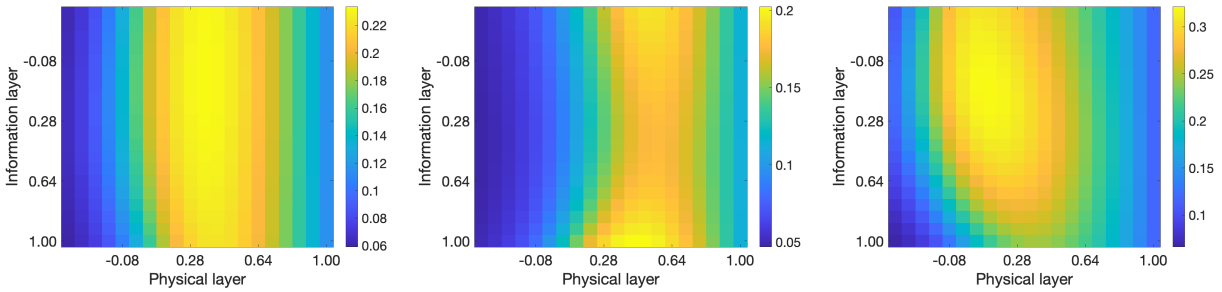

(b) $\mathbb{P}_{\text{info}}(k = 2) = \mathbb{P}_{\text{phy}}(k = 2) = 0.9$

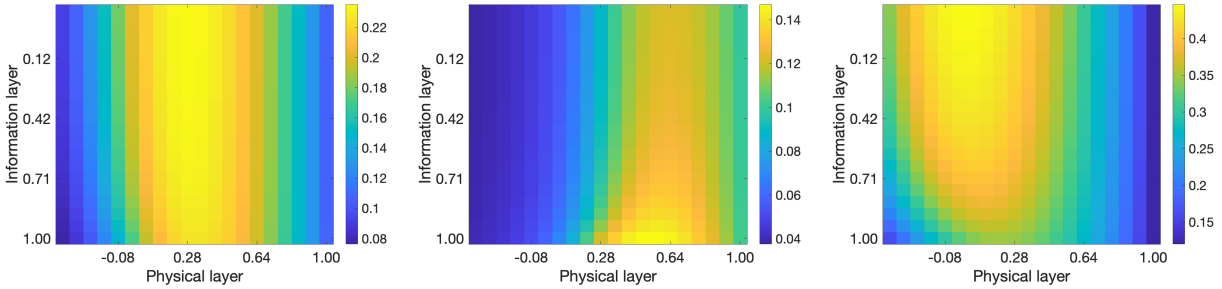

(c) $\mathbb{P}_{\text{info}}(k = 2) = 0.4$, $\mathbb{P}_{\text{phy}}(k = 2) = 0.9$

Figure 3.11: Heat maps of the final epidemic size from our PA as we vary the assortativities in the two layers. The three columns have parameter values of (left) $\alpha_{\text{pro}} = 0.1$ and $\alpha_{\text{anti}} = 10$, (center) $\alpha_{\text{pro}} = 0.1$ and $\alpha_{\text{anti}} = 1$, and (right) $\alpha_{\text{pro}} = 1$, and $\alpha_{\text{anti}} = 10$. The other parameters are $\beta_{\text{phy}} = \beta_{\text{info}} = 0.6$, $\gamma_{\text{phy}} = 1$, and $\gamma_{\text{info}} = 0.1$.

3.6.3.1 Pedagogical example: Networks whose nodes have one of two possible degrees

We again suppose that nodes have one of two possible degrees in each layer. These degrees are $k_{\text{info},1}$, $k_{\text{info},2}$, $k_{\text{phy},1}$, and $k_{\text{phy},2}$, where $\mathbb{P}_{\text{info}}(k = k_{\text{info},1}) = q_1$ and $\mathbb{P}_{\text{phy}}(k = k_{\text{phy},1}) = q_2$.

The correlation matrix C is

$$\begin{bmatrix} a & q_1 - a \\ q_2 - a & 1 - q_1 - q_2 + a \end{bmatrix}, \tag{3.9}$$

where $a \in [\min\{0,\, q_1 + q_2 - 1\},\, \min\{q_1,\, q_2\}]$. The Pearson correlation coefficient is

$$r_{\text{inter}} = \frac{(k_{\text{info},\,1} - k_{\text{info},\,2})(k_{\text{phy},\,1} - k_{\text{phy},\,2})(a - q_1 q_2)}{\sigma_{\text{info}}\sigma_{\text{phy}}},$$

where σ_{info} and σ_{phy} denote the standard deviations of the degrees in the two layers.

Figure 3.12 shows the dependence of the final epidemic size on the interlayer degree–degree correlations. Each of the two layers has nodes of degrees 2 and 8, and we set $\mathbb{P}_{\text{info}}(k = 2) = \mathbb{P}_{\text{phy}}(k = 2) = 0.5$. We generate each layer independently with a generalization of a configuration-model network following the procedure in Section 3.6.2. We suppose either that both intralayer degree–degree correlations are 1 or that both intralayer degree–degree correlations are -0.25, and we couple the two layers as described above.[1] The pro-physical-distancing opinion has a larger influence when the two layers are more positively correlated. (See the red curves with square markers.) However, the anti-physical-distancing opinion's influence can either decrease or increase as we increase the interlayer degree–degree correlation. (See the purple curves with asterisk markers.)

To understand the trends in Figure 3.12, we again decompose the population based on their opinion states (see Figure 3.13). Recall that $\mathcal{U}$, $\mathcal{A}$, $\mathcal{P}$, and $\mathcal{R}$ denote the subpopulations that become infectious when they are in the U, A, P, and R_{info} states, respectively. Additionally, we decompose the $\mathcal{U}$ and $\mathcal{A}$ subpopulations based on node degrees and plot the fraction of the population in each group in Figure 3.14. We examine the effects of positive intralayer degree–degree correlations in Figures 3.13(a) and 3.14(a,c), and we examine the effects of negative intralayer degree–degree correlations in Figures 3.13(b) and 3.14(b,d). In our dis-

[1] A layer with an intralayer degree–degree correlation of 1 has more than one component.

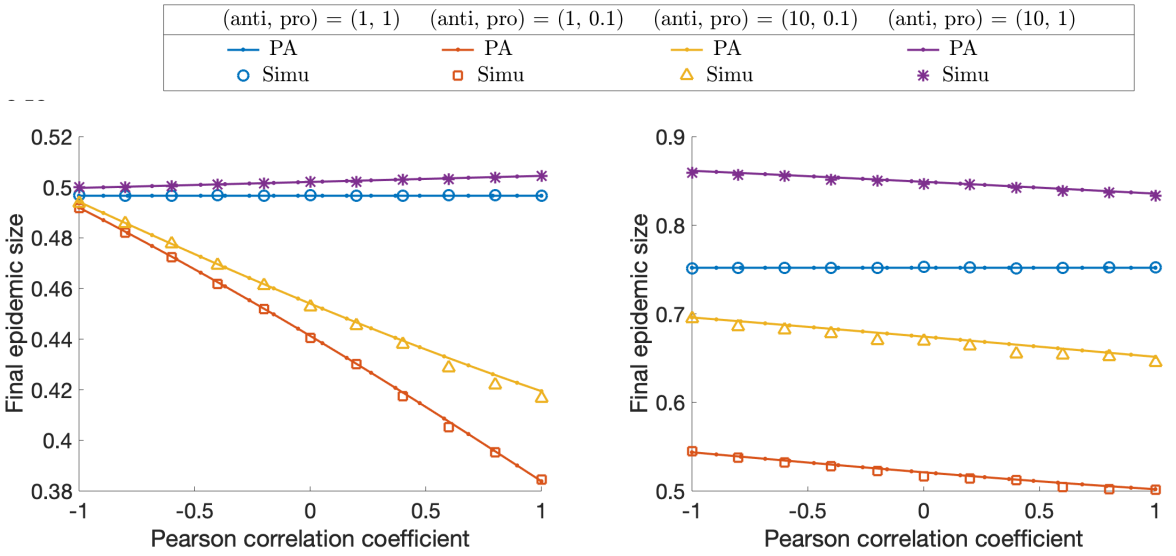

(a) $r_{\text{intra}} = 1$ (b) $r_{\text{intra}} = -0.25$

Figure 3.12: The final epidemic size depends on the interlayer degree–degree correlation. Both layers have nodes of degrees 2 and 8, and we set $\mathbb{P}_{\text{info}}(k = 2) = \mathbb{P}_{\text{phy}}(k = 2) = 0.5$. We generate each layer using the procedure in Section 3.6.2. We couple the two layers following the approach in Section 3.6.3. We set the intralayer degree–degree correlation of both layers to be (a) 1 and (b) -0.25. The other parameters are $\beta_{\text{phy}} = \beta_{\text{info}} = 0.6$, $\gamma_{\text{phy}} = 1$, and $\gamma_{\text{info}} = 0.1$. The curves (respectively, markers) show results from our PA (respectively, from means of 200 direct simulations).

cussion, it is instructive to consider the case of two independent layers (i.e., $\alpha_{\text{pro}} = \alpha_{\text{anti}} = 1$). The interlayer degree–degree correlation changes the opinion distributions, but the final epidemic size stays the same. We investigate the influence of opinions and how this influence depends on the interlayer degree–degree correlation.

We first examine the case in which the intralayer degree–degree correlation is 1 and node opinions do not affect the spread of the disease. A positive interlayer degree–degree correlation encourages the coupling of large-degree nodes in the two layers; these nodes have larger probabilities than small-degree nodes both of becoming infected and of forming an opinion. Therefore, as we increase the interlayer degree–degree correlation, fewer nodes are uninformed when they catch the disease. Figure 3.14(a) shows the decomposition of the $\mathcal{U}$

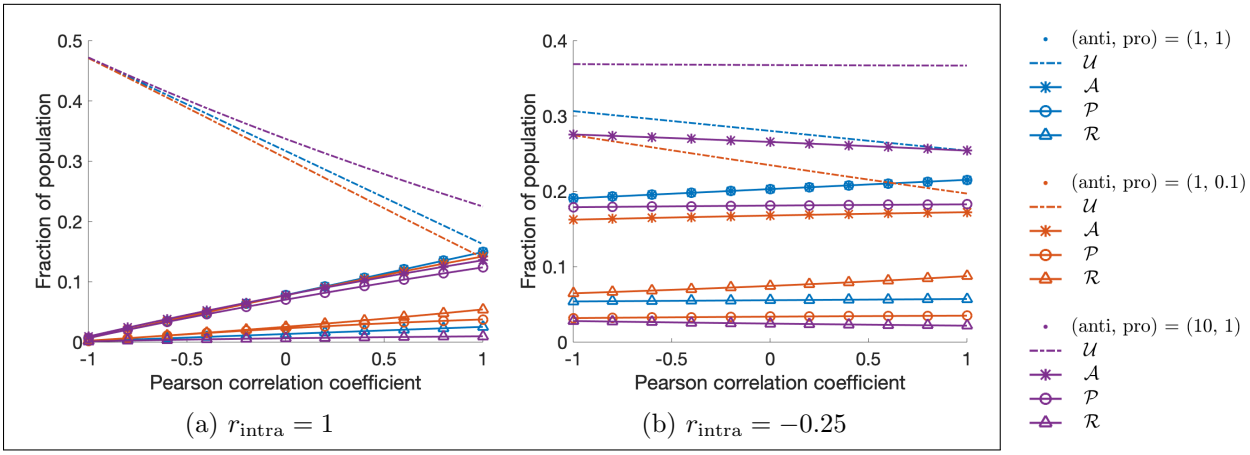

Figure 3.13: Decomposition of the opinion states of nodes that eventually become infected and recover. We group the recovered population based on their opinion states when they become infectious. Recall that the associated subpopulations are $\mathcal{U}$, $\mathcal{P}$, $\mathcal{A}$, and $\mathcal{R}$. The vertical axis indicates the fraction of the population in each of these subpopulations. We plot the subpopulation sizes versus the interlayer degree–degree correlation from our PA. The intralayer degree–degree correlation is (a) 1 and (b) -0.25. The other parameters are $\beta_{\text{phy}} = \beta_{\text{info}} = 0.6$, $\gamma_{\text{phy}} = 1$, and $\gamma_{\text{info}} = 0.1$.

subpopulation based on the degrees of its nodes. Because the degree-2 nodes are adjacent only to other degree-2 nodes in each layer, they are rarely infected and rarely form an opinion. Therefore, the $\mathcal{U}$ subpopulation consists primarily of nodes of types (2, 8) or (8, 8). As we increase the interlayer degree–degree correlation, there are more (8, 8)-type nodes and fewer (2, 8)-type nodes in the network. Because U_8-nodes (i.e., nodes that are uninformed and have degree 8 in the information layer) have a larger probability of forming an opinion than U_2-nodes, fewer nodes become infected while still uninformed as we increase the correlation.

If we perturb the influence coefficients α_{anti} and α_{pro} from 1, the opinions on the information layer directly affect the $\mathcal{A}$ and $\mathcal{P}$ subpopulations, respectively, through modified infection risks. These modified risks then influence the speed of disease spread and affect the other subpopulations. Therefore, the information layer has a larger affect on the disease dynamics when more people become infected while holding some opinion. Based on our discussion above, we expect that increasing the interlayer degree–degree correlation amplifies

the influence of opinion spread on disease dynamics.

We now examine the case in which either the pro-physical-distancing opinion or the anti-physical-distancing opinion has a nontrivial influence on disease dynamics. For simplicity, we suppose that only one opinion is effective. When $\alpha_{\text{pro}} < 1$, the spread of the pro-physical-distancing opinion protects people who adopt that opinion because it suppresses the spread of the disease. In Figure 3.13(a), we see that the $\mathcal{U}$ subpopulation tends to decrease faster and that the $\mathcal{P}$ and $\mathcal{A}$ subpopulations tend to increase slower in this situation than when the disease spreads independently of opinions. Therefore, the final epidemic size decreases as we increase the interlayer degree–degree correlation. When $\alpha_{\text{anti}} > 1$, the anti-physical-distancing opinion accelerates the spread of the disease. Therefore, more people become infected before their opinions change; this, in turn, leads to a larger $\mathcal{U}$ subpopulation and smaller $\mathcal{A}$, $\mathcal{P}$, and $\mathcal{R}$ subpopulations. The growing gap between the dashed purple curve and the dashed blue curves (i.e., the $\mathcal{U}$ subpopulation for different parameter values) in Figure 3.13(a) illustrates the increase in the epidemic size as we increase the interlayer degree–degree correlation.

The situation is more intricate when the intralayer degree–degree correlation is -0.25 in each layer. Because the intralayer edges now can connect degree-2 nodes to degree-8 nodes, the former are more likely both to become infectious and to adopt an opinion than when the intralayer degree–degree correlations are 1. Therefore, when $\alpha_{\text{anti}} = \alpha_{\text{pro}} = 1$, nodes of types (8, 2) and (2, 2) constitute a larger proportion of the $\mathcal{U}$ subpopulation in Figure 3.14(b) than in Figure 3.14(a). As we increase the interlayer degree–degree correlation, the $\mathcal{U}$ subpopulation has progressively more nodes with degree 2 in the physical layer because there are gradually fewer (8, 2)-type nodes and gradually more (2, 2)-type nodes and it is more difficult for the (2, 2)-type nodes to form an opinion. Consequently, the decreasing trend in the $\mathcal{U}$ subpopulation (see the dashed blue curve) in Figure 3.13(b) is less drastic than in Figure 3.13(a).

When $\alpha_{\text{anti}} > 1$, the $\mathcal{A}$ subpopulation in Figure 3.13(b) (see the purple curve with asterisk

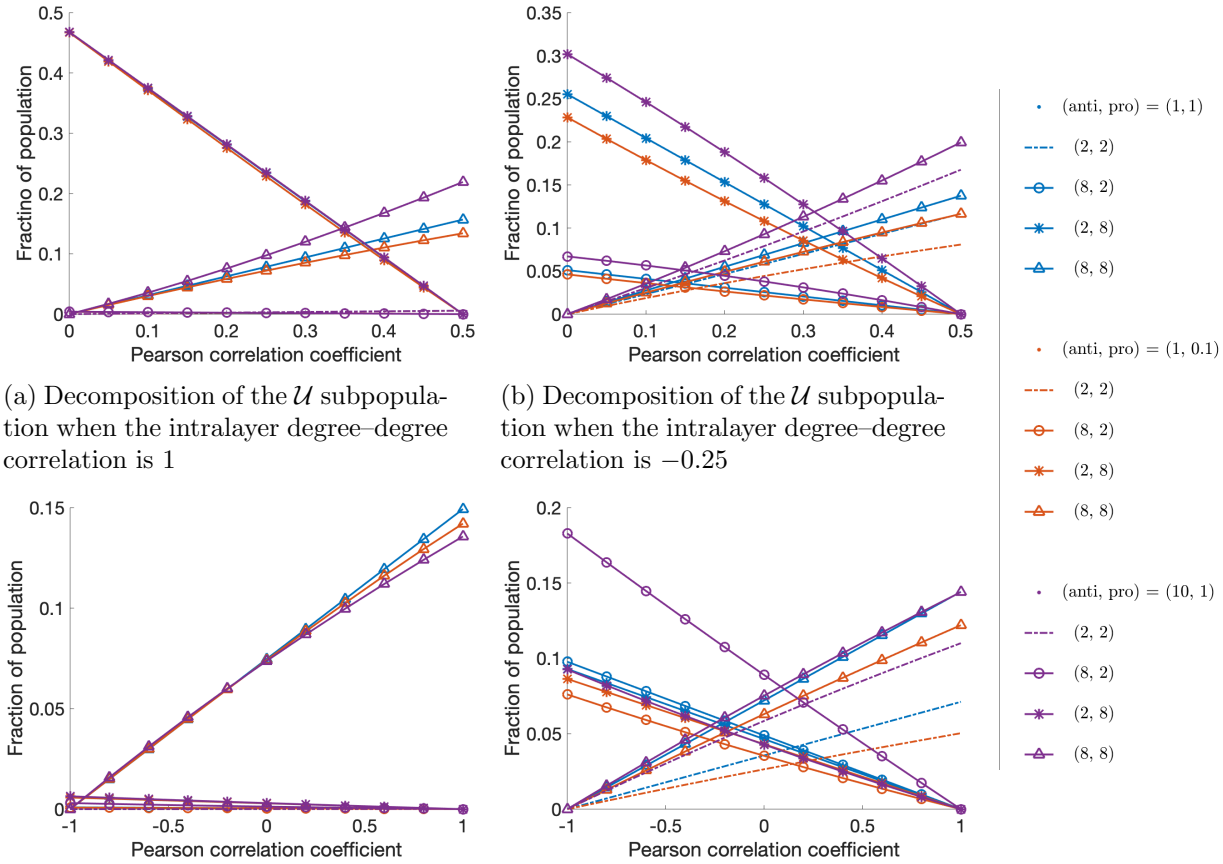

(a) Decomposition of the $\mathcal{U}$ subpopulation when the intralayer degree–degree correlation is 1

(b) Decomposition of the $\mathcal{U}$ subpopulation when the intralayer degree–degree correlation is -0.25

(c) Decomposition of the $\mathcal{A}$ subpopulation when the intralayer degree–degree correlation is 1

(d) Decomposition of the $\mathcal{A}$ subpopulation when the intralayer degree–degree correlation is -0.25

Figure 3.14: Decomposition based on the degrees of the nodes that eventually become infectious and recover. We decompose (a, b) the $\mathcal{U}$ subpopulation and (c, d) the $\mathcal{A}$ subpopulation by degree. The vertical axes indicate the fraction of the population in each subpopulation. We show the changes in subpopulation size versus the interlayer degree–degree correlation from our PA. The other parameters are $\beta_{\text{phy}} = \beta_{\text{info}} = 0.6$, $\gamma_{\text{phy}} = 1$, and $\gamma_{\text{info}} = 0.1$.

markers) has qualitatively different dynamics than in Figure 3.13(a). This difference arises from the influence of opinions on degree-2 nodes in the physical layer. Nodes that adopt the anti-physical-distancing opinion now have a larger infection risk than when $\alpha_{\text{anti}} = 1$, so we expect more nodes to become infected while holding the anti-physical-distancing opinion. In Figure 3.14(d), we see that the anti-physical-distancing opinion leads to an increase in

the numbers of nodes of types (8, 2) and (2, 2) in the $\mathcal{A}$ subpopulation as we increase α_{anti} from 1 to 10. Moreover, as we increase α_{anti} from 1 to 10, the increase in the number of (8, 2)-type nodes in the $\mathcal{A}$ subpopulation when the interlayer degree–degree correlation is -1 is larger than the increase in the number of (2, 2)-type nodes in that population when the interlayer degree–degree correlation is 1. This phenomenon arises because degree-8 nodes are more likely than degree-2 nodes to adopt an opinion. This, in turn, leads to a decrease of the $\mathcal{A}$ subpopulation and ultimately to a decrease of the total epidemic size as we increase the interlayer degree–degree correlation. The anti-physical-distancing opinion does not lead to a clear increase in the number of the degree-8 nodes in the $\mathcal{A}$ subpopulation. One plausible explanation is that the degree-8 nodes are already very likely to become infected at the baseline transmission rate of the disease. Additionally, the anti-physical-distancing opinion does not lead to an increase in the number of nodes of types (8, 2) or (2, 2) when the intralayer degree–degree correaltion is 1 (see Figure 3.14(c)). We conjecture that this is because the positive intralayer degree–degree correlation imposes sufficiently strong constraints so that it is difficult for nodes with degree 2 in the physical layer to become infected even when the transmission rate is high.

3.7 Modeling temporary immunity to opinions

In previous sections, we assumed that people who adopt a pro- or anti-physical-distancing opinion develop immunity to both opinions after they recover. More generally, the opinions of individuals can change back and forth [GF20]. In this section, we extend the opinion dynamics to an SIRS process (see Figure 3.15). With conversion rate τ, people in the R_{info} compartment return to the U compartment and again become susceptible to the pro- and anti-physical-distancing opinions. When $\tau = 0$, this refined model reduces to the model in Section 3.3 (see Figure 3.1).

Figure 3.16 shows the final epidemic size minus the basic size as we vary the contagion

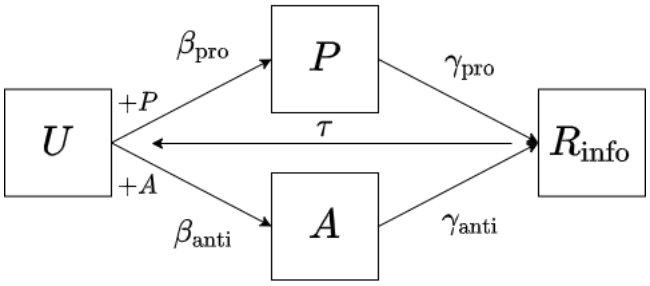

Figure 3.15: Schematic illustration of the dynamics on the information layer with temporary immunity to opinions. The transitions are the same as in Figure 3.1, except that nodes in state R_{info} transition to state U at rate τ.

parameters τ, γ_{info}, and β_{info} in direct simulations of our refined model. For fixed values of τ, we obtain a heat map similar to the one in Figure 3.8. As we increase τ, our simulations suggest that there is an increase in the overall influence from the information layer. For fixed values of γ_{info} and β_{info}, the colors in the heat map become brighter (respectively, darker) from left to right because the spread of opinions leads to a decrease (respectively, increase) in the final epidemic size in comparison to the basic size as we increase τ.

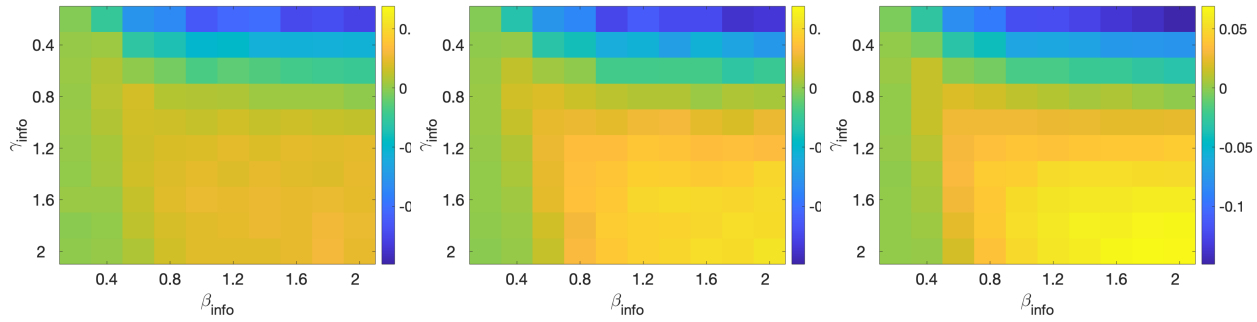

(a) $\tau = 0$ (b) $\tau = 1$ (c) $\tau = 2$

Figure 3.16: The final epidemic size minus the basic size as we vary γ_{info}, β_{info}, and τ in direct simulations of our refined model. We generate each layer using a configuration-model network with a Poisson degree distribution with a mean degree of 5. The other parameters are $\beta_{\text{phy}} = 0.6$, $\gamma_{\text{phy}} = 1$, $\alpha_{\text{anti}} = 10$, and $\alpha_{\text{pro}} = 0.1$. Each panel is a mean of 600 simulations.

Consider the case $\beta_{\text{info}} = 2$, where the effect of τ is particularly evident. Figure 3.17(a) shows the influence of τ on the final epidemic size for a few values of γ_{info}. It is hard to see

the trend when $\gamma_{\text{info}} = 1$ because of the stochasticity of the simulations, but the behavior of the other three curves is consistent with that of Figure 3.16. As we increase τ, there is a decrease in the expected duration that individuals stay in the R_{info} state. Consequently, as we increase τ in Figure 3.17(b), there is a decrease in the size of the $\mathcal{R}$ subpopulation and an increase in the sizes of the other subpopulations ($\mathcal{U}$, $\mathcal{A}$, and $\mathcal{P}$).

We conjecture that the overall influence (i.e., whether increasing τ leads to more or fewer disease infections) depends on whether or not people tend to adopt an opinion that departs from their earlier opinion(s). If individuals tend to adopt different opinions over time, increasing τ makes the model with SIRS opinion dynamics exhibit behavior that resembles what we observed after applying the random-recoupling assumption (see Section 3.4) and leads to more people adopting the anti-physical-distancing opinion at an earlier time. Susceptible individuals are likely to become infected when they adopt the anti-physical-distancing opinion, regardless of whether or not they have previously adopted the pro-physical-distancing opinion. Consequently, increasing τ leads to more disease infections. However, if people tend to adopt the same opinion over time, susceptible individuals who adopt the pro-physical-distancing opinion also are more likely to avoid future infections. In this case, enforcing a faster reversion to the U state has a similar effect as decreasing γ_{info}, which (as we showed in Section 3.6.1) may help suppress disease spreading. Figure 3.17(c) shows the fractions of individuals who adopt (i) both opinions and (ii) at least one opinion within the time frame of our experiments for $\gamma_{\text{info}} = 0.2$ and $\gamma_{\text{info}} = 2$. Many fewer people adopt both opinions when $\gamma_{\text{info}} = 0.2$ than when $\gamma_{\text{info}} = 2$. Additionally, as we increase τ, there is only a slightly increasing trend in the fraction of people who adopt both opinions for $\gamma_{\text{info}} = 0.2$, in contrast to the rapid growth of the fraction for $\gamma_{\text{info}} = 2$. Intuitively, a node that adopts one opinion can influence more neighbors when γ_{info} is smaller. Therefore, it is more likely to adopt the same opinion later. Suppose that a node holds an opinion when it becomes infected on the physical layer, and suppose that this is not the first opinion that it has held (i.e., it previously returned to the U state in the information layer). In Figure 3.17(d), we examine the counts

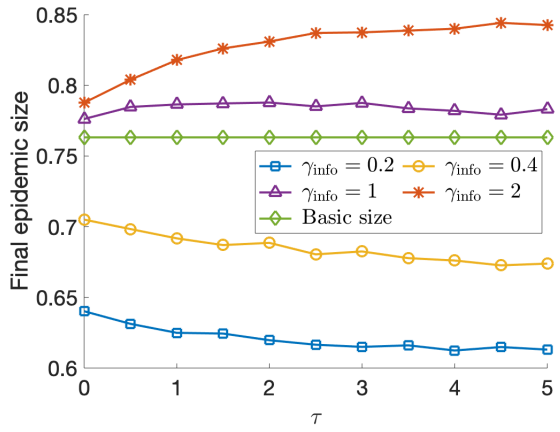

(a) Final epidemic size

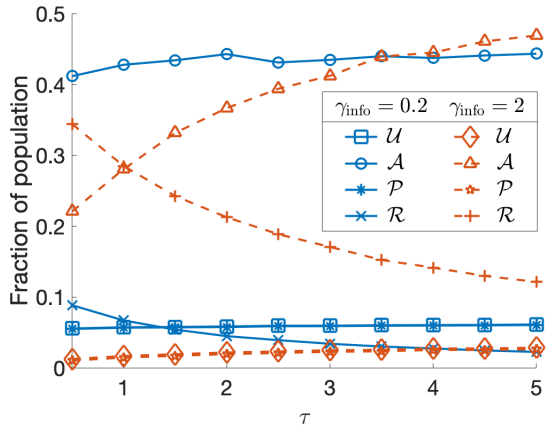

(b) Decomposition of opinion states

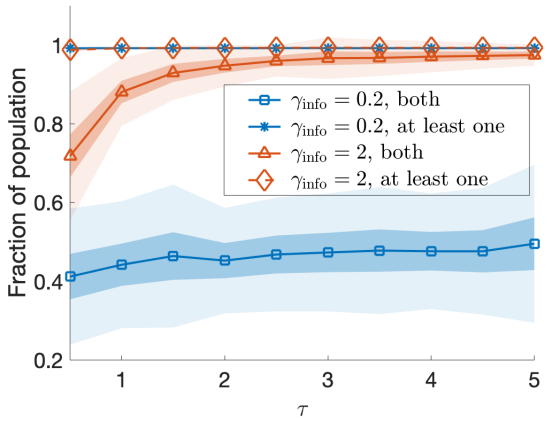

(c) Fractions of the population that adopt (i) both opinions and (ii) at least one opinion

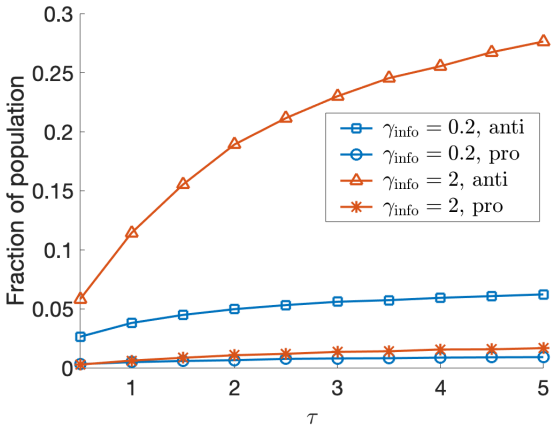

(d) Fractions of the population that are infected during their second or subsequent time that they adopt an opinion (the second and subsequent opinions need not be the same as prior opinions)

Figure 3.17: Influence of the opinion recovery rate γ_{info} and the conversion rate τ on the final epidemic size and on the opinion distribution when we consider SIRS dynamics in the information layer. (a) The influence of τ on the final epidemic size. We decompose the recovered population based on their opinion states when they become infected and plot the sizes of these subpopulations in (b). In (c, d), we show additional opinion-distribution statistics; we specify them in the subtitles. We generate each layer using a configuration model with a Poisson degree distribution with a mean degree of 5. The curves show means of 200 direct simulations with $\beta_{\text{phy}} = 0.6$, $\gamma_{\text{phy}} = 1$, $\beta_{\text{info}} = 2$, $\alpha_{\text{pro}} = 0.1$, and $\alpha_{\text{anti}} = 10$.

of these individuals for both opinions as a function of τ. Consistent with our conjecture, as we increase τ, we observe a larger increase of the fraction of the population that holds the

anti-physical-distancing opinion when $\gamma_{\text{info}} = 2$ than when $\gamma_{\text{info}} = 0.2$.

3.8 Conclusions and discussion

We studied the influence of the spread of competing opinions on the spread of a disease. We assumed that pro- and anti-physical-distancing opinions circulate within a population and affect the spread of the disease. We developed a degree-based pair approximation for the time evolution of the expected number of individuals in different compartments and used it to study dynamics on heterogeneous networks with specified interlayer and intralayer degree–degree correlations. We examined different approximation schemes for the effective transmission rate of susceptible individuals in the physical layer. We found that the distribution of the opinions of the nodes in a given disease state is correlated both with their own disease state and with the disease states of their neighbors in the physical layer.

Through extensive numerical simulations, we showed that the opinion contagions in our model can either increase or decrease the disease transmission speed, the peak infection counts, and the number of people who become infected. We demonstrated that the overall impact of the opinion dynamics on disease prevalence depends not only on the opinion influence coefficients, but also on the network structure and on how the opinions couple to the spread of the disease.

We found that lengthening the duration (through decreasing the opinion recovery rate) over which people adopt opinions — whether in favor of or against physical distancing — may help suppress disease transmission. We also saw that physically distancing for too short a duration may still entail a high infection risk; this is well-known for models of infectious disease with a fully-mixed population [BF07, BFM20]. We observed that the benefit of a long opinion-adoption period is reinforced when we let the spread of opinions follow SIRS dynamics instead of SIR dynamics. Allowing people to become susceptible to opinions after having a previous opinion helps create neighborhoods in a network's information layer in

which adjacent nodes tend to adopt the same opinion over time. Consequently, people who adopt the pro-physical-distancing opinion are more likely to adopt it again later. Although the same phenomenon applies to the spread of the anti-physical-distancing opinion, the difference in the influence of the two opinions on disease transmission rates leads to an asymmetry in their influence on disease prevalence.

We examined both beneficial and harmful effects of the spread of opinions on other dynamical processes (such as the spread of a disease). There are many ways to build on our research. Although two competing opinions can have different contagion parameters, we only showed results in which these parameters are identical. One can study our model when the two competing opinions spread asymmetrically. We also assumed a unidirectional influence from the information layer to the physical layer, but disease states can also influence opinion states [FSJ10, WAW15], and one can incorporate such coupling. Additionally, time-dependent network structures in which node states coevolve with network structures [SPS13, PG16] are relevant for behavioral changes when individuals adopt opinions about physical distancing. Such time-dependent networks allow one to model changes in contact patterns due to lockdowns and stay-at-home orders. One can also consider additional opinions (e.g., opinions on vaccines) in conjunction with more complex disease dynamics due to vaccines [SVB21] and variants.

CHAPTER 4

Majority-Vote Model On Multiplex Networks with Community Structure

4.1 Introduction

In everyday life, the opinions of people who we know often influence our decisions. People may change their opinions or behavior to conform to group behavior [Asc51]. Researchers have proposed many mathematical models to study such social forces [FMF17]. One of these models is the *majority-vote model*. In the classical monolayer majority-vote model [Oli92], each node has one of two opinions. At each time step, a uniformly randomly chosen node adopts the majority opinion of its neighbors with probability $1 - f$ and adopts the minority opinion of its neighbors with probability f, where f is called the noise parameter. Researchers have adapted the majority-vote model to study financial markets [VWN19], tax envision [Lim10], and the effect of filter bubbles [VPD21].

The classical majority-vote model on a square lattice has a continuous phase transition at a critical value f_c of the noise parameter f [Oli92]. When $f < f_c$, the mean opinion of the population on the lattice is close to 0 at steady states and the two opinions are distributed uniformly in the population. This is called a "disordered" regime in the physics literature. When $f > f_c$, the system is in an "ordered" regime in which the absolute value of the mean opinion is positive and increases with f. Researchers have studied the classical majority-vote model on various networks, including ER networks [PM05, LSS08], Watts–Strogatz networks [COM03, LL07, SM15], Barabási–Albert networks [Lim06], networks with

community structure [HCS15], and several types of lattices [YKK08, WH10, SLM11, ASV14].

In our extension of the majority-vote model, we consider networks with community structure. Community structure is a common feature of social networks [POM09, FH16]. Individuals have more connections with individuals from the same community than with individuals from different communities. A large body of research has examined the influence of community structure on a variety of dynamical processes, including the majority-vote model [HCS15], the majority-rule model [LA07, LAH07], the Ising model [DPS09, BNM18], the Sznajd model [RL08], the spread of infectious diseases [LH05, WL08, SVV16], information spread using an SIR model [HPL06], and information spread using a linear threshold model [NFF14]. Huang et al. [HCS15] showed that the majority-vote model on networks with planted community structure undergoes the same continuous disorder–order transition at a critical value f_{c_1} as the majority-vote model on regular lattices. When f is smaller than and close to f_{c_1}, the entire population favors one opinion and the distribution of opinions is independent of the community memberships of the network's nodes. When the noise parameter decreases further, the system in Ref. [HCS15] undergoes a discontinuous phase transition at a second critical value f_{c_2} under certain conditions. When $f < f_{c_2}$, the mean opinions of the different communities can have different signs, which means that the different communities favor different opinions. Researchers have also observed the presence of clusters of nodes with different opinions when studying the Ising model [SH09, DPS09, BNM18] and the majority-rule model [LA07, LAH07] on networks with community structure.

Social relationships in real life are multifaceted [KAB14], and it is important to take this into account in the study of opinion dynamics. One approach is to consider opinion dynamics on multiplex networks. Each layer in a multiplex network can represent a relationship. In this scenario, it is reasonable to assume that all nodes that correspond to a physical node share the same opinion. Different relationships differ in how they are formed and maintained, and they have different levels of importance to an individual. Consequently, the opinions from disparate sources may spread following different rules. Alternatively,

layers can represent different topics and state nodes that correspond to a physical node can often have distinct opinions. Many dynamical processes on multilayer networks cannot be reduced to equivalent processes on monolayer networks that one obtains by aggregating multiplex networks [DNL16]. Researchers have studied several types of opinion dynamics on multilayer networks. Examples include the majority-vote model [KGS18, CG19], the voter model [DNL16], the q-voter model [CSS17, GK20], threshold models [LBG14], and the Deffuant–Weisbuch model [NXX18] .

In this chapter, we study steady-state behavior in a majority-vote model on multiplex networks with community structure. For simplicity, we consider two-layer networks. To incorporate community structure into our multiplex networks, we construct each layer using a stochastic block model (SBM) [New18]. We assume that each physical node holds one opinion. When the two layers have the same majority opinion, the update rules are the same as in the monolayer majority-vote model. Previous extensions of the majority-vote model to multiplex networks [KGS18, CG19] treated the two layers equally so that when majority opinions differ in different layers, a focal node either uniformly randomly adopts an opinion or maintains its current opinion. However, in real life, individuals can attach different levels of importance to different relationships or favor some social relationships over others. We model this situation by introducing a layer-preference parameter that controls the probability of adopting each opinion when the two layers do not have a common majority opinion. We study the influence of the layer-preference parameter, the intralayer communities, and interlayer membership correlations on the steady-state behavior with direct numerical simulations and with a mean-field approximation.

This chapter proceeds as follows. In Section 4.2, we introduce our majority-vote model and discuss the structure of the multiplex networks on which we consider these dynamics. We derive a mean-field approximation of our model in Section 4.3; this yields a coupled system of ODEs. In Section 4.4, we conduct linear stability analysis of three steady-state behaviors that we observe in our mean-field system. In Section 4.5, we compare the results

of direct numerical simulations with those of our mean-field approximation and explore the influence of the model parameters on the locations of our model's phase transitions. We conclude in Section 4.6.

4.2 Model

We consider a two-layer multiplex network of N physical nodes, and we suppose that all physical nodes are present in both layers. Each physical node is associated with one of two opinions (1 and -1). The two layers represent two relationships, which can be online and offline relationships, LinkedIn and Facebook friendship relationships, or something else. We label the two layers as layer 1 and layer 2. We introduce our majority-vote model in Section 4.2.1 and discuss the network structure in Section 4.2.2.

4.2.1 Majority-vote model on multiplex networks

Our extension of the majority-vote model emphasizes layer heterogeneity. Suppose that our system updates at discrete time steps. At each time step, we uniformly randomly choose a physical node. We denote its opinion by O_1 and denote the other opinion by O_2. This focal node conducts a local survey of its neighbors' opinions on each layer. There are four possible situations, which we summarize in Table 4.1. If the opinion O_1 is the common majority opinion in both layers, the chosen node flips its opinion with probability f_1. If O_1 is the majority opinion in layer 1 but not layer 2, the node changes its opinion and adopts opinion O_2 with probability f_2. If O_1 is the majority opinion in layer 2 but not in layer 1, it changes its opinion with probability $1 - f_2$. Finally, if O_1 is not the majority opinion in either layer, the focal node changes its opinion with probability $1 - f_1$. The parameter f_1 is a natural extension of the noise parameter in the classical majority-vote model, so we call it the "noise parameter" in this chapter. We only consider $f_1 < 0.5$, as nodes are more likely to follow the majority opinion. We introduce the parameter f_2 to model the situation that neighbors in

Table 4.1: The probability that a focal node changes its opinion. We denote the original opinion of the focal node by O_1 and denote the other opinion by O_2. The first column indicates the majority opinion in each layer. We use $\bar{O}_1$ to indicate that O_1 is not the majority opinion in a layer. The second column gives the probability that the focal node adopts opinion O_2.

Majority opinions		Opinion-flip probability
Layer 1	Layer 2	
O_1	O_1	f_1
O_1	$\bar{O}_1$	f_2
$\bar{O}_1$	O_1	$1 - f_2$
$\bar{O}_1$	$\bar{O}_1$	$1 - f_1$

one layer are more influential than neighbors in the other layer. We call this parameter the "layer-preference parameter". Without loss of generality, we assume that $f_2 \leq 0.5$, which implies that neighbors in layer 1 are at least as persuasive as neighbors in layer 2. When $f_2 = 0.5$, our model is similar to the model that was studied in Ref. [KGS18]; when $f_2 = 0$, our model is similar to the "AND" model that was studied in Ref. [CG19]. We also assume that $f_2 > f_1$, so a node is more likely to adopt an opinion that is the common majority opinion in both layers than an opinion that is the majority opinion in only one of the layers.

4.2.2 Multiplex networks with community structure

To incorporate community structure into our multiplex networks, we construct each layer using an SBM. For simplicity, we assume that each layer has two communities and that each community consists of $N/2$ nodes. For physical nodes, there are 4 different community labels, which we denote by $\mathbf{g} = (g_1, g_2)$, where $g_l \in \{1, 2\}$ is the label in layer l. To control the correlation of community assignments across layers, we define ν as the probability that a physical node belongs to community g (with $g \in \{1, 2\}$) in both layers. We calculate that $\mathbb{E}[|C_{(1,1)}|] = \mathbb{E}[|C_{(2,2)}|] = \nu N/2$ and $\mathbb{E}[|C_{(1,2)}|] = \mathbb{E}[|C_{(2,1)}|] = (1 - \nu)N/2$, where $C_{(g_1,g_2)}$ denotes the set of physical nodes with community label (g_1, g_2) and $\mathbb{E}[|\cdot|]$ denotes the expected

cardinality of a set. In our simulations, we independently assign each physical node to community $C_{\mathbf{g}}$ with probability $\mathbb{E}[|C_{\mathbf{g}}|]$. Without loss of generality, we assume that $\nu \geq 0.5$. One can exchange community labels in one of the two layers to obtain an equivalent model with $\nu < 0.5$. After we determine community assignments, we generate intralayer edges independently in each layer using an SBM. To do this, in each layer l, we connect two state nodes that belong to the same community with probability $p_{\text{in},l}$ and we connect two state nodes that belong to different communities with probability $p_{\text{out},l}$, where $0 < p_{\text{out},l} < p_{\text{in},l}$. We measure the strength of intralayer communities with the parameter $\mu_l = p_{\text{out},l}/(p_{\text{out},l}+p_{\text{in},l}) \in (0, 0.5)$. A smaller value of μ_l means that a larger fraction of edges connect nodes that are in the same community. We use a simplistic network structure for convenience. More realistic network structures can include more layers and more communities; each layer can have different numbers of communities of different sizes and different densities. To use such a general setting, one can impose interlayer community correlations and construct intralayer communities following Ref. [BJA20]. One can also study the influence of more sophisticated community structures, such as ones with overlapping communities.

4.3 A mean-field approximation

In this section, we derive a mean-field approximation of our majority-vote model and study its dynamics. As in Section 3.5, we group nodes with the same degrees. We denote the degree of a physical node by $\mathbf{k} = (k_1, k_2)$, where k_l is the node's degree in layer l. We also group nodes based on their community assignments. Let $q_{\mathbf{k},\mathbf{g}}$ denote the probability that a uniformly randomly chosen node with degree $\mathbf{k}$ in community $C_{\mathbf{g}}$ holds opinion 1. The probability $q_{\mathbf{k},\mathbf{g}}$ evolves as

$$\frac{d}{dt} q_{\mathbf{k},\mathbf{g}} = (1 - q_{\mathbf{k},\mathbf{g}}) P_{\mathbf{k},\mathbf{g}}^{-1\to 1} - q_{\mathbf{k},\mathbf{g}} P_{\mathbf{k},\mathbf{g}}^{1\to -1}\,, \tag{4.1}$$

where $P_{\mathbf{k},\mathbf{g}}^{O\to -O}$ is the probability that a node changes its opinion to $-O$ from opinion $O \in \{1,-1\}$. The probability $P_{\mathbf{k},\mathbf{g}}^{O\to -O}$ depends on the opinion distribution of a focal node's neighbors; the opinion distribution depends implicitly on the opinion of the focal node. However, as a simplification, we assume that the states of the neighbors and the state of the focal node are independent when updating the state of the focal node. This assumption is called "absence of dynamical correlations" in Ref. [GMW12]. Additionally, we only consider the case that both layers have majority opinions; we ignore all other situations. In our simulations, we examined several opinion-update probabilities for when one or both layers do not have a majority opinion. We do not observe meaningful differences between the steady-state behavior of these different choices. Therefore, we claim that ignoring the case of an equal number of neighbors supporting each opinion in a layer has minimal influence on our mean-field expressions. With these simplifications, we define $P_{\mathbf{k},\mathbf{g}}^{\to O}$ as the probability that the focal node adopts opinion O regardless of its current state. The probability $P_{\mathbf{k},\mathbf{g}}^{\to O}$ satisfies $P_{\mathbf{k},\mathbf{g}}^{\to -1} = 1 - P_{\mathbf{k},\mathbf{g}}^{\to 1}$. Let $\bar{q}_{\mathbf{g}} = \sum_{\mathbf{k}} \mathbb{P}(\mathbf{k}) q_{\mathbf{k},\mathbf{g}}$, where $\mathbb{P}(\mathbf{k})$ denotes the degree distribution of the physical nodes. Based on equation (4.1), we have

$$\frac{d}{dt}\bar{q}_{\mathbf{g}} = -\bar{q}_{\mathbf{g}} + \sum_{\mathbf{k}} \mathbb{P}(\mathbf{k}) P_{\mathbf{k},\mathbf{g}}^{\to 1} \,. \tag{4.2}$$

We seek to expand $P_{\mathbf{k},\mathbf{g}}^{\to 1}$. Let $\xi_{k,g}^{(l)}$ denote the probability that the majority opinion of the neighbors is 1 for a focal state node in layer l with degree k and community label g. We assume that the states of the neighbors in the two layers are independent, so that

$$\begin{aligned} P_{\mathbf{k},\mathbf{g}}^{\to 1} &= (1-f_1)\xi_{k_1,g_1}^{(1)}\xi_{k_2,g_2}^{(2)} + f_1(1-\xi_{k_1,g_1}^{(1)})(1-\xi_{k_2,g_2}^{(2)}) \\ &\quad + (1-f_2)\xi_{k_1,g_1}^{(1)}(1-\xi_{k_2,g_2}^{(2)}) + f_2(1-\xi_{k_1,g_1}^{(1)})\xi_{k_2,g_2}^{(2)} \\ &= f_1 + (1-f_2-f_1)\xi_{k_1,g_1}^{(1)} + (f_2-f_1)\xi_{k_2,g_2}^{(2)} \,. \end{aligned} \tag{4.3}$$

The probability $\xi_{k,g}^{(l)}$ is

$$\xi_{k,g}^{(l)} = \sum_{n=\lceil k/2 \rceil}^{k} \left(1 - \frac{1}{2}\delta_{n,k/2}\right) \binom{k}{n} (Q_g^{(l)})^n (1 - Q_g^{(l)})^{k-n}, \tag{4.4}$$

where δ is the Kronecker delta and $Q_g^{(l)}$ denotes the probability that a uniformly randomly chosen neighbor of a state node with community label g in layer l holds opinion 1. To close the system, we write $Q_g^{(l)}$ in terms of $\bar{q}_{\mathbf{g}}$ as follows:

$$\begin{aligned}
Q_1^{(1)} &= (1-\mu_1)\nu\bar{q}_{(1,1)} + (1-\mu_1)(1-\nu)\bar{q}_{(1,2)} + \mu_1(1-\nu)\bar{q}_{(2,1)} + \mu_1\nu\bar{q}_{(2,2)}\,, \\
Q_2^{(1)} &= \mu_1\nu\bar{q}_{(1,1)} + \mu_1(1-\nu)\bar{q}_{(1,2)} + (1-\mu_1)(1-\nu)\bar{q}_{(2,1)} + (1-\mu_1)\nu\bar{q}_{(2,2)}\,, \\
Q_1^{(2)} &= (1-\mu_2)\nu\bar{q}_{(1,1)} + \mu_2(1-\nu)\bar{q}_{(1,2)} + (1-\mu_2)(1-\nu)\bar{q}_{(2,1)} + \mu_2\nu\bar{q}_{(2,2)}\,, \\
Q_2^{(2)} &= \mu_2\nu\bar{q}_{(1,1)} + (1-\mu_2)(1-\nu)\bar{q}_{(1,2)} + \mu_2(1-\nu)\bar{q}_{(2,1)} + (1-\mu_2)\nu\bar{q}_{(2,2)}\,.
\end{aligned} \tag{4.5}$$

Equations (4.2)–(4.5) are a closed system that approximates the time evolution of $\bar{q}_{\mathbf{g}}$.

The binomial distribution in equation (4.4) is expensive to compute for large values of k. Therefore, we approximate it with a normal distribution using the central limit theorem. In our analysis and experiments in the subsequent sections, we use the following approximation:

$$\xi_{k,g}^{(l)} \approx \frac{1}{2} + \frac{1}{2}\mathrm{erf}\left(\sqrt{2k}\left(Q_g^{(l)} - \frac{1}{2}\right)\right), \tag{4.6}$$

where $\mathrm{erf}(z) = \frac{2}{\sqrt{\pi}}\int_0^z e^{-t^2}dt$ is the error function.

4.4 Steady states

By numerically solving the ODE system (4.2, 4.3, 4.5, 4.6), we find that there are three types of steady states; these states depend on the choices of parameters and on the initial conditions. Let $\bar{m}_{(g_1,g_2)} = 2\bar{q}_{(g_1,g_2)} - 1$ denote the mean opinion of community $C_{(g_1,g_2)}$, and let $\bar{m} = 2\bar{q} - 1$ denote the mean opinion of the entire population. One steady-state solution

is $\bar{q}_{(g_1,g_2)} = \frac{1}{2}$ for all g_1 and g_2. In this solution, the two opinions are uniformly randomly distributed in the population and the mean opinion $\bar{m}_{(g_1,g_2)}$ of each community is 0. We call this solution the "fully-mixed steady state". The four communities in the other two types of steady-state solutions have preferences either for the same opinion or for different opinions. Specifically, $\bar{q}_{(g_1,g_2)}$ deviates from $\frac{1}{2}$ and has equal values for all g_1 and g_2 in one case, which corresponds to "consensus steady states". In the other case, $\bar{q}_{(g_1,g_2)} - \frac{1}{2}$ do not all have the same sign; these correspond to "polarized steady states". In this section, we derive expressions for the steady-state solutions and conditions for the linear stability of these solutions using our mean-field approximation (4.2, 4.3, 4.5, 4.6).

4.4.1 The fully-mixed steady state

We start with the fully-mixed steady-state solution. The Jacobian matrix of equation (4.2) at $\bar{q}_{(g_1,g_2)} = \frac{1}{2}$ for all g_1, g_2 is

$$\mathbb{J}_{\text{full}} = \frac{\sqrt{2}}{\sqrt{\pi}}(1 - f_2 - f_1)\langle\sqrt{k}\rangle^{(1)} \times \begin{bmatrix} (1-\mu_1)\nu & (1-\mu_1)(1-\nu) & \mu_1(1-\nu) & \mu_1\nu \\ (1-\mu_1)\nu & (1-\mu_1)(1-\nu) & \mu_1(1-\nu) & \mu_1\nu \\ \mu_1\nu & \mu_1(1-\nu) & (1-1\mu_1)(1-\nu) & (1-\mu_1)\nu \\ \mu_1\nu & \mu_1(1-\nu) & (1-1\mu_1)(1-\nu) & (1-\mu_1)\nu \end{bmatrix}$$
$$+ \frac{\sqrt{2}}{\sqrt{\pi}}(f_2 - f_1)\langle\sqrt{k}\rangle^{(2)} \times \begin{bmatrix} (1-\mu_2)\nu & \mu_2(1-\nu) & (1-\mu_2)(1-\nu) & \mu_2\nu \\ \mu_2\nu & (1-\mu_2)(1-\nu) & \mu_2(1-\nu) & (1-\mu_2)\nu \\ (1-\mu_2)\nu & \mu_2(1-\nu) & (1-\mu_2)(1-\nu) & \mu_2\nu \\ \mu_2\nu & (1-\mu_2)(1-\nu) & \mu_2(1-\nu) & (1-\mu_2)\nu \end{bmatrix} - I\,, \tag{4.7}$$

where $\langle\sqrt{k}\rangle^{(l)}$ denotes the mean of the square root of the degree in layer l. Because $0.5 \geq f_2 > f_1$, the largest eigenvalue of $\mathbb{J}_{\text{full}}$ is

$$\lambda_{\text{full}} = -1 + \frac{\sqrt{2}}{\sqrt{\pi}}(1 - f_2 - f_1)\langle\sqrt{k}\rangle^{(1)} + \frac{\sqrt{2}}{\sqrt{\pi}}(f_2 - f_1)\langle\sqrt{k}\rangle^{(2)} \,. \tag{4.8}$$

Therefore, the fully-mixed steady state $\bar{q}_{(g_1,g_2)} = \frac{1}{2}$ (with g_1, $g_2 \in \{1, 2\}$) is linearly stable if $\lambda_{\text{full}} < 0$. This condition is independent of μ_1, μ_2, and ν. This result is the same as in the majority-vote model on monolayer networks with community structure [HCS15]. Increasing f_1 always decreases λ_{full}; this helps stabilize the fully-mixed solution. By contrast, the effect of f_2 depends on the difference between the edge densities of the two layers. Recall that f_2 measures the tendency for nodes to favor the majority opinion in layer 1 over that in layer 2 when their majority opinions differ. A smaller value of f_2 implies that nodes have a larger preference for layer 1. When layer 1 has fewer (respectively, more) edges, which is equivalent to the condition that layer 1 has a smaller (respectively, larger) value of $\langle k\rangle$, decreasing (respectively, increasing) f_2 helps stabilize the fully-mixed state.

4.4.2 Consensus steady states

We study the situation that each community has the same mean opinion. To do this, we examine steady-state solutions of the system (4.2, 4.3, 4.5, 4.6) of the form

$$\bar{q}_{\mathbf{g}} = \frac{1}{2} + \epsilon \quad \text{for all } \mathbf{g} \tag{4.9}$$

for some $\epsilon \in [-\frac{1}{2}, 0) \cup (0, \frac{1}{2}]$. Consequently, the mean opinions $\bar{m}_{\mathbf{g}} = \bar{m} = 2\epsilon \neq 0$. We set the right-hand sides of equations (4.2) to 0 and insert the ansatz (4.9). The parameter ϵ satisfies

$$\epsilon = \frac{1}{2}(1-f_2-f_1)\left(\sum_{k_1}\mathbb{P}^{(1)}(k_1)\text{erf}(\sqrt{2k_1}\epsilon)\right) + \frac{1}{2}(f_2-f_1)\left(\sum_{k_2}\mathbb{P}^{(2)}(k_2)\text{erf}(\sqrt{2k_2}\epsilon)\right) \,, \tag{4.10}$$

where $\mathbb{P}^{(l)}(k)$ denotes the degree distribution of the state nodes in layer l. The error function is an S-shaped odd function and is bounded by -1 and 1. Therefore, equation (4.10) admits a solution $\epsilon \in [-\frac{1}{2}, 0) \cup (0, \frac{1}{2}]$ if and only if the value on the right-hand side of (4.10) is smaller than $\frac{1}{2}$ at $\epsilon = \frac{1}{2}$ and its derivative at $\epsilon = 0$ is larger than 1. The former condition is always satisfied. The latter condition is equivalent to

$$1 < \frac{\sqrt{2}}{\sqrt{\pi}}(1 - f_2 - f_1)\langle\sqrt{k}\rangle^{(1)} + \frac{\sqrt{2}}{\sqrt{\pi}}(f_2 - f_1)\langle\sqrt{k}\rangle^{(2)}\,, \tag{4.11}$$

which is also the condition for the disordered steady state to be unstable. Suppose that equation (4.10) has a non-zero solution $\epsilon^* \in [-\frac{1}{2}, \frac{1}{2}]$. The solution $\bar{q}_{\mathbf{g}} = \frac{1}{2} + \epsilon^*$ is always linearly stable because the largest eigenvalue of the Jacobian matrix of equation (4.2) at these values of $\bar{q}_{\mathbf{g}}$ equals the derivative of the right-hand side of equation (4.10) minus 1. The derivative is always smaller than 1. Therefore, for a fixed f_2, when f_1 is smaller than a critical value, consensus steady states are linearly stable. Moreover, the mean opinions $\bar{m}_{\mathbf{g}}$ at a consensus steady state and the critical value of f_1 are independent of the values of μ_1, μ_2, and ν.

4.4.3 Polarized steady states

Suppose that the two communities in one layer have different mean opinions at steady states. Because of the symmetry between the two opinions and the symmetry between the two communities, we expect that the steady-state solutions also have a symmetric structure. Suppose that

$$\begin{aligned} \bar{q}_{(1,1)} &= \frac{1}{2} + \epsilon_1\,, \qquad & \bar{q}_{(1,2)} &= \frac{1}{2} + \epsilon_2\,, \\ \bar{q}_{(2,1)} &= \frac{1}{2} - \epsilon_2\,, \qquad & \bar{q}_{(2,2)} &= \frac{1}{2} - \epsilon_1\,. \end{aligned}$$

Inserting this ansatz into the steady state of the system (4.2, 4.3, 4.5, 4.6) yields

$$\begin{aligned}
\epsilon_1 &= \frac{1}{2}(1-f_2-f_1)\left(\sum_{k_1}\mathbb{P}^{(1)}(k_1)\mathrm{erf}(\sqrt{2k_1}y_1)\right)+\frac{1}{2}(f_2-f_1)\left(\sum_{k_2}\mathbb{P}^{(2)}(k_2)\mathrm{erf}(\sqrt{2k_2}y_2)\right)\,,\\
\epsilon_2 &= \frac{1}{2}(1-f_2-f_1)\left(\sum_{k_1}\mathbb{P}^{(1)}(k_1)\mathrm{erf}(\sqrt{2k_1}y_1)\right)-\frac{1}{2}(f_2-f_1)\left(\sum_{k_2}\mathbb{P}^{(2)}(k_2)\mathrm{erf}(\sqrt{2k_2}y_2)\right)\,,
\end{aligned} \tag{4.12}$$

where

$$\begin{aligned}
y_1 &= (1-2\mu_1)\nu\epsilon_1+(1-2\mu_1)(1-\nu)\epsilon_2\,,\\
y_2 &= (1-2\mu_2)\nu\epsilon_1-(1-2\mu_2)(1-\nu)\epsilon_2\,.
\end{aligned} \tag{4.13}$$

One can solve equations (4.12)–(4.13) for ϵ_1 and ϵ_2 using fixed-point iterations and determine the linear stability of polarized steady states by evaluating the largest eigenvalue of the Jacobian matrix. The eigenvalue is

$$\begin{aligned}
\lambda_{\text{polarized}} = -1 &+ \frac{\sqrt{2}}{\sqrt{\pi}}(1-f_2-f_1)\left(\sum_{k_1}\mathbb{P}^{(1)}(k_1)\sqrt{k_1}e^{-(\sqrt{2k_1}y_1)^2}\right)\\
&+ \frac{\sqrt{2}}{\sqrt{\pi}}(f_2-f_1)\left(\sum_{k_2}\mathbb{P}^{(2)}(k_2)\sqrt{k_2}e^{-(\sqrt{2k_2}y_2)^2}\right)\,.
\end{aligned} \tag{4.14}$$

Consider the special case in which we construct the two layers from the same random-network ensemble. Specifically, we take $\mu_1=\mu_2=\mu$ and $\mathbb{P}^{(1)}(k)=\mathbb{P}^{(2)}(k)=\mathbb{P}(k)$. Additionally, we let $f_2=0.5$. Because of the symmetry between the two layers, $\epsilon_2=0$ and

$$\epsilon_1 = \left(\frac{1}{2}-f_1\right)\sum_k \mathbb{P}(k)\mathrm{erf}\left(\sqrt{2k}(1-2\mu)\nu\epsilon_1\right)\,. \tag{4.15}$$

As we discussed in Section 4.4.2, equation (4.15) admits a nontrivial solution if the derivative

of its right-hand side at $\epsilon_1 = 0$ is larger than 1. Equivalently, there is a nontrivial solution if

$$f_1 < \frac{1}{2} - \frac{\sqrt{\pi}}{2\sqrt{2}(1-2\mu)\nu\langle k^{1/2}\rangle}\,. \tag{4.16}$$

Suppose that condition (4.16) is satisfied, We denote the solution to (4.15) by ϵ_1^*. The largest eigenvalue of the Jacobian matrix is $-1 + \frac{2\sqrt{2}}{\sqrt{\pi}}(\frac{1}{2} - f)\sum_k \mathbb{P}(k)\sqrt{k}e^{-(\sqrt{2k}(1-2\mu)\nu\epsilon_1^*)^2}$. Therefore, the steady-state solution is linearly stable if and only if

$$\begin{aligned} \epsilon_1 &= \left(\frac{1}{2} - f_1\right)\sum_k \mathbb{P}(k)\mathrm{erf}\left(\sqrt{2k}(1-2\mu)\nu\epsilon_1\right)\,, \\ 1 &> \frac{2\sqrt{2}}{\sqrt{\pi}}\left(\frac{1}{2} - f_1\right)\sum_k \mathbb{P}(k)\sqrt{k}e^{-\left(\sqrt{2k}(1-2\mu)\nu\epsilon_1\right)^2}\,. \end{aligned} \tag{4.17}$$

In this special case, consensus steady states are linearly stable if and only if $f_1 < \frac{1}{2} - \frac{\sqrt{\pi}}{2\sqrt{2}\langle k^{1/2}\rangle}$, which is larger than the right-hand side of equation (4.16) because $\mu \in (0, 0.5)$ and $\nu \in [0.5, 1]$. Because equation (4.16) is only a necessary condition for polarized steady states to be linearly stable, the stability region of polarized steady states is a subset of the stability region of consensus steady states. This result is consistent with and generalizes previous results for the monolayer majority-vote model [HCS15].

4.5 Numerical experiments

We now compare the results of computational simulations with our analytical results. In all of our simulations, we generate multiplex networks using the network model in Section 4.2.2. We sample the two layers from the same network ensemble. We set the mean degrees to be $\langle k\rangle = 60$ in each layer and let $\mu_1 = \mu_2 = \mu = 0.25$. Consequently, the degree distribution of state nodes in each layer approximately follows a Poisson distribution with mean 60 and $(p_{\text{in}}, p_{\text{out}}) = \left(\frac{2(1-\mu)\langle k\rangle}{N}, \frac{2\mu\langle k\rangle}{N}\right)$. We run each simulation for $200N$ time steps. We consider a steady state to be stable if we observe it in our simulations. In our simulations, when

we assign the initial opinions uniformly at random, the system can reach either consensus steady states or polarized steady states if the system is in the regime in which both steady states are stable. However, because (1) the linear stability region of the consensus steady states contains the linear stability region of polarized steady states in our mean-field model and (2) we are more interested in locating the boundary at which polarized steady states lose stability, we want more simulations to reach polarized steady states. To achieve this, we assign the initial opinions based on the community assignments of nodes. We assign opinion 1 to all physical nodes in community 1 in layer 1 and assign opinion -1 to the remaining physical nodes. By maximizing $|\bar{m}_{(1,1)} - \bar{m}_{(2,2)}|$ and $|\bar{m}_{(1,2)} - \bar{m}_{(2,1)}|$, we expect that the initial state of the system is closer in the state space to a polarized steady state than to a consensus steady state. Consequently, we expect that it is more difficult for stochasticity in our numerical simulations to pull the system towards a consensus steady state. In our simulations, this choice of initial opinions always yields polarized steady states when the parameters are inside the polarized regime and are sufficiently far away from its stability boundary. We initialize the opinions of the nodes based on their community assignments in all subsequent simulations.

For both our simulations and our mean-field approximation, we calculate the overall mean opinion $\bar{m}$ and the single-community mean opinion $\bar{m}_{(1,1)}$ to see which steady state the system reaches. At the fully-mixed steady state, we expect that both $\bar{m}$ and $m_{(1,1)}$ are close to 0. At a consensus steady state, neither $\bar{m}$ or $\bar{m}_{(1,1)}$ is close to 0. At a polarized steady state, we expect that $\bar{m}$ is close to 0 and $\bar{m}_{(1,1)}$ is not. For each set of parameters, we run our model on 10 networks. To calculate the mean opinions in our simulations, we first calculate the mean opinion of each node over the last 30 time steps. We then calculate the mean of these time-averaged opinions in the entire population and in community $C_{(1,1)}$. We take absolute values of these means because there is an equal probability for the system or a community to favor each opinion. Finally, we report the means of these absolute values (the population-scale and the community-scale time-averaged opinions) over the simulations.

When we refer to "mean opinions" from simulations in the rest of this section, we refer to the means that we calculate using this procedure.

4.5.1 Experiment 1

We set $f_2 = 0.5$ so that the nodes treat neighbors in the two layers equally when the majority opinions are different in the two layers. With this choice of f_2, our majority-vote model is the same as the model that was studied in Ref. [KGS18] if one ignores the case that an equal number of neighbors hold each opinion in a layer.

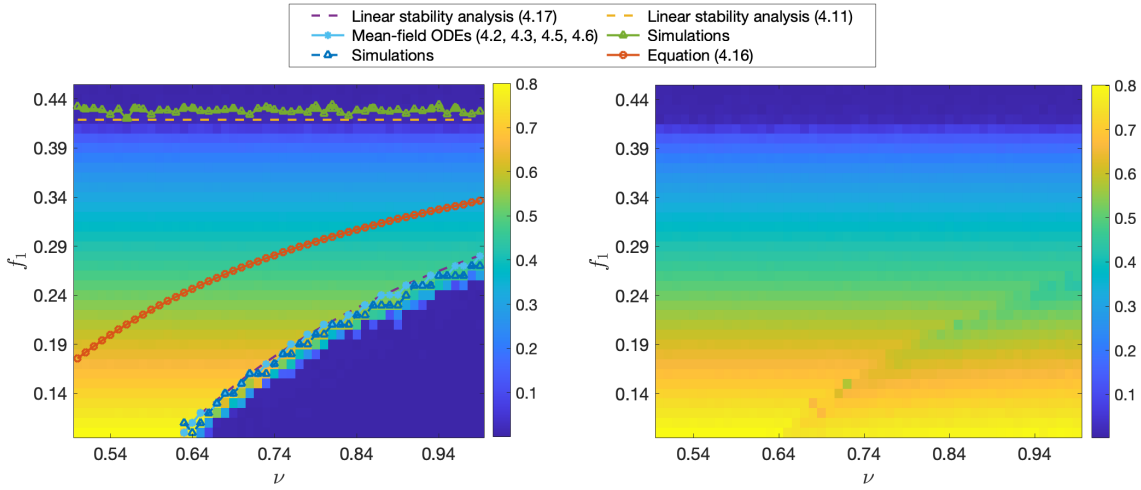

Figure 4.1: Heat maps of (left) the mean opinions of the entire population and (right) the mean opinions of community $C_{(1,1)}$ from means of 10 direct numerical simulations. The horizontal axis is the parameter ν that controls the correlation of community assignments across layers and the vertical axis is the noise parameter f_1. In the left panel, we mark the boundaries of the stability regions of each steady state that we obtain from direct simulations and from our mean-field approximation. We set $f_2 = 0.5$, $N = 15000$, and $\mu = 0.25$.

In Figure 4.1, we compare our simulation results and our mean-field results for different values of f_1 and ν. We set $N = 15000$. For each set of parameters, we sample 10 networks from the SBM and run our model once on each network. We show the results of our simulations as heat maps; the left panel shows the mean opinions of the whole population, and the right panel shows the mean opinions of community $C_{(1,1)}$. The heat maps in both panels

have three regions. In the left panel, the middle region with values far away from 0 separates the bottom-right and the top regions, which have values that are close to 0. In the right panel, the top region has values that are close to 0. The middle and the bottom-right regions both have values that are far away from 0. The colors undergo sharper changes at locations where the two regions meet than inside the regions. The fully-mixed steady state is stable in the top region, and the consensus steady states are stable in the middle region. In the bottom-right region, both the consensus steady states and the polarized steady states are stable. Because of our choice of initial opinion distributions, the system reaches polarized steady states for almost every simulation except when the parameters are close to the boundary of the bottom-right region. Based on our simulations, it seems that the mean opinions undergo a smooth transition between the fully-mixed region and the consensus region but that there is an abrupt transition between the consensus region and the polarized region.

We mark the boundaries of the stability regions in the left panel of Figure 4.1. For the transition between the fully-mixed regime and the consensus regime, we calculate an approximate zero level set of the mean opinions from our simulation results. Because we take absolute values when calculating the mean opinions, the values are larger than 0. We use MATLAB's `contour` function[1] to find the parameter values at which the mean opinion equals 0.01. (See the green curve with triangles.) We plot the linear-stability boundaries using (4.11). (See the yellow dashed curves.) These two curves are close to each other. For the transition between the consensus regime and the polarized regime, we observe a rapid decrease of the mean opinions when we decrease f_1, so we do not try to plot an approximate zero level set. Instead, we determine the values of f_1 that yield the maximum mean opinions for each ν. (See the blue curve with triangles.) From our linear stability condition (4.17), for each pair of f and ν, we solve for ϵ_1 using fixed-point iterations and calculate the value of the largest eigenvalue. We collect the largest eigenvalues and obtain a matrix of eigenvalues. We calculate an approximate zero level set of this matrix using

[1] MATLAB's `contour` function finds isolines of a matrix through interpolation.

the contour function. (See the purple dashed curve.) We obtain a matrix of mean opinions by numerically solving the ODE system (4.2, 4.3, 4.5, 4.6) for each pair of f and ν. The light-blue curve with asterisks indicates the approximate zero level set of this mean-opinion matrix. We set the initial condition to be compatible with the initial opinion distributions in our direct numerical simulations; this entails that $(\bar{q}_{(1,1)}, \bar{q}_{(1,2)}, \bar{q}_{(2,1)}, \bar{q}_{(2,2)}) = (1, 1, 0, 0)$. The three curves are close to each other, but they are not very close to the approximate zero level set of the mean opinions from our simulation results. As the parameters approach the boundary of the stability region of the polarized steady states, it seems that the polarized steady states become less stable and the stochasticity of our numerical simulations makes it easier for the system to reach a consensus steady state. We also expect that the stochasticity has more influence as N decreases and that the gap between the three curves and the actual zero level set decreases as N increases. To examine this, we run the same simulations for $N = 5000$ and plot our results in Figure 4.2. The gap widens, as expected. Finally, we plot the condition (4.16) (see the red curve with circles) to verify that condition (4.16) is a necessary but not sufficient condition for polarized steady states to be linearly stable.

Overall, we observe that the phase-transition patterns for $f_2 = 0.5$ are qualitatively the same as what was obtained for the monolayer majority-vote model in Ref. [HCS15]. For a fixed ν, the system undergoes two transitions as f_1 decreases. The smaller critical value is independent of ν (as we see in our mean-field model) and the larger critical value increases with ν.

4.5.2 Experiment 2

In this experiment, we explore the influence of the layer-preference parameter f_2. In Figures 4.3 and 4.4, we show heat maps of the mean opinions for a range of f_1 and ν values when $f_2 = 0.32$ and $f_2 = 0.26$, respectively. These two figures show two typical heat maps. In the left panels of both figures, the dark-blue regions indicate regimes in which both consensus steady states and polarized steady states are stable; in the yellow regions, only consensus

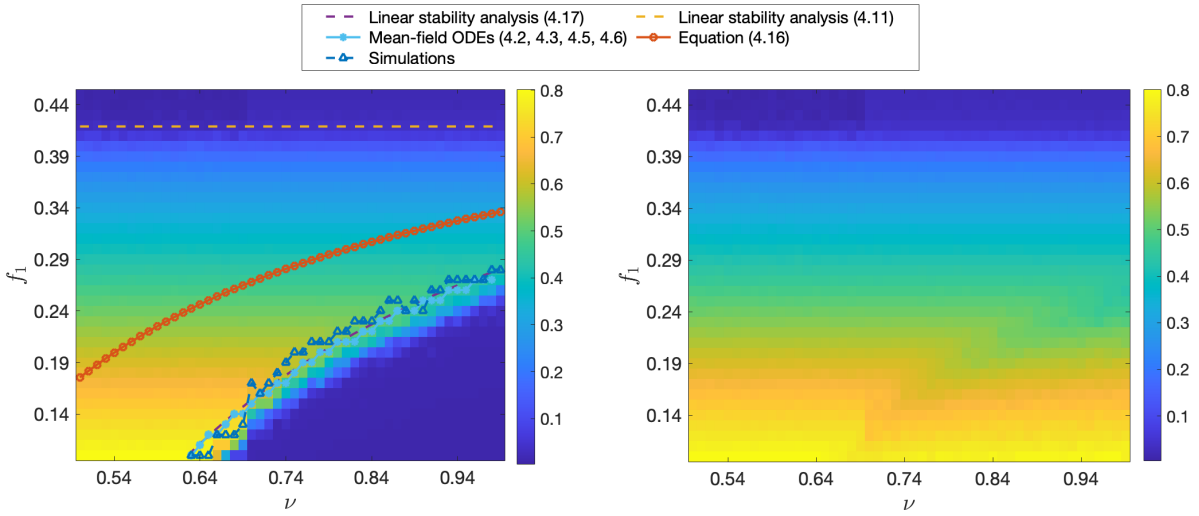

Figure 4.2: Heat maps of (left) the mean opinions of the entire population and (right) the mean opinions of community $C_{(1,1)}$ from means of 10 direct numerical simulations. In the left panel, we mark the boundaries of the stability regions of each steady state that we obtain from direct simulations and from our mean-field approximation. We set $f_2 = 0.5$, $N = 5000$, and $\mu = 0.25$.

steady states are stable. At locations where the two regions meet, both figures have jagged boundaries, which one can smoothen by running simulations with more finely-grained values of f_1 and ν. Figure 4.3 has a similar pattern as Figure 4.1. In Figure 4.4, however, we see that the polarized steady states are stable in a much larger region than in Figures 4.1 and 4.3. This indicates that it is easier for different communities to favor different opinions when the nodes have a stronger preference for opinions in one layer than for those in the other. Additionally, when ν is small, polarized steady states are stable for large values of f_1 but not for small values of f_1. We do not know the reason that small values of f_1 appear to destabilize polarized steady states.

4.5.3 Experiment 3

In this experiment, we fix ν and run our model for different values of f_1 and f_2 with $0.5 \geq f_2 > f_1 > 0$. We show heat maps of the mean opinions in Figure 4.5–4.7 for different values

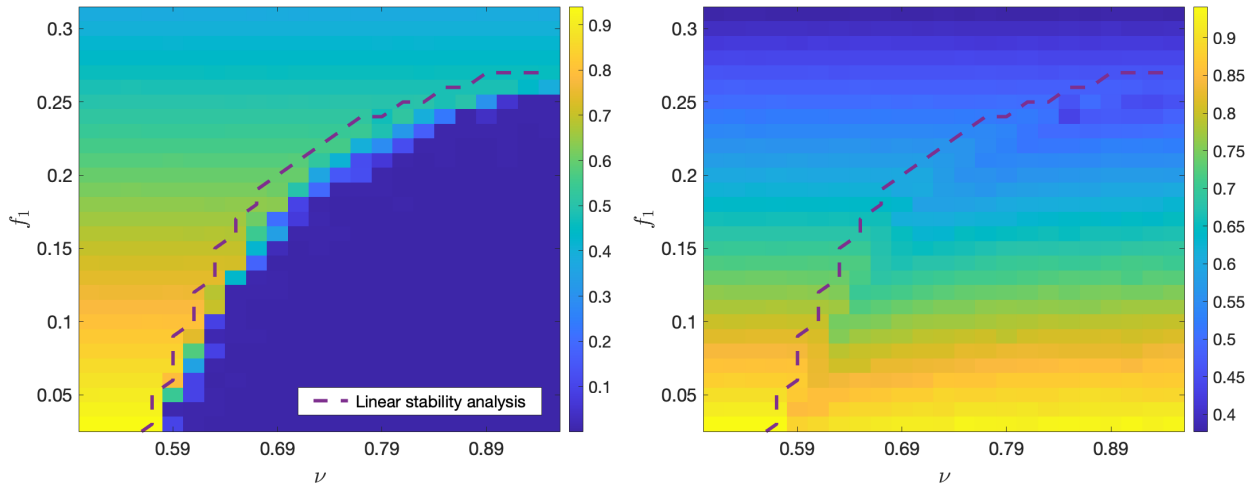

Figure 4.3: Heat maps of (left) the mean opinions of the entire population and (right) the mean opinions of community $C_{(1,1)}$ from means of 10 direct numerical simulations. In both panels, we mark the boundary of the linear stability region of polarized steady states; we obtain it by setting $\lambda_{\text{polarized}} = 0$ in equation (4.14). We set $f_2 = 0.32$, $N = 10000$, and $\mu = 0.25$.

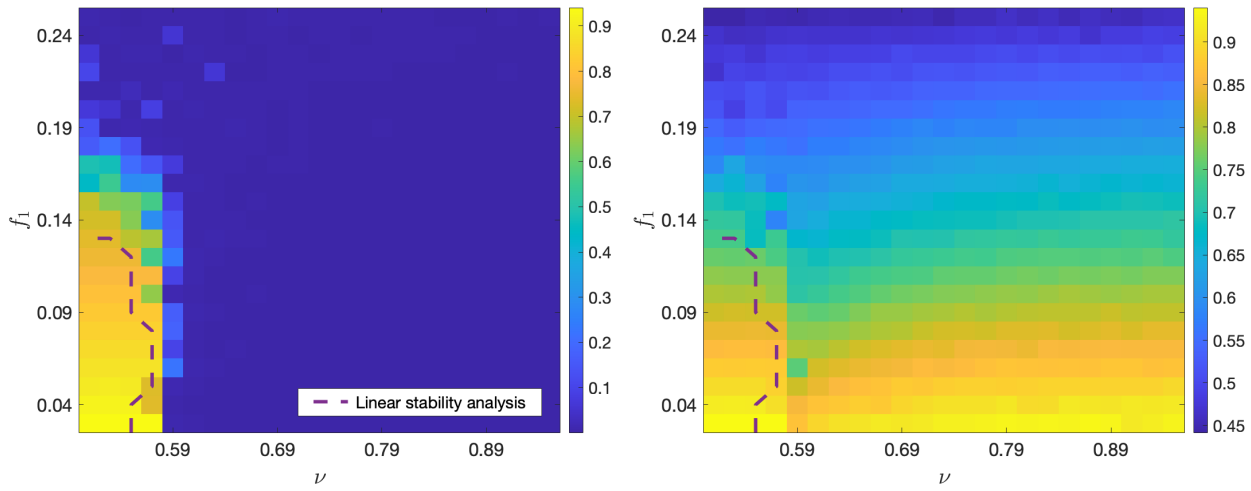

Figure 4.4: Heat maps of (left) the mean opinions of the entire population and (right) the mean opinions of community $C_{(1,1)}$ from means of 10 direct numerical simulations. In both panels, we mark the boundary of the linear stability region of polarized steady states; we obtain it by setting $\lambda_{\text{polarized}} = 0$ in equation (4.14). We set $f_2 = 0.26$, $N = 10000$, and $\mu = 0.25$.

of ν. The dark-blue regions in the lower part of the triangles are regions where polarized steady states are stable. From our linear stability analysis, we obtain the boundaries of linear stability regions of polarized steady states by setting $\lambda_{\text{polarized}} = 0$ in equation (4.14). We mark the boundaries with dashed curves. The area of this region increases as ν increases, so it is easier for different communities to develop preferences for different opinions when the communities in the two layers are more strongly correlated with each other. We also observe some other interesting features. Let f_1^* denote the maximum value of f_1 for which there exists some f_2 such that polarized steady states are stable. When $f_1 > f_1^*$, polarized steady states are not stable for any value of f_2. The value of f_1^* is the same in Figures 4.5–4.7. Let f_2^* denote the value of f_2 such that (f_1^*, f_2^*) is on the boundary of the stability region. When ν is small (see Figure 4.5), there exists $f_2 < f_2^*$ such that polarized steady states are stable for some f_1. For larger values of ν (see Figures 4.6 and 4.7), f_2^* is the minimum value of f_2 such that polarized steady states are stable.

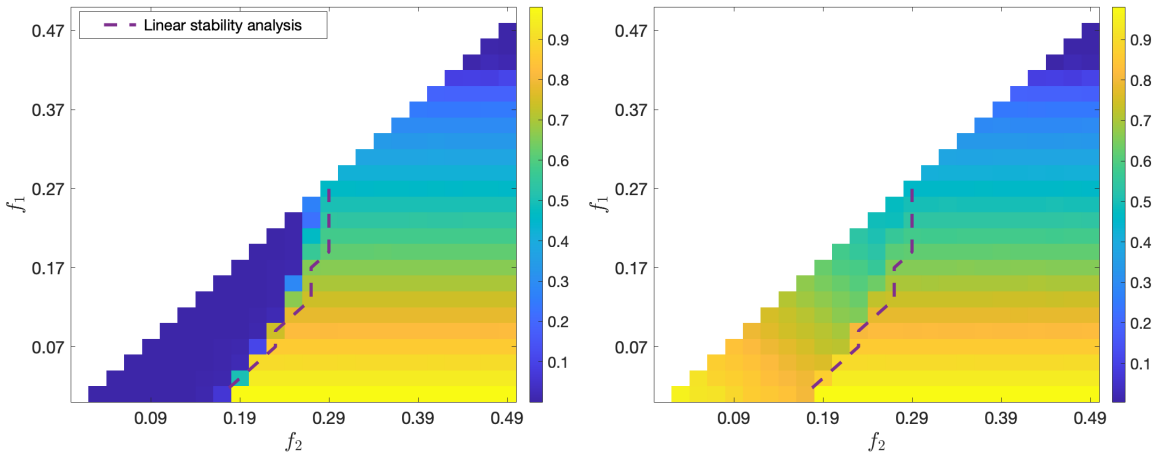

Figure 4.5: Heat maps of (left) the mean opinions of the entire population and (right) the mean opinions of community $C_{(1,1)}$ from means of 10 direct numerical simulations. In both panels, we mark the boundary of the linear stability region of polarized steady states; we obtain it by setting $\lambda_{\text{polarized}} = 0$ in equation (4.14). We set $\nu = 0.5$, $N = 10000$, and $\mu = 0.25$.

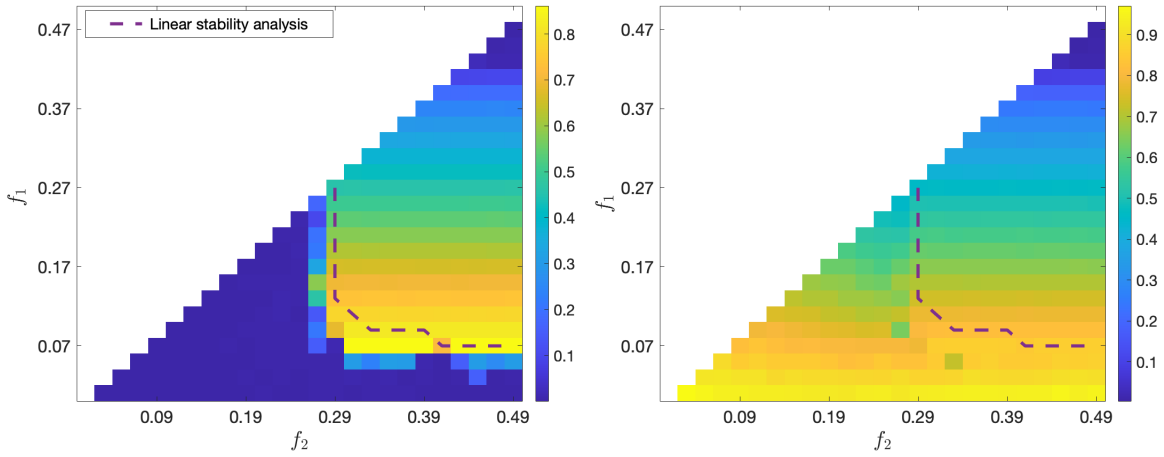

Figure 4.6: Heat maps of (left) the mean opinions of the entire population and (right) the mean opinions of community $C_{(1,1)}$ from means of 10 direct numerical simulations. In both panels, we mark the boundary of the linear stability region of polarized steady states; we obtain it by setting $\lambda_{\text{polarized}} = 0$ in equation (4.14). We set $\nu = 0.6$, $N = 10000$, and $\mu = 0.25$.

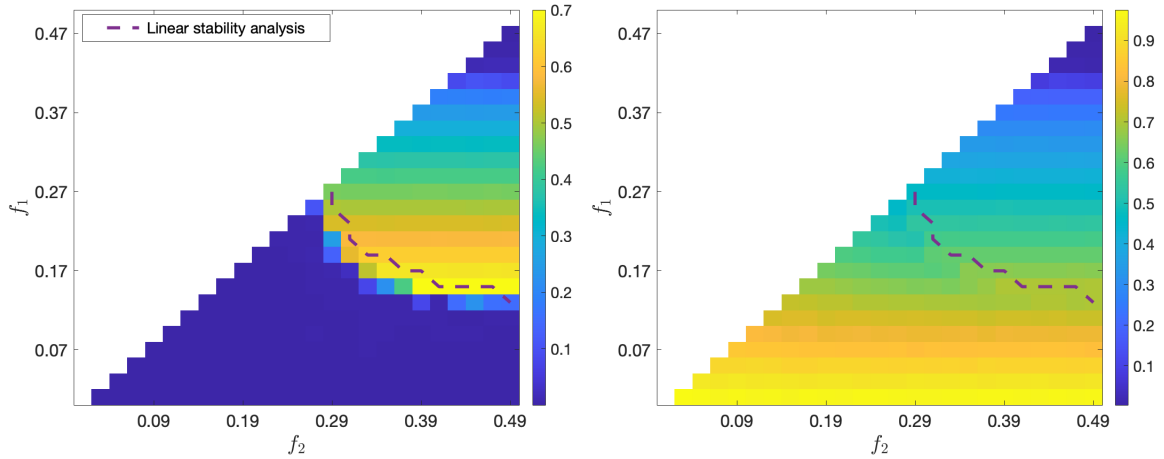

Figure 4.7: Heat maps of (left) the mean opinions of the entire population and (right) the mean opinions of community $C_{(1,1)}$ from means of 10 direct numerical simulations. In both panels, we mark the boundary of the linear stability region of polarized steady states; we obtain it by setting $\lambda_{\text{polarized}} = 0$ in equation (4.14). We set $\nu = 0.7$, $N = 10000$, and $\mu = 0.25$.

4.6 Conclusions and discussions

We proposed a multiplex majority-vote model in which each layer represents one relationship and each physical node holds one opinion. Our model considers situations in which different relationships have different propensities to influence an individual's opinion. This feature cannot exist in monolayer opinion models and (to the best of our knowledge) was neglected in the multiplex majority-vote models that were studied in previous works. We examined the steady-state opinion distributions of our majority-vote model on networks with community structure. We observed the same three regimes as those that were observed in majority-vote models on monolayer networks with community structure [HCS15]. Additionally, we showed using simulations and mean-field calculations that heterogeneous influence abilities of different layers can qualitatively affect the regions in which polarized steady states are stable.

There are many ways to generalize our model. First, one can consider more complicated network structures. One can examine more realistic community structures (e.g., by considering degree-corrected SBMs or overlapping communities), and one can also study the influence of interlayer degree correlations and interlayer edge overlaps on opinion spread. Second, one can consider more general opinion-update rules. For example, when the two layers have the same majority opinion, the probability that a node flips its opinion when the common majority opinion is the same as its opinion and the probability that it flips when the common majority opinion is different from its opinion do not have to sum to 1. Third, in our model, each node has the same propensity of conforming to one of the two layers when the two layers have different majority opinions (i.e., they have the same value of f_2). A natural extension is to consider a model in which the nodes have heterogeneous propensities. This is typically relevant when the different layers represent different online social platforms; different people do prefer different social platforms in real life. Moreover, because individuals who belong to the same communities often share common traits, it seems sensible to study

situations in which individuals' preferred relationships are correlated with their community memberships .

CHAPTER 5

Modeling Illegal Logging in Brazil

This chapter is adapted from an original paper [CPP21] that I co-authored with Bohan Chen, Christian Parkinson, Andrea L. Bertozzi, Tara Lyn Slough and Johannes Urpelainen. Bohan implemented the main algorithm, and I performed experiments and analyzed results.

5.1 Introduction

Deforestation, and illegal logging in particular, has caused some of the most damaging effects to the world's forests [Reb13, LV15]. There have been a variety of attempts to model and quantify deforestation from ecologists, political scientists, applied mathematicians, and others. For example, Pfaff studied the correlation between certain parameters and deforestation in tropical regions such as Brazil [Pfa99] . The three dominant categories of parameters were identified by Pfaff and other authors [LAS02, AGR15] as accessibility, population, and climate. One effort to control deforestation in Brazil while exploiting timber in a sustainable way is through allowing legal concessions for industrial timber harvest in public forests [ASM15]. Under such concessions, companies that operated in Brazil fell an average of only one tree per acre instead of clear-cutting to allow tree regrowth [TF20]. However, as was reported by Trevisani et al. [TF20], legal timber companies pulled out of the concession because uncontrolled loggers invaded the companies' land, illegally toppling and stealing trees. They also mentioned that the Brazilian government's failure to detect and punish these criminals led to even more rampant organized crime and more severe deforestation.

It is an essential and urgent task to determine effective tactics to combat illegal logging. Efficient and effective deployment of law enforcement to threatened areas is essential to deter these crimes. Such deployment has been modeled in a continuum setting [Alb10, AFJ19, CV20]. However, effective deterrence can lead to spatial "spillovers" as loggers move away from areas with heavy monitoring. Assessing loggers' responses to policies is important when designing an effective system that minimizes deforestation of forested areas. In this chapter, we build a game-theoretic model to infer interactions between uncontrolled loggers and law-enforcement agents.

5.1.1 Deforestation in the state of Roraima

We use the PRODES (Programa Despoluição de Bacias Hidrográficas, or "Basin Restoration Program") data set [IN], which is the official data set that the Brazilian government uses for annual statistics that are related to deforestation. PRODES includes a mixture of computer analysis and human expert analysis to delineate deforestation regions in the Brazilian Amazon. The minimum patch size of such region is 6.25 hectares (ha). We focus on the state of Roraima, which is the northernmost state in Brazil. We extract annual deforestation-event data and tree-coverage data from PRODES. We also use the transportation system map (including highways and waterways) from OpenStreetMap [Ope17]. OpenStreeMap labels highways based on their importance. In this chapter, we call the highways with labels motorway, trunk, primary, secondary, and tertiary as "major highways" and the highways with labels road, track, and unclassified as "secondary highways". We ignore the highways with other labels. In Figure 5.1(a), we plot the deforestation events from 2001 to 2015 and the transportation system of Roraima. We see that many of the deforestation events occur near highways and rivers. We show the tree-coverage data for 2015 in Figure 5.1(b), where yellow indicates land covered by trees and blue indicates cleared land. There are fifteen municipalities in the state of Roraima. In our model, we assume that loggers originate from and return to these fifteen municipalities.

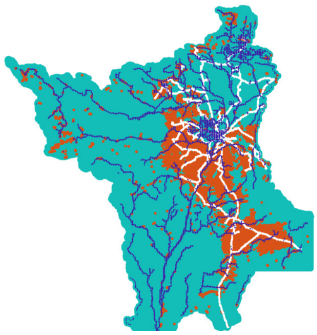

(a) Deforestation events on top of the transportation system

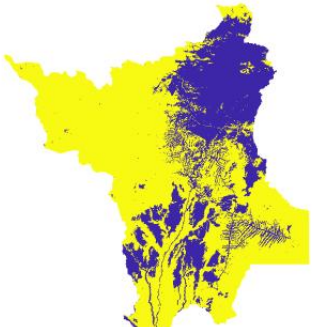

(b) The indicator function of tree coverage

Figure 5.1: An overview of the data from PRODES [IN]. Panel (a) shows the deforestation events between 2001 and 2015 in Roraima on top of the transportation system. We use the highway and waterway map from OpenStreetMap [Ope17]. Dark blue indicates rivers, white indicates major highways, and red dots indicate deforestation events. Panel (b) shows tree-coverage data for 2015; yellow represents regions that are covered by trees and blue represents uncovered regions.

5.1.2 Previous work

Albers [Alb10] proposed the first game-theoretic model of deforestation that is continuous in space. They modeled deforestation events in a circular area with radially symmetric benefit and patrol functions. Criminals enter from the boundary of the area and want to maximize their profit

$$P(d) = (1 - \Phi(d))B(d) - C(d)\,,$$

where d is the shortest distance between the extraction point to the boundary, B is the benefit to an attacker, C is the travel cost, Φ is the cumulative patrol function (so $(1 - \Phi)$ indicates the probability of avoiding capture).

Johnson et al. [JFT12] examined optimal patrol strategies in the framework of Albers' model [Alb10]. Kamra et al. [KGF18] extended Albers' model by removing the assumption that the distribution of trees is radially symmetric. They considered a game between law enforcement and extractors and applied machine-learning techniques to find optimal or near-optimal patrol strategies. All of these works considered a circular region and assumed that

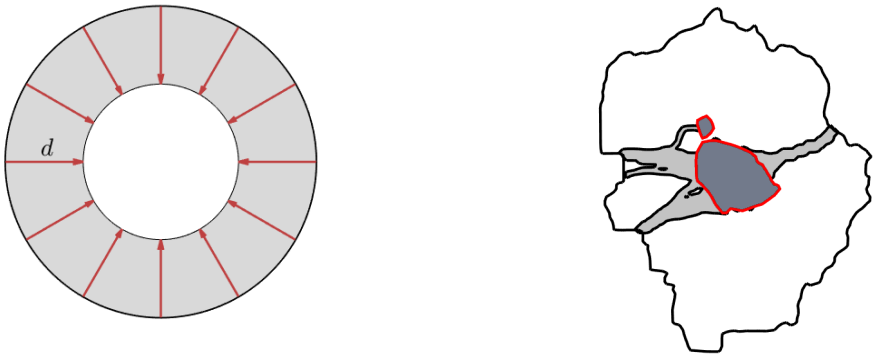

(a) Model of Albers [Alb10] in radially symmetric areas

(b) Model of Arnold et al. [AFJ19] applied to Yosemite National Park

Figure 5.2: Illustration of previous work. (a) Albers' [Alb10] model assumes a radially symmetric and radially symmetric functions so that extractors only move along the radius. (b) Arnold et al. [AFJ19] generalized the model to terrains with arbitrary shapes and applied their generalized model to the Yosemite national park. In both panels, the white area is pristine and the grey area is affected by criminals.

extractors come from the boundary of the region and move toward the center. The radial symmetry of the region and the functions is a major restriction.

Arnold et al. [AFJ19] generalized Albers' model [Alb10] to any closed, simple region in $\mathbb{R}^2$. The primary tool that they employed to study their model is the level-set method [OS88]. In their model, the cost represents the effort of logging at any point in the protected area. They evaluated the effort by calculating the optimal travel time, where the travel speed is allowed to depend on terrain data. They modeled the impact of patrol by including capture probability in the form of a heuristic modified speed that decreases as the product of patrol intensity and benefit increases. The model has not been evaluated against real-world data, but it was recently modified and improved by Cartee and Vladimirsky [CV20]. They constructed two models that are based on whether or not authorities use ground patrol (where confiscation takes place as perpetrators are detected) or aerial patrol (with which illegal goods are not confiscated until perpetrators exit the protected area).

Models for illegal extraction with discretized domains have been developed by Fang et al. [YFT14, FNP17] and Kar et al. [KFD15, KFG17]. Fang et al. [FNP17] developed the PAWS (Protection Assistant for Wildlife Security) algorithm and described the protected region as nodes that are connected by edges, which are natural pathways such as rivers or roads. They deployed their models in Queen Elizabeth National Park (QENP), Uganda and a conservation area in Malaysia. Kar et al. [KFG17] used machine-learning techniques to predict attacks from extractors and conducted a one-month field test in QENP. Both methods showed potential to improve the effectiveness of law enforcement agencies. One advantage of these methods, which are discrete, is that they can readily incorporate realistic features such as detailed terrain information, different types of environmental crime (including animal poaching), and different types of patrol teams [MTK16]. However they have the disadvantage that they do not track the actual movement of the environmental criminals. Additionally, it can be difficult to interpret the results of these models because of the "black box" nature of parameter-estimation methods.

5.1.3 Our contribution

Our model builds on the works by Arnold et al. [AFJ19] and Cartee et al. [CV20]. We use optimal control theory to model and solve a path-planning problem that is faced by uncontrolled loggers as they balance benefit, travel cost, and capture risk. We assume that authorities deploy remote patrols, similarly to model A in [CV20]; therefore there is a delay in confiscation of illegal goods. We introduce several improvements to make our model more realistic than previous works. We consider non-instantaneous logging activities and positive capture risk while logging on site so that loggers can choose optimal logging time to maximize their profit. We also incorporate load-dependent travel speed when loggers return from a forest with illegal goods. We work directly with real-world data from Brazil to calibrate our model. We simulate and conduct a side-by-side comparison of the inferred outcomes of several geographically targeted and data-driven patrol strategies.

The remainder of the chapter is organized as follows. In Section 5.2, we discuss our model formulation. We discuss a multiobjective approach that transforms our optimization problem into solving ekonal equations, which we solve numerically with a fast-sweeping method. In Section 5.3, we discuss the setup and results of our numerical experiments. We summarize our conclusions in Section 5.4.

5.2 Illegal-logging model

Our model, which is based on the work of Albers [Alb10] and Arnold et al. [AFJ19], examines the decision-making process of loggers. Our model allows an arbitrary domain as in Ref. [AFJ19], but it balances travel time and capture risk in a more judicious manner than in Ref. [AFJ19] by appealing to optimal control theory. We also account for logging time, which was ignored by previous models but makes a big difference to loggers' profit (see Section 5.3). In the remaining part of the present section, we construct our model and then pose an optimal control problem as a static Hamilton–Jacobi equation. We solve this equation using a fast-sweeping method [BD99, ZOM00, TCO03, Zha05, Par21].

5.2.1 Model construction

Given an arbitrary domain $\Omega \subseteq \mathbb{R}^2$, our goal is to construct an expected profit function $P(x) : \Omega \to \mathbb{R}$ from the perspective of loggers. We adopt the basic idea from Albers [Alb10], who used $P = (1 - \Phi)\mathcal{B} - \mathcal{C}$. The function $\mathcal{B}$ is a benefit function that describes the value of the timber if loggers are not captured during a trip. The function $\mathcal{C}$ represents the cost and is measured by the travel cost of both entering and leaving the forest. The term $1 - \Phi$ describes the probability of not being captured, which depends on patrollers' detection ability and loggers' trajectories. We present details of these three components in the following paragraphs. We follow the Stackelberg game model [Von10] and assume that loggers have perfect information about patrol.

The benefit function $\mathcal{B}$ depends on the value and amount of timber that perpetrators log. We assume that each location x in the domain Ω has a fixed amount of timber, but with a different total value $B(x)$ that depends on the category and quality of timber. Departing from previous models, for which extraction happens instantaneously, we introduce the notion of a logging time $t_{\log}$, which is comparable to the travel time. We assume that loggers have a constant production rate $1/T$, where T is a global constant that represents the time to clear all of the trees in one location. If one ignores the existence of patrollers, the benetift function is $\mathcal{B}(t) = \frac{t_{\log}}{T} B(x)$. We always assume that $t_{\log} \leq T$ and that loggers only extract from one spot x in one trip.

We assume that loggers can be detected when they are logging or when they are returning with illegal goods. We define the capture intensity using the function $\psi : \Omega \to \mathbb{R}$, which we assume to be known to loggers and dependent on patrol resources and strategies. In particular, we assume that it satisfies a budget constraint

$$\int_{\Omega} \psi(x)(1 + \mu d(x))^2 \, dx \leq E \,, \tag{5.1}$$

where E represents the budget, $d(x)$ is the Euclidean distance from location x to major highways, and μ is an adjustable weight parameter. The term $(1+\mu d(x))^2$ models a scenario in which it is more expensive to patrol deeper into a forest. We try several capture intensity functions in the experiments in Section 5.3. Following the derivation in [CV20], we take the probability of not being captured while logging at x for time $t_{\log}$ to be $e^{-\psi(x) t_{\log}}$. Longer logging time entails a larger benefit, but it also entails a larger risk of being detected. We assume that the loggers are detectable only when they have timber in their possession. The probability of not being captured when a logger returns via a path $X(s)$ is $e^{-\int_0^\tau \psi(X(s)) ds}$, where τ is the travel time. If they are detected, they lose all of the benefit without extra penalty. (See the discussion at the end of this subsection.) The expected benefit of logging

at location x for time $t_{\log}$ and returning via path $X(s)$ is

$$B(x)\frac{t_{\log}}{T}e^{-\psi(x)t_{\log}}e^{-\int_0^{\tau}\psi(X(s))\,ds}\,. \tag{5.2}$$

The cost, represented by the travel time, is straightforward to calculate if one has a path and the loggers' travel speed. We assume that loggers embark from and return to one of the fifteen municipalities in Roraima. We use X_{in} and X_{out} to represent the paths to and from the logging location, respectively. We allow loggers to return to any municipality — not necessarily the one from which they embarked from. In our model, we first define the travel speed $v : \Omega \to \mathbb{R}^2$ towards the forest based on the region's transportation system. Loggers travel fastest when they are on major highways and are slower when they are on water or secondary highways. When loggers are not on highways or waterways, we scale their speed according to terrain slope, in the same ways as in Ref. [AFJ19]. When they return, we assume that their speed is slower because of loaded cars or boats. We set the return speed of loggers to be $v_{\text{out}} = v(x)/(1 + c(t_{\log}/T)^{\gamma})$, where $t_{\log}/T$ measures the amount of timber that loggers carry back. The parameters c and γ model the influence of carrying timber on the speed of motion. A larger travel cost may be another reason that loggers decide to spend less than the maximum logging time.

Based on our previous assumptions, the profit of logging at position x for time $t_{\log}$ and following paths X_{in} and X_{out} is

$$\begin{aligned} P(x, t_{\log}, X_{\text{in}}, X_{\text{out}}) = B(x)\frac{t_{\log}}{T}e^{-\psi(x)t_{\log}}e^{-\int_0^{\tau_{\text{out}}}\psi(X_{\text{out}}(s))\,ds} \\ - \int_0^{\tau_{\text{out}}} \alpha(X_{\text{out}}(s))\,ds - \int_0^{\tau_{\text{in}}} \alpha(X_{\text{in}}(s))\,ds\,, \end{aligned} \tag{5.3}$$

where τ_{in} and τ_{out} are travel times and α is a dimensional function that converts time to monetary value. As in [CV20], α may be constant or may depend on the regions. This can model loggers' preferences for certain areas or represent differences in the unit cost of travel

time for different modes of travel. For example, perhaps the unit time cost of traveling on waterways is smaller than that of traveling on highways. We have made various assumptions and choices to obtain a concrete profit function. It is difficult to verify their validity and it seems useful to study variations of our model with other assumptions.

Rational loggers try to solve the optimization problem

$$P_{\text{opt}}(x) = \max_{t_{\log}, X_{\text{in}}, X_{\text{out}}} P(x, t_{\log}, X_{\text{in}}, X_{\text{out}}) \tag{5.4}$$

and may fall trees from locations with positive profit. The optimal paths going in and out of a forest can be different because of patrols. In reality, a mixture of different patrol methods are deployed, including ground patrol (which use boats and motor vehicles), and remote patrol, (which use satellite, helicopters, planes and drones). As was pointed out in [CV20], ground patrols lead to immediate confiscation, so it seems more reasonable for loggers to switch to the minimum-time path after they are detected. In this chapter, we always assume that the government deploys remote patrols. Because loggers are unaware of being detected, they choose optimal return paths that balance capture risk and travel time.

5.2.2 Multiobjective approach and eikonal equations

We adapt the multiobjective optimal-control approach of Cartee and Vladimirsky [CV20] to our model and describe its use in solving the optimization problem (5.4). We consider a trajectory $X(s)$ that follows the dynamics

$$\begin{aligned} &\dot{X}(t) = \mathfrak{a}(t) v(X(t)) \,, \ t \in [0, S] \,, \\ &X(0) = x \,, \\ &X(S) \in \mathbb{X}_0 \,, \end{aligned} \tag{5.5}$$

where $\mathbb{X}_0$ denotes the set of possible destinations (the fifteen municipalities). The map $\mathfrak{a}$ is the control plan; it is an element of the set of valid control functions

$$\mathcal{A} = \{\mathfrak{a} : [0, S] \to \mathbb{R}^2 \mid \mathfrak{a} \text{ measurable}, \ |\mathfrak{a}(t)| = 1, \text{ for all } t \in [0, S]\}.$$

Define $J_1(x, \mathfrak{a}, v) = \int_0^\tau \psi(X(s))\, ds$ and $J_2(x, \mathfrak{a}, v) = \int_0^\tau \alpha(X(s))\, ds$. According to (5.3), the profit is

$$P(x, t_{\log}, X_{\text{in}}, X_{\text{out}}) = B(x)\frac{t_{\log}}{T} e^{-\psi(x)t_{\log}} e^{-J_1(x,\mathfrak{a},v_{\text{out}})} - J_2(x, \mathfrak{a}, v_{\text{out}}) - R(x), \tag{5.6}$$

where $R(x)$ is the minimum cost of traveling from $\mathbb{X}_0$ to x. In fact, because our speed is isotropic, $R(x)$ is the unique viscosity solution [CL83, BC08] of the eikonal equation

$$\begin{aligned} v(x)|\nabla R(x)| &= \alpha(x), \quad x \in \Omega \setminus \mathbb{X}_0, \\ R(x) &= 0, \quad x \in \mathbb{X}_0. \end{aligned} \tag{5.7}$$

Recall that in our model, loggers do not need to worry about patrols and they travel with speed $v(x)$ along a path toward a forest. Along a return path, the loggers' speed decreases if they carry timber. The amount of timber that they carry is proportional to their logging time. In our model, we set $v_{\text{out}} = v/(1 + c(t_{\log}/T)^\gamma)$. Expanding v_{out} in equation (5.6) yields

$$\begin{aligned} P(x, t_{\log}, X_{\text{in}}, X_{\text{out}}) = B(x)\frac{t_{\log}}{T} e^{-\psi(x)t_{\log}} e^{-J_1(x,\mathfrak{a},v)(1+c(t_{\log}/T)^\gamma)} \\ - J_2(x, \mathfrak{a}, v)(1 + c(t_{\log}/T)^\gamma) - R(x). \end{aligned} \tag{5.8}$$

We determine the optimum profit value using a multiobjective control formulation as in [CV20]. For any $\lambda \in [0, 1]$, let $K^\lambda(x) = \lambda\psi(x) + (1 - \lambda)\alpha(x)$. Then the λ-optimal value function $u^\lambda(x)$

$$u^\lambda(x) = \inf_{\mathfrak{a}\in\mathcal{A}} \{\lambda J_1(x, \mathfrak{a}, v) + (1 - \lambda)J_2(x, \mathfrak{a}, v)\} \tag{5.9}$$

is the unique viscosity solution of the eikonal equation

$$\begin{aligned} v(x)|\nabla u^\lambda(x)| &= K^\lambda(x)\,, \quad x \in \Omega \setminus \mathbb{X}_0\,, \\ u^\lambda(x) &= 0\,, \quad x \in \mathbb{X}_0\,. \end{aligned} \tag{5.10}$$

While we do not expect u^λ to be smooth, under mild conditions on v and K, it is Lipschitz continuous and hence differentiable almost everywhere. Therefore, the optimal controls that achieve $u^\lambda(x)$, which we call λ-optimal controls, are uniquely determined for almost every starting point $x \in \Omega \setminus \mathbb{X}_0$. We denote the set of λ-optimal controls corresponding to $u^\lambda(x)$ as

$$\mathcal{A}_x^\lambda = \arg\min_{\mathfrak{a}\in\mathcal{A}} \left\{\lambda J_1(x,\mathfrak{a},v) + (1-\lambda)J_2(x,\mathfrak{a},v)\right\}\,.$$

The value functions that correspond to λ-optimal controls are defined by

$$\begin{aligned} u_1^\lambda(x) &= \inf_{\mathfrak{a}\in\mathcal{A}_x^\lambda} \left\{J_1(x,\mathfrak{a},v)\right\}, \\ u_2^\lambda(x) &= \inf_{\mathfrak{a}\in\mathcal{A}_x^\lambda} \left\{J_2(x,\mathfrak{a},v)\right\}. \end{aligned} \tag{5.11}$$

Given u^λ, we obtain u_1^λ and u_2^λ by solving

$$\begin{aligned} \nabla u^\lambda(x)\nabla u_1^\lambda(x) &= \frac{\psi(x)K^\lambda(x)}{v^2(x)}\,, \quad x \in \Omega \setminus \mathbb{X}_0\,, \\ \nabla u^\lambda(x)\nabla u_2^\lambda(x) &= \frac{\alpha(x)K^\lambda(x)}{v^2(x)}\,, \quad x \in \Omega \setminus \mathbb{X}_0\,, \end{aligned} \tag{5.12}$$

with boundary conditions $u_1(x) = u_2(x) = 0$, for $x \in \mathbb{X}_0$ [CV20, MS03].

The optimal profit is

$$
\begin{aligned}
P_{\text{opt}}(x) &= \max_{t_{\log},\, X_{\text{in}},\, X_{\text{out}}} P(x, t_{\log}, X_{\text{in}}, X_{\text{out}}) \\
&= \max_{t_{\log}\in[0,T]} \left\{ \sup_{\mathfrak{a}\in\mathcal{A}} \left[B(x)\frac{t_{\log}}{T} e^{-\psi(x)t_{\log}} e^{-J_1(x,\mathfrak{a},v)\left(1+c\left(\frac{t_{\log}}{T}\right)^{\gamma}\right)} \right.\right. \\
&\qquad \left.\left. -J_2(x,\mathfrak{a},v)\left(1+c\left(\frac{t_{\log}}{T}\right)^{\gamma}\right)\right]\right\} - R(x) \\
&= \max_{t_{\log}\in[0,T]} \left\{ \max_{\lambda\in[0,1]} \left[B(x)\frac{t_{\log}}{T} e^{-\psi(x)t_{\log}} e^{-u_1^{\lambda}(x)\left(1+c\left(\frac{t_{\log}}{T}\right)^{\gamma}\right)} \right.\right. \\
&\qquad \left.\left. -u_2^{\lambda}(x)\left(1+c\left(\frac{t_{\log}}{T}\right)^{\gamma}\right)\right]\right\} - R(x) \\
&= \max_{\lambda\in[0,1]} \left\{ \max_{t_{\log}\in[0,T]} \left[B(x)\frac{t_{\log}}{T} e^{-\psi(x)t_{\log}} e^{-u_1^{\lambda}(x)\left(1+c\left(\frac{t_{\log}}{T}\right)^{\gamma}\right)} \right.\right. \\
&\qquad \left.\left. -u_2^{\lambda}(x)\left(1+c\left(\frac{t_{\log}}{T}\right)^{\gamma}\right)\right]\right\} - R(x)\,.
\end{aligned}
\tag{5.13}
$$

The expression

$$
B(x)\frac{t_{\log}}{T} e^{-\psi(x)t_{\log}} e^{-u_1^{\lambda}(x)\left(1+c\left(\frac{t_{\log}}{T}\right)^{\gamma}\right)} - u_2^{\lambda}(x)\left(1+c\left(\frac{t_{\log}}{T}\right)^{\gamma}\right) \tag{5.14}
$$

is a function of $t_{\log}$. It is not easy to find an explicit value of the location where the maximum is obtained. In practice, we discretize $[0,T]\times[0,1]$ into finitely many points (t_i, λ_j) and choose the one that yields the largest profit.

We conclude the discussion of our model with two remarks regarding implementation.

Remark 1: Choice of $\mathbb{X}_0$. In our model, we need to solve the eikonal equation (5.7) for the minimum travel time, where we take $\mathbb{X}_0$ to be the set of municipalities from which the loggers depart. We also need to solve (5.10) for the λ-optimal value function u^{λ}, where we take $\mathbb{X}_0$ to be the set of municipalities to which loggers transport timber. As we mentioned briefly in Section 5.2.1, we do not require loggers to return to the same municipality from which they start. From the patrol perspective, it is not be clear which municipality the loggers will choose. Accordingly, we let $\mathbb{X}_0$ be the set of all fifteen municipalities in both

(5.7) and (5.10). The resulting maximum profit for loggers reflects their freedom to choose their starting and terminal municipalities. If loggers are required to return to their starting point, one can perform 15 calculations that each take $\mathbb{X}_0$ to be a singleton corresponding to one municipality in both equation (5.7) and (5.10). In all of our simulations, we allow loggers to return to any municipality, which always gives a profit that is at least as large as that from insisting that they return to their starting municipality. One can view this situation as a worst-case situation.

Remark 2: Optimal paths. We find optimal paths from $x \in \Omega$ to the set $\mathbb{X}_0$ by following the negative gradient directions of the value functions. More specifically, to find a minimum-cost path from x to $\mathbb{X}_0$ in the absence of patrols (i.e., an optimal path towards the forest), we integrate $\dot{\mathbf{x}} = -v(\mathbf{x})\frac{\nabla R(\mathbf{x})}{|\nabla R(\mathbf{x})|}$. To find an optimal path when loggers carry timber and go outwards (i.e., an optimal return path), we integrate $\dot{\mathbf{x}} = -v(\mathbf{x})\frac{\nabla u^{\lambda}(\mathbf{x})}{|\nabla u^{\lambda}(\mathbf{x})|}$, where λ is an optimal value of the extraction point x.

In our model, optimal logging times can be different at different locations. However, an optimal path is the same regardless of the logging time because the logging time and the amount of timber carried influence the speed uniformly. Consequently, a path is traversed more slowly for a longer logging time, but the spatial location of that path is the same.

One of the basic assumptions of our model is that travel speed is isotropic, meaning that it depends only on position and not on the direction of motion. Therefore, one can determine optimal paths between two points regardless of which is the starting point and which is the ending point. If we instead use an anisotropic speed — for example, if the downstream and upstream velocities of a river are different — this is no longer true. We would then need to compute entering and leaving paths separately, which would require additional partial differential equations (PDEs) similar to (5.7) and (5.10) but formulated with a reversed orientation.

5.2.3 Numerical methods

We need to solve two types of PDE in our model: standard eikonal equations (5.7), (5.10) and auxiliary PDEs (5.12). Because the region Ω (the state of Roraima) has an irregular shape, we use a uniform Cartesian grid to discretize a rectangular region in $\mathbb{R}^2$ that contains Ω. As mentioned in Section 5.2.2, we choose $\mathbb{X}_0$ to be the set of all 15 municipalities in the state of Roraima. This applies to all three equations (5.7), (5.10), and (5.12). To mark the boundary of Ω, we set the travel speed to 0 outside Ω; this makes it impossible for paths to leave the region.

To numerically solve the equations, one can apply standard numerical methods for static Hamilton–Jacobi equations [FF16]. Two of the most popular methods are fast-marching and fast-sweeping schemes. The basic idea of fast-marching methods is to follow characteristic flow and update values at grid nodes monotonically based on the values at neighboring nodes [Tsi95, Set99, SV00, SV03]. With a proper choice of the order of node updates, fast-marching methods can approximate the value function at N grid points with a computational cost of $O(N \log N)$. By contrast, the philosophy of fast-sweeping methods is to account for all possible directions of characteristic flow. Fast-sweeping methods sweep through grid nodes in alternating directions and update values at nodes in a Gauss–Seidel manner [BD99, ZOM00, TCO03, Zha05, Par21]. Each sweep captures the correct characteristic flow for some subset of the nodes. This process is iterated until convergence.

We use the basic fast-sweeping method of Ref. [Zha05]. While the fast-marching method is more efficient, the standard fast-sweeping scheme is sufficient for our purposes and is very easy to implement. If efficiency is a concern and one prefers fast-sweeping methods, one can parallelize the computation as in Ref. [Zha07], though we did not do this. There also exist other fast methods to solve eikonal equations; one example is the method in Ref. [CV12], which uses a hybrid fast-marching and fast-sweeping approach.

5.3 Implementation and results

In this section, we apply the optimization solver (see Section 5.2.2) to our model. We start with a detailed description of the benefit function, the speed function, and the evaluation measures in Section 5.3.1. We then discuss our numerical results in Section 5.3.2.

5.3.1 Experimental setup

High-fidelity inference of the benefit function requires detailed knowledge of Brazilian forest. We construct the benefit function based on the PRODES data set [IN]. Deforestation events within 50 kilometers of the major highways are dense and clustered. We manually checked the street views of many of these locations through Google Map and found that they were used for agricultural purposes. Therefore, we assume that deforestation for agricultural land clearance takes place within 50 kilometers of the major highways and treat all other deforestation events as the result of logging. We mark events with red circles in Figure 5.3(a). We also assume that regions with a high event frequency have a large benefit. We use the same technique as in kernel density estimation [Par62]. We construct a density function by assigning a 2-D Gaussian kernel to each event. From the PRODES data, we also construct an indicator function of tree coverage within the region (see Figure 5.3(b)). We then write the logging benefit function as a linear combination of the density function and the indicator function (see Figure 5.3(c)). Our approach gives some idea of the true benefit but it is not fully accurate, because we do not incorporate features like distance to municipalities and patrols. The simpler benefit function allows us to focus on exploring loggers' behavior under the influence of other factors. The inverse problem of recovering the benefit function based on the deforestation event data, travel distance, and capture risk if of interest by itself. Moreover, as we show in Figure 5.3(a), many logging events are in the periphery of the state of Roraima, providing further evidence that these regions have sufficient benefit to be worthy of long-distance travel. In practice, local governments may be able to design a more realistic

benefit function by incorporating more granular data that involves types of trees and other vegetation in specific areas.

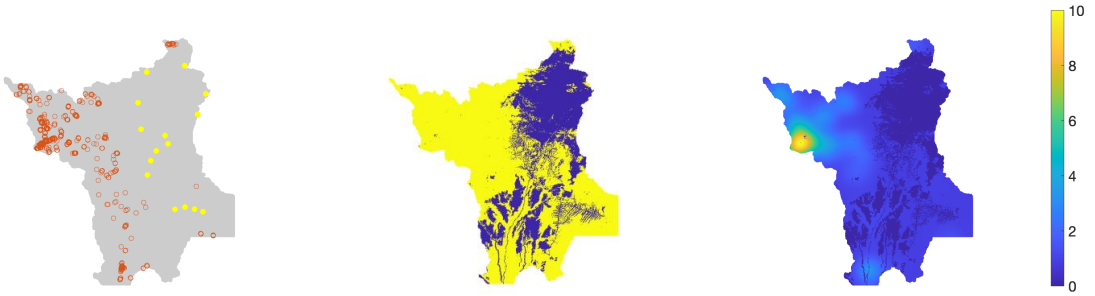

(a) (b) (c)

Figure 5.3: We show (a) logging events from 2001 to 2015 and the 15 municipalities, which we mark with red circles and yellow dots, respectively, (b) the indicator function of tree coverage (yellow) from 2015 PRODES data, and (c) the constructed benefit function. We assume that deforestation events that are at least 50 kilometers away from the major highways are logging events. We discretize the region into a 806×622 grid. We construct the benefit function in panel (c) by combining a density function with the indicator function in panel (b). We normalize the benefit function so that the maximum benefit is 10. We construct the density function by convolving the event count in panel (a) with a 2-D Gaussian kernel of size 17×17 with a standard deviation of 20.

Because our logging model is sensitive to the transportation system, we design a speed field (see Figure 5.4) to capture the movement of loggers in a region. Using the highway and waterway map from OpenStreetMap [Ope17], we assign velocities of 1, 0.7, and 0.4 to major highways, secondary highways, and waterways, respectively. This reflects the assumption that loggers use trucks and cargo ships to transport timber. Outside these regions, we use a speed model that is based on the local slope of the terrain. Specifically, we use elevation data from the Shuttle Radar Topography Mission [FRC07] and set the slope $S(x, y) = |\nabla \mathcal{E}(x, y)|$, where $\mathcal{E}(x, y)$ is the elevation of the region. The speed is 0.2 multiplied by a function of the local slope; see Arnold et al. [AFJ19], who based their speed function on that of Irmischer and Clarke [IC18]. In reality, the speed on waterways may be anisotropic, in contrast to the isotropic assumption in our model. One can generalize our model to incorporate this

more realistic scenario and derive anisotropic Hamilton–Jacobi equations that are similar to equations (5.7) and (5.10).

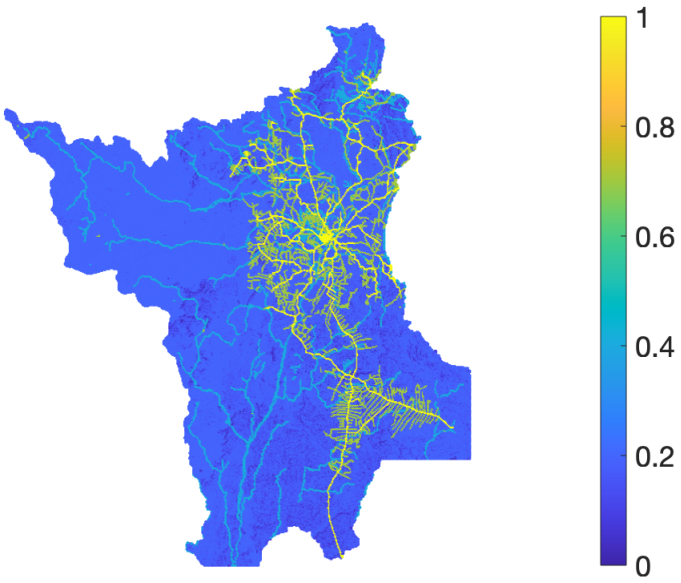

Figure 5.4: Speed field in the state of Roraima. The speed on major highways, secondary highways, and waterways is 1, 0.7, and 0.4, respectively. The speed in off-highway and off-water areas depends on the change of elevation.

Many governments, including the Brazilian government, endeavor to combat deforestation by designating geographic areas as protected areas or priority areas for monitoring and enforcement. However, identifying where to target protection presents challenges for policymakers. We evaluate the efficiency with which targeted patrol strategies can reduce deforestation using three measures:

1. Pristine area ratio PA: We designate the regions with non-positive profit as pristine areas. The ratio of the area of pristine region over the area of the state is PA $= \frac{\int_\Omega \mathbf{1}_{\{P(x)\le 0\}} dx}{\int_\Omega 1 dx}$.

2. Pristine benefit ratio PB: This measure calculates the ratio of the benefit in a pristine

area to the total benefit as PB $= \frac{\int_\Omega B(x)\mathbf{1}_{\{P(x)\le 0\}}dx}{\int_\Omega B(x)dx}$.

3. Weighted profit WP: We interpret the positive part of the profit as the inclination for loggers to choose the logging location. We define WP as the expected profit of loggers using the formula WP $= \frac{\int_\Omega P_+(x)^2 dx}{\int_\Omega P_+(x)dx}$, where $P_+(x) = P(x)\mathbf{1}_{\{P(x)\ge 0\}}$ is the non-negative profit.

We run our model on a 600×600 grid. To search for optimal $\lambda \in [0,1]$ and $t_{\log} \in [0,T]$, we discretize both $[0,1]$ and $[0,T]$ into 101 equally spaced values. The choices of the following parameter values are somewhat arbitrary because we do not have access to empirical data. We expect that the distance to major highways has a moderate influence on patrol cost, so $\mu \times d$ should be roughly at the same order of magnitude as 1. In our experiments, we set $\mu = \frac{2}{5\max_{x\in\Omega} d(x)} \approx 7.33 \times 10^7$. We let the maximal logging time to be $T = 2000000$ so that it has a similar scale as the travel time. We expect that the unit time cost of traveling on waterways to be smaller than on waterways, so we set $\alpha = \mu$ on the highways and $\alpha = 0.7\mu$ otherwise.

5.3.2 Results

We run our model with different patrol budgets and patrol strategies. We also explore the influence of logging time and decreased speed when traveling with goods.

5.3.2.1 Example 1: No patrol

We first suppose that there is no patrol. Recall that the the speed when the loggers return is $v(x)/(1 + c(t_{\log}/T)^\gamma)$ to account for the influence of carrying timber. When there is no patrol (i.e., $\psi(x) = 0$), the optimal paths are the same when traveling to and from the forest. Additionally, when the amount of timber has no influence (i.e., $c = 0$), the loggers always use the maximum logging time T. These statements are generally not true when patrol is

present or $c \neq 0$. We show the resulting non-negative profit P_+ in Figure 5.5(a). We then test $c = 0.5$, $\gamma = 1$ and $c = 1$, $\gamma = 1.5$. As we show in Figure 5.5, a larger c entails a larger reduction of the travel speed and thus leads to a smaller profit. In all of the subsequent experiments, we fix $c = 0.5$ and $\gamma = 1$.

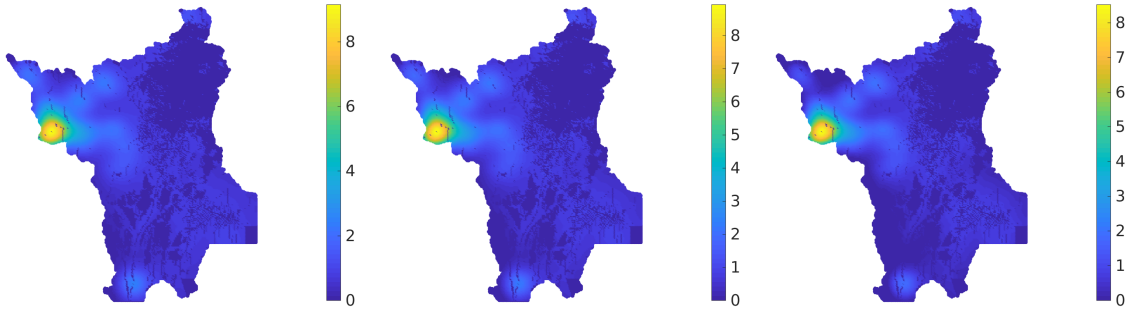

(a) $c = 0$ (b) $c = 0.5, \gamma = 1$ (c) $c = 1.5, \gamma = 1$

Figure 5.5: Expected non-negative profit P_+ when there is no control. The speed when the loggers return depends on the amount of timber and is defined to be $v(x)/(1 + c(t_{\log}/T)^\gamma)$. The weighted profit WP is (a) 2.4091, (b) 2.3499, and (c) 2.2622.

5.3.2.2 Example 2: Comparison of different budgets

Recall that we imposed a budget constraint for patrols in (5.1). We assume that a patrol uses all available resources and impose equality in (5.1) for all of our simulations. In this example, we set

$$\psi(x) = \frac{E}{(1 + \mu d(x))^5 \int_\Omega (1 + \mu d(x))^3 \, dx} \,. \tag{5.15}$$

Recall that $d(x)$ is the Euclidean distance to major highways; the above patrol function puts more patrol effort on regions that are closer to major highways. We plot the capture intensity in Figure 5.9(c); we discuss this intensity further in Section 5.3.2.4. We set E to be 0.001, 0.003, and 0.005 and we plot the resulting non-negative profit in Figure 5.6. As expected, a higher budget yields a lower profit. In all of our subsequent experiments, we fix $E = 0.003$.

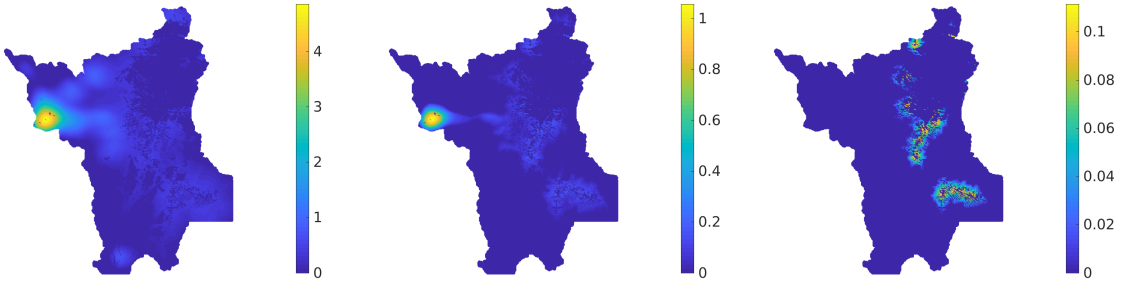

(a) $E = 0.001$ (b) $E = 0.003$ (c) $E = 0.005$

Figure 5.6: Expected non-negative profit P_+ with different budgets E while fixing the other parameters.

5.3.2.3 Example 3: Influence of patrol on optimal logging time

We use the same experimental setup as in example 2, and we fix $E = 0.003$. Recall that we discretize the logging time interval $[0, T]$ into 101 equally spaced values and search for the best logging time at those values. We plot the optimal logging times in Figure 5.7(a) as a proportion of the maximum logging time T used. Because we assume that loggers do not choose locations with zero benefit, we set the optimal logging time at those locations to be 0 in all of our figures of optimal time. We sample four points in this region that achieve optimal logging time when logging for 50%, 60%, 70%, and 80% of T. We mark these points with white dots in Figure 5.7(a). In figure 5.7(b), we show the profit as a function of logging time at each point; the optimal logging times are different for each point. When $c = 0$ (i.e., when carrying timber does not influence travel speed), the optimal time depends only on the capture intensity and is equal to $\min\{1/\psi(x), T\}$. When c is non-zero, the solution of optimal logging time is more complicated because benefit and travel time also play a role.

5.3.2.4 Example 4: Comparison of different patrol strategies

The enforcement strategy in Brazil in the time period 2003–2012 involved a combination of satellite and ground patrols. They successfully reduced deforestation with these strategies. Patrols were active in areas with significant deforestation. These areas are "priority"

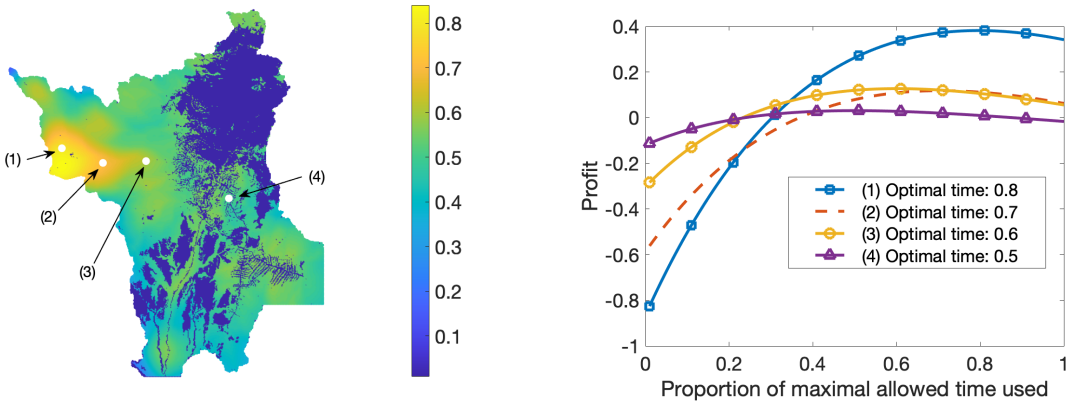

(a) Optimal logging time

(b) Profit versus logging time

Figure 5.7: (a) Optimal logging time. We show the proportion of the maximum time T used on regions with positive benefit. We set the proportion to be 0 on regions with 0 benefit. White points mark locations where the optimal logging times are (1) 80%, (2) 70%, (3) 60%, and (4) 50% of T. (b) Profit as a function of logging time at each of the sampled point from panel (a).

municipalities. Patrols were also sent where the satellite system revealed suspiciously high deforestation [Jac16]. These spatially targeting patrols follow sensible strategies. But we are interested in studying if more sophisticated strategies can improve patrolling efficiency. In this example, we compare the patrolling efficiency of different capture intensity functions $\psi(x)$. Each patrol strategy has a budget $E = 0.003$. We plot the corresponding capture intensity function, non-negative profit P_+, and optimal logging time for each experiment and summarize the values of these quantities in Table 5.1.

We first consider a patrol function that is based only on the distance to major highways by setting

$$\psi(x) = \frac{E}{(1 + \mu d(x))^r \int_\Omega (1 + \mu d(x))^{2-r}\, dx}\,, \tag{5.16}$$

where we choose r from the values 1, 5, and 15. We focus on regions that are close to highways because logging and patrol costs are low in these regions. A larger value of r means that the patrol is more concentrated near the highways, and a smaller value of r entails a patrol that is distributed more uniformly. In Figures 5.8–5.10, we show the corresponding capture

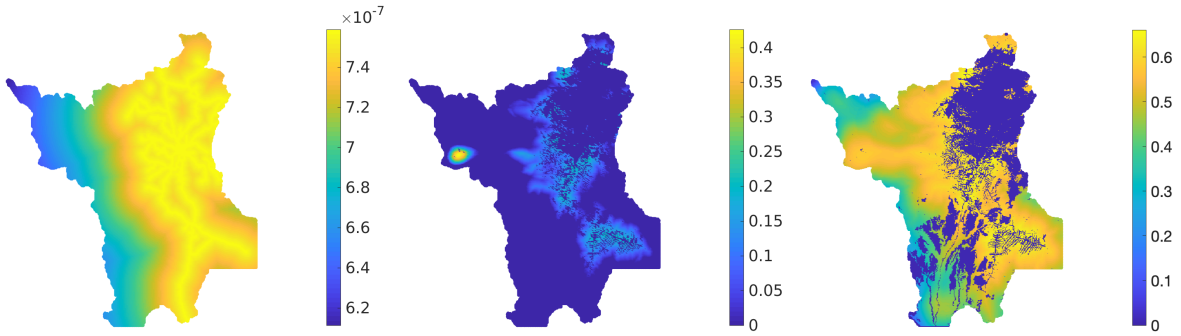

(a) Capture intensity (b) Profit P_+ (c) Optimal logging time

Figure 5.8: (a) Capture intensity is based on distance only, with $r = 1$ in equation (5.16). (b) Expected non-negative profit P_+ for the entire region. (c) Optimal logging time on regions with positive benefit.

intensities, non-negative profits P_+ and, optimal logging times. When $r = 1$, the optimal logging times are distributed more uniformly than for larger values of r. In high-benefit regions (these regions are away from major highways), the optimal logging time and the profit increase markedly with increasing r because loggers are less likely to be captured away from major highways. All three profit plots in Figures 5.8–5.10 have the pattern that high-benefit regions are also high-profit regions. This suggests that we should take the benefit function into consideration when designing patrol strategies.

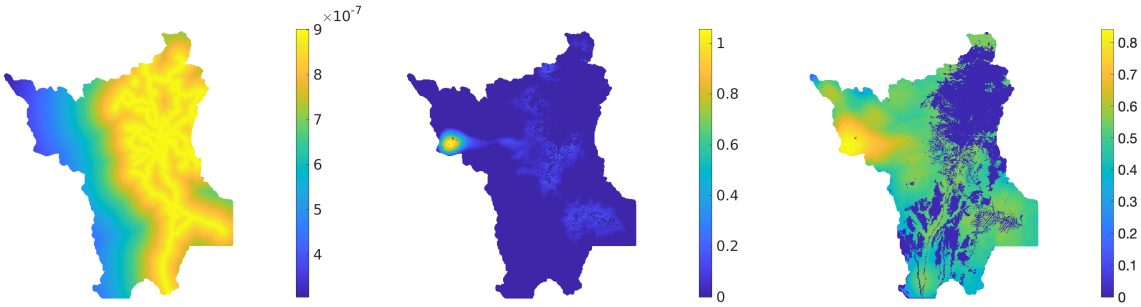

(a) Capture intensity (b) Profit P_+ (c) Optimal logging time

Figure 5.9: (a) Capture intensity is based on distance only, with $r = 5$ in equation (5.16). (b) Expected non-negative profit P_+ for the entire region. (c) Optimal logging time on regions with positive benefit.

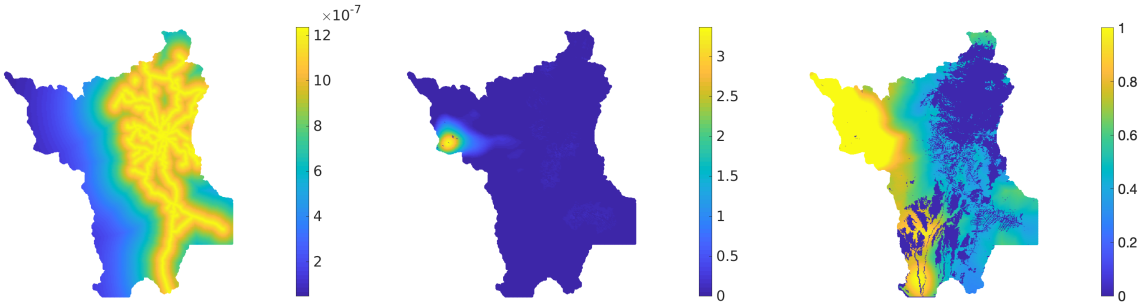

(a) Capture intensity (b) Profit P_+ (c) Optimal logging time

Figure 5.10: (a) Capture intensity is based on distance only, with $r = 15$ in equation (5.16). (b) Expected non-negative profit P_+ for the entire region. (c) Optimal logging time on regions with positive benefit.

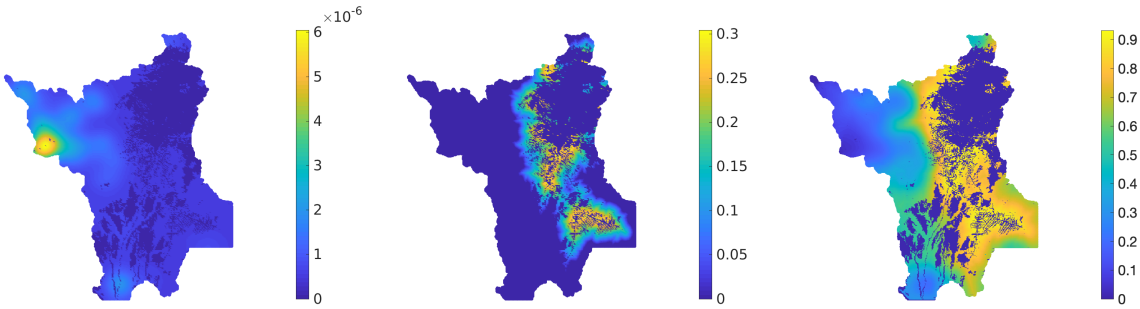

(a) Capture intensity (b) Profit P_+ (c) Optimal logging time

Figure 5.11: (a) Capture intensity is based on benefit only, with $w = 1$ in equation (5.17). (b) Expected non-negative profit P_+ for the entire region. (c) Optimal logging time on regions with positive benefit.

We now set

$$\psi(x) = \frac{B(x)^w E}{\int_\Omega (1 + \mu d(x))^2 B(x)^w \, dx}, \tag{5.17}$$

where we choose w to be 1, 0.5, or 0.2 to target the high-benefit regions. Similar to the previous example, a larger value of w indicates a more concentrated patrol. We show the results in Figures 5.11–5.13. The intense patrol in high-profit regions makes those regions less vulnerable. Additionally, profitable regions now cluster around highways because both the initial benefit and the travel cost are relatively low near highways .

Our experiments thus far in Section 5.3.2.4 inform us that we need to balance benefit

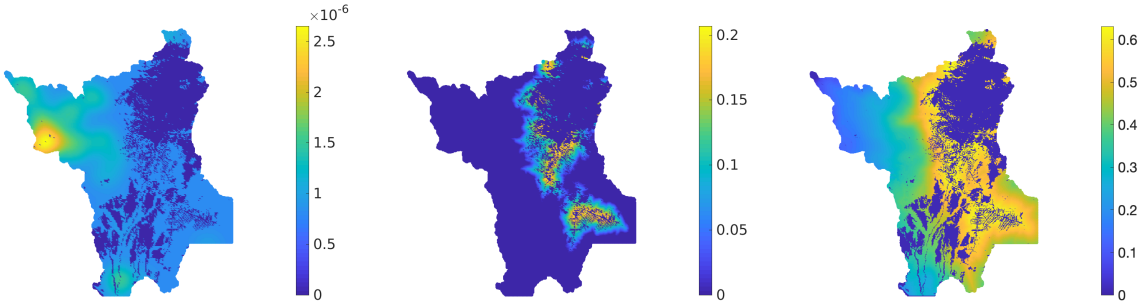

(a) Capture intensity (b) Profit P_+ (c) Optimal logging time

Figure 5.12: (a) Capture intensity is based on benefit only, with $w = 0.5$ in equation (5.17). (b) Expected non-negative profit P_+ for the entire region. (c) Optimal logging time on regions with positive benefit.

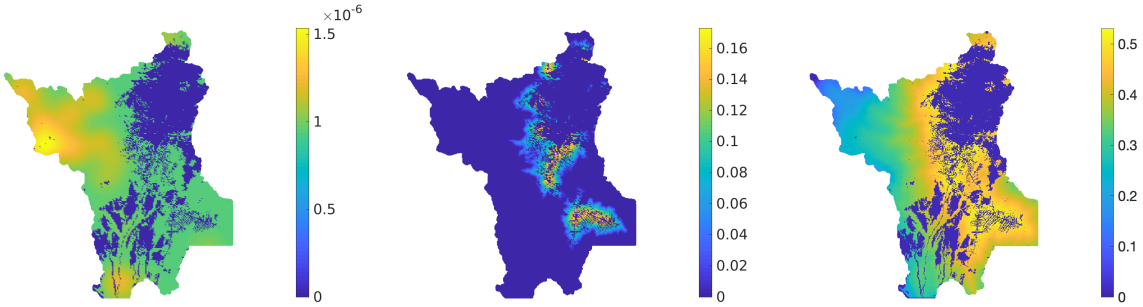

(a) Capture intensity (b) Profit P_+ (c) Optimal logging time

Figure 5.13: (a) Capture intensity is based on benefit only, with $w = 0.2$ in equation (5.17). (b) Expected non-negative profit P_+ for the entire region. (c) Optimal logging time on regions with positive benefit.

and distance when designing a patrol strategy. We set the patrol function to be

$$\psi(x) = \frac{B(x)^w E}{(1 + \mu d(x))^r \int_\Omega (1 + \mu d(x))^{2-r} B(x)^w \, dx} \, . \tag{5.18}$$

We test this patrol function with $w = 0.2$ and $r = 1, 5, 15$. We plot the results in Figures 5.14–5.16. The statistics in Table 5.1 confirm that forests are better protected when patrol strategies take both distance and benefit into account. (Compare (7)–(9) to (1)–(6) in Table 5.1.) Compare the patrol results based on distance only (results (1)–(3)) to the results based on strategy (5.18) (results (7)–(9)) in Table 5.1. It is clear that the "optimal" attention that

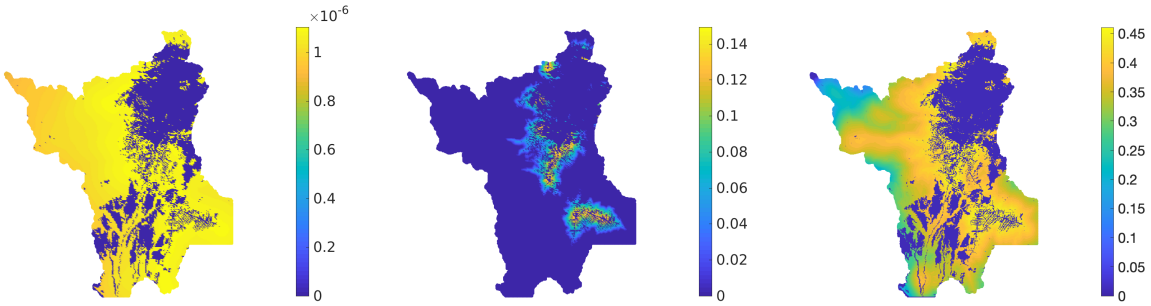

(a) Capture intensity (b) Profit P_+ (c) Optimal logging time

Figure 5.14: (a) Capture intensity is based on benefit and distance, with $w = 0.2$ and $r = 1$ in equation (5.18). (b) Expected non-negative profit P_+ for the entire region. (c) Optimal logging time on regions with positive benefit.

we should give to small-distance regions, as indicated by the value of r, can depend on w (i.e., the attention that is given to high-benefit regions). When we ignore the benefit, the weighted profit (WP) and the protected benefit (PB) measures indicate that smaller r (for which the patrol is more uniform) is better. However, when we take benefit into consideration and let $w = 0.2$, our computations suggest that a moderately large patrol concentration along highways is more appropriate than a uniform patrol distribution. Moreover, the three measures are not necessarily positively or negatively correlated. For example, both the protected area (PA) and weighted profit (WP) in Figure 5.16 are larger then those in Figure 5.14 and 5.15, although in many cases PA decrease if WP increases. This feature adds to the complexity of finding an "optimal" patrol strategy.

Finally, we consider a patrol strategy that puts more effort along specific waterways than any of previous strategies in addition to targeting highways and high-benefit regions. We mark the selected waterways in Figure 5.17(a) with blue curves. As we will discuss in Section 5.3.2.5, the waterways are in many optimal paths. We define a new distance function $\hat{d}(x)$ that calculates the minimum Euclidean distance to major highways and the selected waterways. We modify the patrol function in equation (5.18) to obtain the following

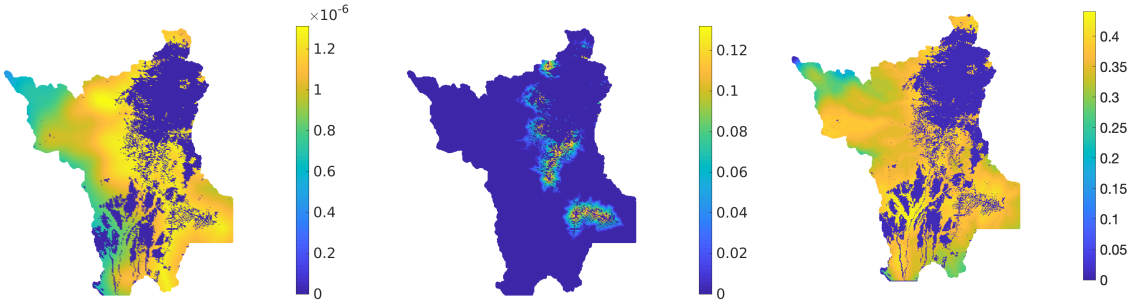

(a) Capture intensity (b) Profit P_+ (c) Optimal logging time

Figure 5.15: (a) Capture intensity is based on benefit and distance, with $w = 0.2$ and $r = 5$ in equation (5.18). (b) Expected non-negative profit P_+ for the entire region. (c) Optimal logging time on regions with positive benefit.

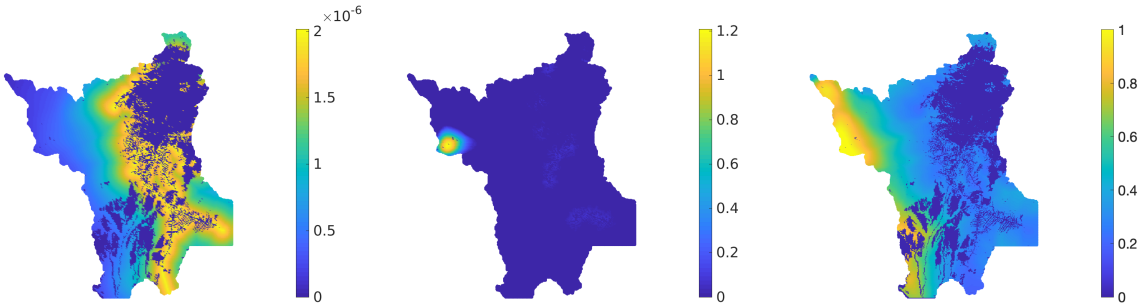

(a) Capture intensity (b) Profit P_+ (c) Optimal logging time

Figure 5.16: (a) Capture intensity is based on benefit and distance, with $w = 0.2$ and $r = 15$ in equation (5.18). (b) Expected non-negative profit P_+ for the entire region. (c) Optimal logging time on regions with positive benefit.

strategy:

$$\psi(x) = \frac{B(x)^w E}{(1+\mu\hat{d}(x))^r \int_\Omega B(x)^w (1+\mu d(x))^2 (1+\mu\hat{d}(x))^{-r}\, dx}\,. \tag{5.19}$$

In Figure 5.17, we plot the results when $w = 0.2$ and $r = 15$. Because loggers have to reroute to avoid heavy patrolling (see Figure 5.18(d)), the profit is less than that of previous strategies.

All of our numerical experiments indicate that both distance and potential benefit are

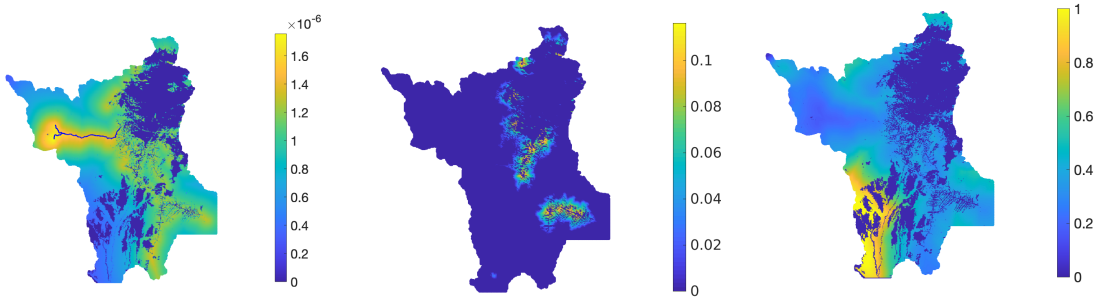

(a) Capture intensity

(b) Profit P_+

(c) Optimal logging time

Figure 5.17: (a) Capture intensity is based on benefit and distance to both highways and waterways, with $w = 0.2$ and $r = 15$ in equation (5.19). (b) Expected non-negative profit P_+ for the entire region. (c) Optimal logging time on regions with positive benefit.

important factors for patrol allocation. For now, we do not have a method to find optimal patrol strategies, but our model can be applied to evaluate and compare different strategies.

5.3.2.5 Example 5: Optimal paths

We now calculate and compare optimal paths in different regions under different patrol strategies. We randomly sample 500 target locations with probabilities that are proportional to the non-negative profits in Figure 5.8(b). We plot the optimal paths that go to each of these points in Figure 5.18(a) and show the optimal paths that return from these points under different patrol strategies in Figures 5.18(b)–5.18(d). As discussed previously (see Section 5.2.2), the optimal paths that go to the targets are the same regardless of the patrol strategy. To convey the differences between these paths, we plot the paths that leave the target points (blue curves) on top of those that go to the target points (red curves) in panels (b)–(d). Figure 5.18(b) illustrates that most of the optimal paths that enter and leave the forest are very similar under the patrol strategy in Figure 5.13. As we increase the nonuniformity of capture intensity by focusing more on the northwest corner (see Figure 5.11), we observe a major change in Figure 5.18(c). Loggers now choose a different route to

Patrol based on	Parameters	WP	PA	PB	Index
Distance only	$r = 1$	0.1321	0.7667	0.6912	(1)
	$r = 5$	0.3419	0.7702	0.6231	(2)
	$r = 15$	1.6289	0.7632	0.5311	(3)
Benefit only	$w = 1$	0.1774	0.7493	0.7827	(4)
	$w = 0.5$	0.1130	0.8108	0.8376	(5)
	$w = 0.2$	0.0917	0.8384	0.8600	(6)
Benefit and distance to highways	$w = 0.2$, $r = 1$	0.0773	0.8611	0.8791	(7)
	$w = 0.2$, $r = 5$	0.0683	0.8863	0.9059	(8)
	$w = 0.2$, $r = 15$	0.6714	0.9056	0.7695	(9)
Benefit and distance to highways and waterways	$w = 0.2$, $r = 15$	0.0582	0.8944	0.9101	(10)

Table 5.1: Results of numerical experiments with different patrol strategies. We defined the evaluation measures WP, PA, and PB in Section 5.3.1.

avoid patrols and return to a different municipality than the one from which they started. Nevertheless, many optimal paths that go deeper into the forest in the northwest corner cluster into one trajectory; one reason for this is that the capture intensity is much more uniform than the travel speed due to the presence of rivers. The fast travel speed along the river outweighs the risk of being captured. With this in mind, we design the patrol strategy that we plot in Figure 5.17; in this patrol strategy, we target waterways that attract loggers. As expected, the corresponding optimal paths in Figure 5.18(d) demonstrate huge differences from those in Figure 5.18(bc). Because of these differences, this patrol strategy (see Figure 5.17) achieves the smallest WP and the largest PB in Table 5.1. This result again emphasizes the importance of spatially targeted patrolling.

5.4 Conclusions and discussion

We presented a control-theoretic model to infer the behavior of uncontrolled loggers, including their travel paths and target logging locations. We consider logging events that are sufficiently lucrative for the criminals so that they are willing to incur some risk of be-

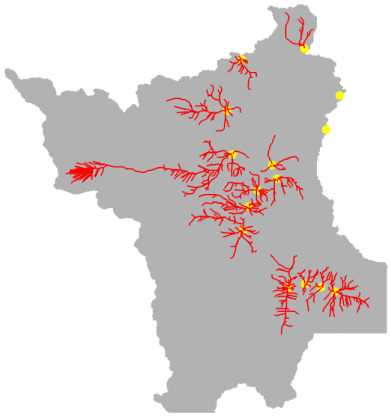

(a) Optimal paths entering the forest

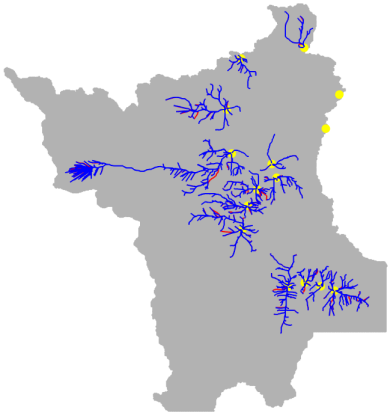

(b) Optimal paths leaving the forest with the patrol function in Figure 5.13

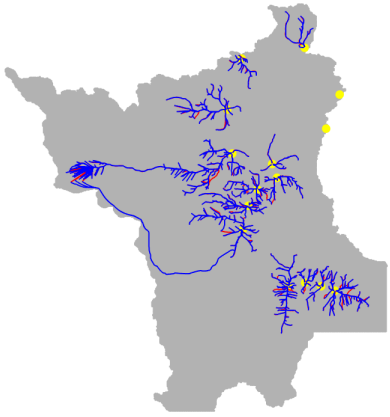

(c) Optimal paths leaving the forest with the patrol function in Figure 5.11

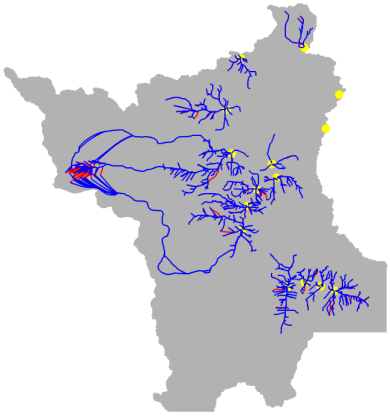

(d) Optimal paths leaving the forest with the patrol function in Figure 5.17

Figure 5.18: We sample 500 target points in the region with probabilities that are proportional to the non-negative profits in Figure 5.8(b). We plot the optimal paths entering the forest in panel (a) and the optimal paths leaving the forest in panels (b)–(d). We write the deployed patrols in the subtitles. We plot the departing paths (blue) on top of the entering paths (red) in panels (b)–(d). Yellow dots mark the 15 municipalities.

ing caught. The criminals balance that risk against the benefit to find an optimal logging duration. Our model quantifies the intensity of a logging event, in contrast to models in

which deforestation events clear all of the trees from an area. We believe that our approach is more realistic because the PRODES data set [IN] shows that trees are still present in many locations where past deforestation events have occurred. We detailed the underlying mathematical formalism, including the numerical schemes that we used to simulate our model. Finally, we explored the influence of different parameter values through numerical experiments and compared different patrol strategies.

Our model is built on the idea that efficient patrols against deforestation should be spatially targeted, rather than applied uniformly across a territory. This assumption comports with the targeted nature of deforestation enforcement policies used by many countries. However, the most efficient patrols that we obtained in our experiments require more precise spatial targeting than the ones that are specified by most existing public policies. Such policies typically target administrative units (e.g., municipalities in Brazil) or other large swaths of a forest. There are clear tradeoffs between precise and blunt targeting, including challenges in patrol-strategy implementation, difficulties in communication of control strategies, and political costs of targeting. The model that we developed in this chapter reveals the necessity to study these tradeoffs to improve the efficacy of deforestation control policies.

We now discuss several directions for future work. First, one of the basic assumptions in our model is that the loggers know the precise patrol strategy. This is a standard game-theoretic simplification, but we expect that it is false in reality. Incorporation of imperfect knowledge (perhaps using stochastic effects) may better model the strategic game between the criminals and the patrol. Relevant work exists on surveillance uncertainty in reach–avoid games [GV20]. Second, although our model can evaluate a suggested patrol strategy, we are not able to find optimal patrol strategies using our current formulation. It would be useful to design a model that can resolve optimal strategies or suggest a constructive method for improving a given suboptimal strategy. Additionally, our model is static. One can envision a time-series model such that the model that we have described in this chapter is one stage in an ongoing game and the patrol strategy can change with time. Studying the

long-term behavior of such a model may provide additional insight into the expected amount of deforestation over long stretches of time.

CHAPTER 6

Conclusions

In this thesis, we developed and studied several models of human dynamics. We discussed a model of coupled epidemic spread and opinion spread and a model of opinion spread in the form of dynamical processes on multilayer networks. We then discussed a model of human movement using optimal control.

We introduced a model of the spread of a infectious disease when competing opinions on physical distancing spread concurrently in a population. Our model takes the form of a dynamical system on a two-layer multiplex network. We assumed that the disease and the opinions spread on different layers following compartmental models. We developed a degree-based pair approximation for the time evolution of population-scale quantities. Using direct numerical simulations and our pair approximation, we explored the influence of opinion spread on disease spread. We also explored the influence of several network structures on the dynamics.

We extended a majority-vote model to two-layer multiplex networks. In our model, neighbors in one layer are more influential at changing an individual's opinion than neighbors in the other layer. We studied our model on multiplex networks with community structure in which we controlled intralayer community strength and interlayer community correlation. We found three different types of steady-state behavior — fully mixed, consensus, and polarized steady states. We studied phase transitions with a mean-field approximation and obtained results that are close to those that we observed using direct numerical simulations. We found that a stronger interlayer community correlation results in polarized steady states being

reachable for wider ranges of the other model parameters. We also found that different values of the layer-preference parameter (which quantifies the degree to which neighbors in one layer are more influential than neighbors in the other layer) result in qualitatively different phase diagrams for the mean opinions at steady states.

Finally, we studied a model of illegal logging. We examined the behavior of illegal loggers who want to maximize their profit by balancing benefit and cost. We formulated our model as an optimal control problem and solved it numerically using a fast-sweeping method. Our numerical experiments demonstrated that, in our model, spatially targeted patrols are more efficient than uniform patrols at deterring illegal logging.

Our three models of human dynamics are inspired by real-life applications. However, much work is necessary before it is possible to use such models to truly address real-world issues. Our models rely on many assumptions. We make some of the assumptions to simplify analysis and calculations. These assumptions are generally not true. For example, a more realistic effect of adopting an opinion on physical distancing is to change contact patterns rather than to change the disease transmission rate. It is important to develop new mathematical tools to solve the more sophisticated mathematical problems that we obtain when we relax these assumptions. Moreover, some of our assumptions are inherently hard to verify. One example is how opinions change under peer pressure. In this case, comparing the behavior of our models and of variations of our models with empirical data is essential to help evaluate these assumptions. Even with these drawbacks, we believe that our models improve upon previous works and can provide insights for future research.

REFERENCES

[Aca08] Adam Acar. "Antecedents and consequences of online social networking behavior: The case of Facebook." *Journal of Website Promotion*, **3**(1–2):62–83, 2008.

[AFJ19] David J Arnold, Dayne Fernandez, Ruizhe Jia, Christian Parkinson, Deborah Tonne, Yotam Yaniv, Andrea L Bertozzi, and Stanley J Osher. "Modeling environmental crime in protected areas using the level set method." *SIAM Journal on Applied Mathematics*, **79**(3):802–821, 2019.

[AGR15] Juliano Assunção, Clarissa Gandour, and Rudi Rocha. "Deforestation slowdown in the Brazilian Amazon: Prices or policies?" *Environment and Development Economics*, **20**(6):697–722, 2015.

[Alb10] Heidi J Albers. "Spatial modeling of extraction and enforcement in developing country protected areas." *Resource and Energy Economics*, **32**(2):165–179, 2010.

[AM92] Roy M Anderson and Robert M May. *Infectious Diseases of Humans: Dynamics and Control*. Oxford University Press, Oxford, UK, 1992.

[AM19] Alberto Aleta and Yamir Moreno. "Multilayer networks in a nutshell." *Annual Review of Condensed Matter Physics*, **10**:45–62, 2019.

[ANS21] Folashade B. Agusto, Eric Numfor, Karthik Srinivasan, Enahoro Iboi, Alexander Fulk, Jarron M. Saint Onge, and Townsend Peterson. "Impact of public sentiments on the transmission of COVID-19 across a geographical gradient." *medRxiv*, 2021. 10.1101/2021.01.29.21250655.

[Ari22] Julien Arino. "Describing, modelling and forecasting the spatial and temporal spread of COVID-19: A short review." In V. Kumar Murty and Jianhong Wu, editors, *Mathematics of Public Health: Proceedings of the Seminar on the Mathematical Modelling of COVID-19*, pp. 25–51. Springer International Publishing, Cham, Switzerland, 2022.

[Asc51] Solomon E Asch. "Effects of group pressure upon the modification and distortion of judgments." In Harold Guetzkow, editor, *Groups, Leadership and Men: Research in Human Relations*, pp. 177–190. Carnegie Press, Pittsburgh, PA, 1951.

[ASM15] Claudia Azevedo-Ramos, José Natalino Macedo Silva, Frank Merry, Anne R Kapuscinski, Peter C Frumhoff, and Kim Locke. "The evolution of Brazilian forest concessions." *Elementa: Science of the Anthropocene*, **3**, 2015.

[ASV14] Ana L Acuña-Lara, Francisco Sastre, and José Raúl Vargas-Arriola. "Critical phenomena in the majority voter model on two-dimensional regular lattices." *Physical Review E*, **89**(5):052109, 2014.

[BA99] Albert-László Barabási and Réka Albert. "Emergence of scaling in random networks." *Science*, **286**(5439):509–512, 1999.

[Bar05] Albert-László Barabási. "Taming complexity." *Nature physics*, **1**(2):68–70, 2005.

[BBC20] Nicola Bellomo, Richard Bingham, Mark A J Chaplain, Giovanni Dosi, Guido Forni, Damian A Knopoff, John Lowengrub, Reidun Twarock, and Maria Enrica Virgillito. "A multiscale model of virus pandemic: Heterogeneous interactive entities in a globally connected world." *Mathematical Models and Methods in Applied Sciences*, **30**(8):1591–1651, 2020.

[BBP04] Alain Barrat, Marc Barthelemy, Romualdo Pastor-Satorras, and Alessandro Vespignani. "The architecture of complex weighted networks." *Proceedings of the National Academy of Sciences of the United States of America*, **101**(11):3747–3752, 2004.

[BC08] Martino Bardi and Italo Capuzzo-Dolcetta. *Optimal Control and Viscosity Solutions of Hamilton-Jacobi-Bellman Equations*. Birkhäuser, Boston, MA, 2008.

[BC19] David E Bloom and Daniel Cadarette. "Infectious disease threats in the twenty-first century: Strengthening the global response." *Frontiers in Immunology*, **10**:549, 2019.

[BCC12] Fred Brauer, Carlos Castillo-Chavez, and Carlos Castillo-Chavez. *Mathematical Models in Population Biology and Epidemiology*. Springer, New York, NY, second edition, 2012.

[BCF19] Fred Brauer, Carlos Castillo-Chavez, and Zhilan Feng. *Mathematical Models in Epidemiology*, volume 32. Springer-Verlag, Heidelberg, Germany, 2019.

[BCK06] Luís MA Bettencourt, Ariel Cintrón-Arias, David I Kaiser, and Carlos Castillo-Chávez. "The power of a good idea: Quantitative modeling of the spread of ideas from epidemiological models." *Physica A: Statistical Mechanics and its Applications*, **364**:513–536, 2006.

[BD99] Michelle Boué and Paul Dupuis. "Markov chain approximations for deterministic control problems with affine dynamics and quadratic cost in the control." *SIAM Journal on Numerical Analysis*, **36**(3):667–695, March 1999.

[BF07] Martin CJ Bootsma and Neil M Ferguson. "The effect of public health measures on the 1918 influenza pandemic in US cities." *Proceedings of the National Academy of Sciences of the United States of America*, **104**(18):7588–7593, 2007.

[BFM20] Andrea L Bertozzi, Elisa Franco, George Mohler, Martin B Short, and Daniel Sledge. "The challenges of modeling and forecasting the spread of COVID-19." *Proceedings of the National Academy of Sciences of the United States of America*, **117**(29):16732–16738, 2020.

[BG09] Jørgen Bang-Jensen and Gregory Z Gutin. *Digraphs: Theory, Algorithms and Applications*. Springer, London, second edition, 2009.

[BJA20] Marya Bazzi, Lucas GS Jeub, Alex Arenas, Sam D Howison, and Mason A Porter. "A framework for the construction of generative models for mesoscale structure in multilayer networks." *Physical Review Research*, **2**(2):023100, 2020.

[BNM18] Maira Bolfe, Lucas Nicolao, and Fernando L Metz. "Phase diagram and metastability of the Ising model on two coupled networks." *Journal of Statistical Mechanics: Theory and Experiment*, **2018**(8):083404, 2018.

[BP16] Albert-László Barabási and Márton Pósfai. *Network Science*. Cambridge University Press, Cambridge, UK, 2016.

[BSP21] Jamie Bedson, Laura A Skrip, Danielle Pedi, Sharon Abramowitz, Simone Carter, Mohamed F Jalloh, Sebastian Funk, Nina Gobat, Tamara Giles-Vernick, Gerardo Chowell, João Rangel de Almeida, Rania Elessawi, Samuel V Scarpino, Ross A Hammond, Sylvie Briand, Joshua M Epstein, Laurent Hébert-Dufresne, and Benjamin M Althouse. "A review and agenda for integrated disease models including social and behavioural factors." *Nature Human Behaviour*, **5**(7):834–846, 2021.

[CBB10] Ciro Cattuto, Wouter Van den Broeck, Alain Barrat, Vittoria Colizza, Jean-François Pinton, and Alessandro Vespignani. "Dynamics of person-to-person interactions from distributed RFID sensor networks." *PLoS One*, **5**(7):e11596, 2010.

[CES06] Xavier Castelló, Víctor M Eguíluz, and Maxi San Miguel. "Ordering dynamics with two non-excluding options: Bilingualism in language competition." *New Journal of Physics*, **8**(12):308, 2006.

[CFL09] Claudio Castellano, Santo Fortunato, and Vittorio Loreto. "Statistical physics of social dynamics." *Reviews of Modern Physics*, **81**:591–646, May 2009.

[CG19] Jeehye Choi and Kwang-Il Goh. "Majority-vote dynamics on multiplex networks with two layers." *New Journal of Physics*, **21**(3):035005, 2019.

[CL83] Michael G. Crandall and Pierre-Louis Lions. "Viscosity solutions of Hamilton–Jacobi equations." *Transactions of the American Mathematical Society*, **277**(1):1–42, 1983.

[CMG21] Matteo Cinelli, Gianmarco De Francisci Morales, Alessandro Galeazzi, Walter Quattrociocchi, and Michele Starnini. "The echo chamber effect on social media." *Proceedings of the National Academy of Sciences of the United States of America*, **118**(9), 2021.

[COM03] Paulo R A Campos, Viviane M de Oliveira, and F G Brady Moreira. "Small-world effects in the majority-vote model." *Physical Review E*, **67**(2):026104, 2003.

[CPP21] Bohan Chen, Kaiyan Peng, Christian Parkinson, Andrea L Bertozzi, Tara Lyn Slough, and Johannes Urpelainen. "Modeling illegal logging in Brazil." *Research in the Mathematical Sciences*, **8**(2):1–21, 2021.

[CS73] Peter Clifford and Aidan Sudbury. "A model for spatial conflict." *Biometrika*, **60**(3):581–588, 1973.

[CSN09] Aaron Clauset, Cosma Rohilla Shalizi, and Mark E J Newman. "Power-law distributions in empirical data." *SIAM Review*, **51**(4):661–703, 2009.

[CSS17] Anna Chmiel, Julian Sienkiewicz, and Katarzyna Sznajd-Weron. "Tricriticality in the q-neighbor Ising model on a partially duplex clique." *Physical Review E*, **96**(6):062137, 2017.

[CV12] Adam Chacon and Alexander Vladimirsky. "Fast two-scale methods for Eikonal equations." *SIAM Journal on Scientific Computing*, **34**(2):A547–A578, 2012.

[CV20] Elliot Cartee and Alexander Vladimirsky. "Control-theoretic models of environmental crime." *SIAM Journal on Applied Mathematics*, **80**(3):1441–1466, 2020.

[DB14] Florian Dörfler and Francesco Bullo. "Synchronization in complex networks of phase oscillators: A survey." *Automatica*, **50**(6):1539–1564, 2014.

[DBZ16] Michela Del Vicario, Alessandro Bessi, Fabiana Zollo, Fabio Petroni, Antonio Scala, Guido Caldarelli, H Eugene Stanley, and Walter Quattrociocchi. "The spreading of misinformation online." *Proceedings of the National Academy of Sciences of the United States of America*, **113**(3):554–559, 2016.

[DC07] Luca Dall'Asta and Claudio Castellano. "Effective surface-tension in the noise-reduced voter model." *Europhysics Letters*, **77**(6):60005, 2007.

[DHB12] Odo Diekmann, Hans Heesterbeek, and Tom Britton. *Mathematical Tools for Understanding Infectious Disease Dynamics*. Princeton University Press, Princeton, NJ, 2012.

[DHM90] Odo Diekmann, Johan Andre Peter Heesterbeek, and Johan A J Metz. "On the definition and the computation of the basic reproduction ratio R_0 in models for infectious diseases in heterogeneous populations." *Journal of Mathematical Biology*, **28**(4):365–382, 1990.

[DL94] Richard Durrett and Simon Levin. "The importance of being discrete (and spatial)." *Theoretical Population Biology*, **46**(3):363–394, 1994.

[DNA00] Guillaume Deffuant, David Neau, Frederic Amblard, and Gérard Weisbuch. "Mixing beliefs among interacting agents." *Advances in Complex Systems*, **3**(01n04):87–98, 2000.

[DNL16] Marina Diakonova, Vincenzo Nicosia, Vito Latora, and Maxi San Miguel. "Irreducibility of multilayer network dynamics: The case of the voter model." *New Journal of Physics*, **18**(2):023010, 2016.

[DPS09] Subinay Dasgupta, Raj Kumar Pan, and Sitabhra Sinha. "Phase of Ising spins on modular networks analogous to social polarization." *Physical Review E*, **80**(2):025101, 2009.

[DSC13] Manlio De Domenico, Albert Solé-Ribalta, Emanuele Cozzo, Mikko Kivelä, Yamir Moreno, Mason A Porter, Sergio Gómez, and Alex Arenas. "Mathematical formulation of multilayer networks." *Physical Review X*, **3**(4):041022, 2013.

[Dur19] Rick Durrett. *Probability: Theory and Examples*. Cambridge University Press, Cambridge, UK, fifth edition, 2019.

[EHC21] Joshua M Epstein, Erez Hatna, and Jennifer Crodelle. "Triple contagion: A two-fears epidemic model." *Journal of the Royal Society Interface*, **18**(181):20210186, 2021.

[EK02] Ken T D Eames and Matt J Keeling. "Modeling dynamic and network heterogeneities in the spread of sexually transmitted diseases." *Proceedings of the National Academy of Sciences of the United States of America*, **99**(20):13330–13335, 2002.

[ER59] Paul Erdős and Alfréd Rényi. "On random graphs I." *Publicationes Mathematicae Debrecen*, **6**:290–297, 1959.

[ER60] Paul Erdős and Alfréd Rényi. "On the evolution of random graphs." *Publications of the Mathematical Institute of the Hungarian Academy of Sciences*, **5**(1):17–60, 1960.

[ER61] Paul Erdős and Alfréd Rényi. "On the strength of connectedness of a random graph." *Acta Mathematica Hungarica*, **12**(1):261–267, 1961.

[Est12] Ernesto Estrada. *The Structure of Complex Networks: Theory and Applications*. Oxford University Press, Oxford, UK, 2012.

[Est20] Ernesto Estrada. "COVID-19 and SARS-CoV-2. Modeling the present, looking at the future." *Physics Reports*, **869**:1–51, 2020.

[Fea05] Philip M Fearnside. "Deforestation in Brazilian Amazonia: History, rates, and consequences." *Conservation Biology*, **19**(3):680–688, 2005.

[FF16] Maurizio Falcone and Roberto Ferretti. "Numerical methods for Hamilton–Jacobi type equations." In Rémi Abgrall and Chi-Wang Shu, editors, *Handbook of Numerical Analysis*, volume 17, pp. 603–626. Elsevier, Amsterdam, Netherlands, 2016.

[FGJ10] Sebastian Funk, E Gilad, and Vincent A A Jansen. "Endemic disease, awareness, and local behavioural response." *Journal of Theoretical Biology*, **264**(2):501–509, 2010.

[FGW09] Sebastian Funk, Erez Gilad, Chris Watkins, and Vincent A A Jansen. "The spread of awareness and its impact on epidemic outbreaks." *Proceedings of the National Academy of Sciences of the United States of America*, **106**(16):6872–6877, 2009.

[FH16] Santo Fortunato and Darko Hric. "Community detection in networks: A user guide." *Physics Reports*, **659**:1–44, 2016.

[FJT13] Fei Fang, Albert Xin Jiang, and Milind Tambe. "Optimal patrol strategy for protecting moving targets with multiple mobile resources." In *Proceedings of the 2013 international conference on Autonomous agents and multi-agent systems*, pp. 957–964. International Foundation for Autonomous Agents and Multiagent Systems, 2013.

[FLN18] Bailey K Fosdick, Daniel B Larremore, Joel Nishimura, and Johan Ugander. "Configuring random graph models with fixed degree sequences." *SIAM Review*, **60**(2):315–355, 2018.

[FM21] Dennis M Feehan and Ayesha S Mahmud. "Quantifying population contact patterns in the United States during the COVID-19 pandemic." *Nature Communications*, **12**(1):893, 2021.

[FMF17] Andreas Flache, Michael Mäs, Thomas Feliciani, Edmund Chattoe-Brown, Guillaume Deffuant, Sylvie Huet, and Jan Lorenz. "Models of social influence: Towards the next frontiers." *Journal of Artificial Societies and Social Simulation*, **20**(4):2, 2017.

[FNP17] Fei Fang, Thanh H Nguyen, Rob Pickles, Wai Y Lam, Gopalasamy R Clements, Bo An, Amandeep Singh, Brian C Schwedock, Milin Tambe, and Andrew Lemieux. "PAWS—A deployed game-theoretic application to combat poaching." *AI Magazine*, **38**(1):23–36, 2017.

[FRC07] Tom G Farr, Paul A Rosen, Edward Caro, Robert Crippen, Riley Duren, Scott Hensley, Michael Kobrick, Mimi Paller, Ernesto Rodriguez, Ladislav Roth, et al. "The shuttle radar topography mission." *Reviews of Geophysics*, **45**(2), 2007.

[FSJ10] Sebastian Funk, Marcel Salathé, and Vincent A A Jansen. "Modelling the influence of human behaviour on the spread of infectious diseases: A review." *Journal of the Royal Society Interface*, **7**(50):1247–1256, 2010.

[Gab20] Adam Gabbatt. "US anti-lockdown rallies could cause surge in COVID-19 cases, experts warn." *The Guardian*, Apr

2020. https://www.theguardian.com/us-news/2020/apr/20/us-protests-lockdown-coronavirus-cases-surge-warning (20 April 2020).

[Gal02] Serge Galam. "Minority opinion spreading in random geometry." *The European Physical Journal B-Condensed Matter and Complex Systems*, **25**(4):403–406, 2002.

[GB08] Thilo Gross and Bernd Blasius. "Adaptive coevolutionary networks: A review." *Journal of the Royal Society Interface*, **5**(20):259–271, 2008.

[GF20] Alina Glaubitz and Feng Fu. "Oscillatory dynamics in the dilemma of social distancing." *Proceedings of the Royal Society A*, **476**(2243):20200686, 2020.

[GGA13] Clara Granell, Sergio Gómez, and Alex Arenas. "Dynamical interplay between awareness and epidemic spreading in multiplex networks." *Physical Review Letters*, **111**(12):128701, 2013.

[GGA14] Clara Granell, Sergio Gómez, and Alex Arenas. "Competing spreading processes on multiplex networks: Awareness and epidemics." *Physical Review E*, **90**(1):012808, 2014.

[GJL15] Quantong Guo, Xin Jiang, Yanjun Lei, Meng Li, Yifang Ma, and Zhiming Zheng. "Two-stage effects of awareness cascade on epidemic spreading in multiplex networks." *Physical Review E*, **91**(1):012822, 2015.

[GK20] Tomasz Gradowski and Andrzej Krawiecki. "Pair approximation for the q-voter model with independence on multiplex networks." *Physical Review E*, **102**(2):022314, 2020.

[Gle11] James P Gleeson. "High-accuracy approximation of binary-state dynamics on networks." *Physical Review Letters*, **107**(6):068701, 2011.

[Gle13] James P Gleeson. "Binary-state dynamics on complex networks: Pair approximation and beyond." *Physical Review X*, **3**(2):021004, 2013.

[GLJ16] Quantong Guo, Yanjun Lei, Xin Jiang, Yifang Ma, Guanying Huo, and Zhiming Zheng. "Epidemic spreading with activity-driven awareness diffusion on multiplex network." *Chaos*, **26**(4):043110, 2016.

[GMW12] James P Gleeson, Sergey Melnik, Jonathan A Ward, Mason A Porter, and Peter J Mucha. "Accuracy of mean-field theory for dynamics on real-world networks." *Physical Review E*, **85**(2):026106, 2012.

[GN64] William Goffman and V Newill. "Generalization of epidemic theory." *Nature*, **204**(4955):225–228, 1964.

[Gre21] Catherine Greenhill. "Generating graphs randomly." In Konrad K. Dabrowski, Maximilien Gadouleau, Nicholas Georgiou, Matthew Johnson, George B. Mertzios, and DaniëlEditors Paulusma, editors, *Surveys in Combinatorics 2021*, London Mathematical Society Lecture Note Series, pp. 133–186. Cambridge University Press, Cambridge, UK, 2021.

[GV20] Marc Aurèle Gilles and Alexander Vladimirsky. "Evasive path planning under surveillance uncertainty." *Dynamic Games and Applications*, **10**(2):391–416, 2020.

[GVC20] Riccardo Gallotti, Francesco Valle, Nicola Castaldo, Pierluigi Sacco, and Manlio De Domenico. "Assessing the risks of 'infodemics' in response to COVID-19 epidemics." *Nature Human Behaviour*, **4**(12):1285–1293, 2020.

[HCS15] Feng Huang, Han-Shuang Chen, and Chuan-Sheng Shen. "Phase transitions of majority-vote model on modular networks." *Chinese Physics Letters*, **32**(11):118902, 2015.

[HK02] Rainer Hegselmann and Ulrich Krause. "Opinion dynamics and bounded confidence models, analysis, and simulation." *Journal of Artificial Societies and Social Simulation*, **5**(3), 2002.

[HL75] Richard A Holley and Thomas M Liggett. "Ergodic theorems for weakly interacting infinite systems and the voter model." *The Annals of Probability*, pp. 643–663, 1975.

[HL14] Nathan O. Hodas and Kristina Lerman. "The Simple Rules of Social Contagion." *Scientific Reports*, **4**:4343, 2014.

[HLL83] Paul W Holland, Kathryn Blackmond Laskey, and Samuel Leinhardt. "Stochastic blockmodels: First steps." *Social Networks*, **5**(2):109–137, 1983.

[HPL06] Liang Huang, Kwangho Park, and Ying-Cheng Lai. "Information propagation on modular networks." *Physical Review E*, **73**(3):035103, 2006.

[IC18] Ian J Irmischer and Keith C Clarke. "Measuring and modeling the speed of human navigation." *Cartography and Geographic Information Science*, **45**(2):177–186, 2018.

[IDC22] Giulio Iannelli, Giordano De Marzo, and Claudio Castellano. "Filter bubble effect in the multistate voter model." *Chaos*, **32**(4):043103, 2022.

[IN] National Institute of Space Research (INPE). "PRODES deforestation." Accessed through Global Forest Watch (www.globalforestwatch.org) in 07/2019.

[Jac16] Rachel Jackson. "A credible commitment: Reducing deforestation in the Brazilian Amazon, 2003–2012." *Princeton University: Innovations for Successful Societies*, **15**, 2016.

[JFT12] Matthew Johnson, Fei Fang, and Milind Tambe. "Patrol strategies to maximize pristine forest area." In *Proceedings of the AAAI Conference on Artificial Intelligence*, volume 26, pp. 295–301, 2012.

[JP20] Matthew D Johnston and Bruce Pell. "A dynamical framework for modeling fear of infection and frustration with social distancing in COVID-19 spread." *Mathematical Biosciences and Engineering*, **17**:7892, 2020.

[JVR20] Neil F Johnson, Nicolas Velásquez, Nicholas Johnson Restrepo, Rhys Leahy, Nicholas Gabriel, Sara El Oud, Minzhang Zheng, Pedro Manrique, Stefan Wuchty, and Yonatan Lupu. "The online competition between pro-and anti-vaccination views." *Nature*, **582**(7811):230–233, 2020.

[KAB14] Mikko Kivelä, Alex Arenas, Marc Barthelemy, James P Gleeson, Yamir Moreno, and Mason A Porter. "Multilayer networks." *Journal of Complex Networks*, **2**(3):203–271, 2014.

[KBS16] Kaj-Kolja Kleineberg, Marián Boguná, M Ángeles Serrano, and Fragkiskos Papadopoulos. "Hidden geometric correlations in real multiplex networks." *Nature Physics*, **12**(11):1076–1081, 2016.

[KFD15] Debarun Kar, Fei Fang, Francesco Delle Fave, Nicole Sintov, and Milind Tambe. "A game of thrones: When human behavior models compete in repeated Stackelberg security games." In *Proceedings of the 2015 International Conference on Autonomous Agents and Multiagent Systems*, pp. 1381–1390. International Foundation for Autonomous Agents and Multiagent Systems, 2015.

[KFG17] Debarun Kar, Benjamin Ford, Shahrzad Gholami, Fei Fang, Andrew Plumptre, Milind Tambe, Margaret Driciru, Fred Wanyama, Aggrey Rwetsiba, Mustapha Nsubaga, and Joshua Mabonga. "Cloudy with a chance of poaching: Adversary behavior modeling and forecasting with real-world poaching data." In *Proceedings of the 16th Conference on Autonomous Agents and MultiAgent Systems*, AAMAS '17, p. 159–167, Richland, SC, 2017. International Foundation for Autonomous Agents and Multiagent Systems.

[KGF18] Nitin Kamra, Umang Gupta, Fei Fang, Yan Liu, and Milind Tambe. "Policy learning for continuous space security games using neural networks." *Proc. 32nd AAAI Conference on Artificial Intelligence*, 2018.

[KGK08] István Z Kiss, Darren M Green, and Rowland R Kao. "The effect of network mixing patterns on epidemic dynamics and the efficacy of disease contact tracing." *Journal of the Royal Society Interface*, **5**(24):791–799, 2008.

[KGS18] A Krawiecki, T Gradowski, and G Siudem. "Majority vote model on multiplex networks." *Acta Physica Polonica A*, **133**:1433–1440, 2018.

[KLT08] Peter Klimek, Renaud Lambiotte, and Stefan Thurner. "Opinion formation in laggard societies." *Europhysics Letters*, **82**(2):28008, 2008.

[KM27] William O Kermack and Anderson G McKendrick. "A contribution to the mathematical theory of epidemics." *Proceedings of the Royal Society of London. Series A, Mathematical and Physical Sciences*, **115**(772):700–721, 1927.

[KMS17] István Z Kiss, Joel C Miller, and Péter L Simon. *Mathematics of Epidemics on Networks: From Exact to Approximate Models*, volume 598. Springer International Publishing, Cham, Switzerland, 2017.

[KN11] Brian Karrer and Mark E J Newman. "Competing epidemics on complex networks." *Physical Review E*, **84**:036106, 2011.

[KRM97] Matthew J Keeling, David A Rand, and Andrew J Morris. "Correlation models for childhood epidemics." *Proceedings of the Royal Society of London. Series B, Biological Sciences*, **264**(1385):1149–1156, 1997.

[Kue16] Christian Kuehn. "Moment closure — A brief review." *Control of self-organizing nonlinear systems*, pp. 253–271, 2016.

[LA07] Renaud Lambiotte and Marcel Ausloos. "Coexistence of opposite opinions in a network with communities." *Journal of Statistical Mechanics: Theory and Experiment*, **2007**(08):P08026, 2007.

[LA18] Sune Lehmann and Yong-Yeol Ahn. *Complex Spreading Phenomena in Social Systems: Influence and Contagion in Real-World Social Networks*. Springer International Publishing, Cham, Switzerland, 2018.

[LAA18] Quan-Hui Liu, Marco Ajelli, Alberto Aleta, Stefano Merler, Yamir Moreno, and Alessandro Vespignani. "Measurability of the epidemic reproduction number in data-driven contact networks." *Proceedings of the National Academy of Sciences of the United States of America*, **115**(50):12680–12685, 2018.

[LAH07] Renaud Lambiotte, Marcel Ausloos, and Janusz A Hołyst. "Majority model on a network with communities." *Physical Review E*, **75**(3):030101, 2007.

[LAS02] William F Laurance, Ana K M Albernaz, Götz Schroth, Philip M Fearnside, Scott Bergen, Eduardo M Venticinque, and Carlos Da Costa. "Predictors of deforestation in the Brazilian Amazon." *Journal of Biogeography*, **29**(5-6):737–748, 2002.

[LBG14] Kyu-Min Lee, Charles D Brummitt, and K-I Goh. "Threshold cascades with response heterogeneity in multiplex networks." *Physical Review E*, **90**(6):062816, 2014.

[LH05] Zonghua Liu and Bambi Hu. "Epidemic spreading in community networks." *Europhysics Letters*, **72**(2):315, 2005.

[Lig85] Thomas M Liggett. *Interacting Particle Systems*, volume 2. Springer, Berlin, Heidelberg, 1985.

[Lig10] Thomas M Liggett. *Continuous Time Markov Processes: An Introduction*, volume 113. American Mathematical Society, Providence, Rhode Island, 2010.

[Lim06] Francisco W S Lima. "Majority-vote on directed Barabási–Albert networks." *International Journal of Modern Physics C*, **17**(9):1257–1265, 2006.

[Lim10] Francesco W S Lima. "Analysing and controlling the tax evasion dynamics via majority-vote model." *Journal of Physics: Conference Series*, **246**(1):012033, 2010.

[LL07] Edina M S Luz and Francisco W S Lima. "Majority-vote on directed small-world networks." *International Journal of Modern Physics C*, **18**(8):1251–1261, 2007.

[LLL21] Ming Li, Run-Ran Liu, Linyuan Lü, Mao-Bin Hu, Shuqi Xu, and Yi-Cheng Zhang. "Percolation on complex networks: Theory and application." *Physics Reports*, **907**:1–68, 2021.

[LMD11] Jennifer Lindquist, Junling Ma, P Van den Driessche, and Frederick H Willeboordse. "Effective degree network disease models." *Journal of Mathematical Biology*, **62**(2):143–164, 2011.

[LSS08] Francisco W S Lima, Alexandre O Sousa, and MA Sumuor. "Majority-vote on directed Erdős–Rényi random graphs." *Physica A: Statistical Mechanics and its Applications*, **387**(14):3503–3510, 2008.

[LV15] Deborah Lawrence and Karen Vandecar. "Effects of tropical deforestation on climate and agriculture." *Nature Climate Change*, **5**(1):27–36, 2015.

[LYW16] Kristina Lerman, Xiaoran Yan, and Xin-Zeng Wu. "The "majority illusion" in social networks." *PLoS One*, **11**(2):e0147617, 2016.

[Man22] De Domenico Manlio. *Multilayer Networks: Analysis and Visualization*. Springer, Cham, Switzerland, 2022.

[MAP11] Stefano Merler, Marco Ajelli, Andrea Pugliese, and Neil M Ferguson. "Determinants of the spatiotemporal dynamics of the 2009 H1N1 pandemic in Europe: Implications for real-time modelling." *PLoS Computational Biology*, **7**(9):e1002205, 2011.

[MFA21] Md Mofijur, I M Rizwanul Fattah, Md Asraful Alam, A B M Saiful Islam, Hwai Chyuan Ong, S M Ashrafur Rahman, Gholamhassan Najafi, Shams Forruque Ahmed, Md Alhaz Uddin, and Teuku Meurah Indra Mahlia. "Impact of COVID-19 on the social, economic, environmental and energy domains: Lessons learnt from a global pandemic." *Sustainable Production and Consumption*, **26**:343–359, 2021.

[MG05] Mauro Mobilia and Ivan T Georgiev. "Voting and catalytic processes with inhomogeneities." *Physical Review E*, **71**(4):046102, 2005.

[MGK13] Byungjoon Min, K-I Goh, and I-M Kim. "Suppression of epidemic outbreaks with heavy-tailed contact dynamics." *Europhysics Letters*, **103**(5):50002, 2013.

[MGP03] Yamir Moreno, Javier B Gómez, and Amalio F Pacheco. "Epidemic incidence in correlated complex networks." *Physical Review E*, **68**(3):035103, 2003.

[Mil13] Joel C Miller. "Cocirculation of infectious diseases on networks." *Physical Review E*, **87**(6):060801, 2013.

[Mob03] Mauro Mobilia. "Does a single zealot affect an infinite group of voters?" *Physical Rview Letters*, **91**(2):028701, 2003.

[MPM14] Sergey Melnik, Mason A Porter, Peter J Mucha, and James P Gleeson. "Dynamics on modular networks with heterogeneous correlations." *Chaos*, **24**(2):023106, 2014.

[MRB08] Yadvinder Malhi, J Timmons Roberts, Richard A Betts, Timothy J Killeen, Wenhong Li, and Carlos A Nobre. "Climate change, deforestation, and the fate of the Amazon." *Science*, **319**(5860):169–172, 2008.

[MS03] Ian M Mitchell and Shankar Sastry. "Continuous path planning with multiple constraints." In *42nd IEEE International Conference on Decision and Control (IEEE Cat. No. 03CH37475)*, volume 5, pp. 5502–5507. Institute of Electrical and Electronics Engineers, 2003.

[MSV12] Joel C Miller, Anja C Slim, and Erik M Volz. "Edge-based compartmental modelling for infectious disease spread." *Journal of the Royal Society Interface*, **9**(70):890–906, 2012.

[MTK16] Sara McCarthy, Milind Tambe, Christopher Kiekintveld, Meredith L. Gore, and Alex Killion. "Preventing illegal logging: Simultaneous optimization of resource teams and tactics for security." In *AAAI Conference on Artificial Intelligence*, 2016.

[New02] Mark E J Newman. "Assortative mixing in networks." *Physical Review Letters*, **89**(20):208701, 2002.

[New18] Mark E J Newman. *Networks*. Oxford University Press, Oxford, UK, second edition, 2018.

[NFF14] Azadeh Nematzadeh, Emilio Ferrara, Alessandro Flammini, and Yong-Yeol Ahn. "Optimal network modularity for information diffusion." *Physical Review Letters*, **113**(8):088701, 2014.

[NG03] Mark E J Newman and Michelle Girvan. "Mixing patterns and community structure in networks." In Romualdo Pastor-Satorras, Miguel Rubi, and Albert Diaz-Guilera, editors, *Statistical Mechanics of Complex Networks*, pp. 66–87. Springer-Verlag, Heidelberg, Germany, 2003.

[NVT20] Hossein Noorazar, Kevin R Vixie, Arghavan Talebanpour, and Yunfeng Hu. "From classical to modern opinion dynamics." *International Journal of Modern Physics C*, **31**(07):2050101, 2020.

[NXX18] Vu Xuan Nguyen, Gaoxi Xiao, Xin-Jian Xu, Guoqi Li, and Zhen Wang. "Opinion formation on multiplex scale-free networks." *Europhysics Letters*, **121**(2):26002, 2018.

[Oli92] Mario J de Oliveira. "Isotropic majority-vote model on a square lattice." *Journal of Statistical Physics*, **66**(1):273–281, 1992.

[Ope17] OpenStreetMap contributors. "Planet dump retrieved from https://planet.osm.org ." https://www.openstreetmap.org, 2017.

[OS88] Stanley Osher and James Sethian. "Fronts propagating with curvature dependent speed: Algorithms based on Hamilton–Jacobi Formulations." *Journal of Computational Physics*, **79**:12–49, 1988.

[Par62] Emanuel Parzen. "On estimation of a probability density function and mode." *The Annals of Mathematical Statistics*, **33**(3):1065–1076, 1962.

[Par21] Christian Parkinson. "A rotating-grid upwind fast sweeping scheme for a class of Hamilton–Jacobi equations." *Journal of Scientific Computing*, **88**(1):13, 2021.

[PCV15] Romualdo Pastor-Satorras, Claudio Castellano, Piet Van Mieghem, and Alessandro Vespignani. "Epidemic processes in complex networks." *Reviews of Modern Physics*, **87**(3):925–979, 2015.

[Pei19] Tiago P Peixoto. "Bayesian stochastic blockmodeling." In Anuška Ferligoj Patrick Doreian, Vladimir Batagelj, editor, *Advances in Network Clustering and Blockmodeling*, pp. 289–332. John Wiley & Sons, Ltd, Hoboken, NJ, 2019.

[Pen21] Kaiyan Peng. "Code — A multilayer network model of the coevolution of the spread of a disease and competing opinions." https://gitlab.com/KaiyanP196/coevolution-disease-and-competing-opinions, 2021.

[Per21] Nicola Perra. "Non-pharmaceutical interventions during the COVID-19 pandemic: A review." *Physics Reports*, **913**:1–52, 2021.

[Pfa99] Alexander S P Pfaff. "What drives deforestation in the Brazilian Amazon? Evidence from satellite and socioeconomic data." *Journal of Environmental Economics and Management*, **37**(1):26–43, 1999.

[PG16] Mason A Porter and James P Gleeson. *Dynamical Systems on Networks: A Tutorial*, volume 4. Springer International Publishing, Cham, Switzerland, 2016. Frontiers in Applied Dynamical Systems: Reviews and Tutorials.

[PHP20] A Roxana Pamfil, Sam D Howison, and Mason A Porter. "Inference of edge correlations in multilayer networks." *Physical Review E*, **102**(6):062307, 2020.

[PKI22] Antonio F Peralta, János Kertész, and Gerardo Iñiguez. "Opinion dynamics in social networks: From models to data." *arXiv preprint arXiv:2201.01322*, 2022.

[PLL21] Kaiyan Peng, Zheng Lu, Vanessa Lin, Michael R Lindstrom, Christian Parkinson, Chuntian Wang, Andrea L Bertozzi, and Mason A Porter. "A multilayer network model of the coevolution of the spread of a disease and competing opinions." *Mathematical Models and Methods in Applied Sciences*, **31**(12):2455–2494, 2021.

[PM05] Luiz FC Pereira and FG Brady Moreira. "Majority-vote model on random graphs." *Physical Review E*, **71**(1):016123, 2005.

[POM09] Mason A Porter, Jukka-Pekka Onnela, and Peter J Mucha. "Communities in networks." *Notices of the AMS*, **56**(9):1082–1097, 2009.

[PY18] Yaohui Pan and Zhijun Yan. "The impact of multiple information on coupled awareness–epidemic dynamics in multiplex networks." *Physica A: Statistical Mechanics and its Applications*, **491**:45–54, 2018.

[PZ21] Xiao-Long Peng and Yi-Dan Zhang. "Contagion dynamics on adaptive multiplex networks with awareness-dependent rewiring." *Chinese Physics B*, **30**(5):058901, 2021.

[QXU20] Xinwu Qian, Jiawei Xue, and Satish V. Ukkusuri. "Modeling disease spreading with adaptive behavior considering local and global information dissemination." *arXiv preprint arXiv:2008.10853*, 2020.

[Reb13] Fernando Reboredo. "Socio-economic, environmental, and governance impacts of illegal logging." *Environment Systems and Decisions*, **33**(2):295–304, 2013.

[Red19] Sidney Redner. "Reality-inspired voter models: A mini-review." *Comptes Rendus Physique*, **20**(4):275–292, 2019.

[RL08] Wang Ru and Chi Li-Ping. "Opinion dynamics on complex networks with communities." *Chinese Physics Letters*, **25**(4):1502, 2008.

[RPF17] Puck Rombach, Mason A Porter, James H Fowler, and Peter J Mucha. "Core-periphery structure in networks (revisited)." *SIAM Review*, **59**(3):619–646, 2017.

[RPJ16] Francisco A Rodrigues, Thomas K DM Peron, Peng Ji, and Jürgen Kurths. "The Kuramoto model in complex networks." *Physics Reports*, **610**:1–98, 2016.

[RVK16] Gergely Röst, Zsolt Vizi, and István Z Kiss. "Impact of non-Markovian recovery on network epidemics." In *BIOMAT 2015: International Symposium on Mathematical and Computational Biology*, pp. 40–53. World Scientific, 2016.

[Set99] James A Sethian. "Fast marching methods." *SIAM Review*, **41**(2):199–235, 1999.

[SGB17] Michele Starnini, James P Gleeson, and Marián Boguñá. "Equivalence between non-Markovian and Markovian dynamics in epidemic spreading processes." *Physical Review Letters*, **118**(12):128301, 2017.

[SH09] Krzysztof Suchecki and Janusz A Hołyst. "Bistable-monostable transition in the Ising model on two connected complex networks." *Physical Review E*, **80**(3):031110, 2009.

[SLM11] Jeová C Santos, Francisco W S Lima, and Krzysztof Malarz. "Majority-vote model on triangular, honeycomb and Kagomé lattices." *Physica A: Statistical Mechanics and its Applications*, **390**(2):359–364, 2011.

[SLS22] Baike She, Ji Liu, Shreyas Sundaram, and Philip E. Paré. "On a Network SIS Epidemic Model with Cooperative and Antagonistic Opinion Dynamics." *IEEE Transactions on Control of Network Systems*, 2022. 10.1109/TCNS.2022.3145748.

[SM15] Thomas E Stone and Susan R McKay. "Majority-vote model on a dynamic small-world network." *Physica A: Statistical Mechanics and its Applications*, **419**:437–443, 2015.

[SPS13] Hiroki Sayama, Irene Pestov, Jeffrey Schmidt, Benjamin James Bush, Chun Wong, Junichi Yamanoi, and Thilo Gross. "Modeling complex systems with adaptive networks." *Computers & Mathematics with Applications*, **65**(10):1645–1664, 2013.

[SR51] Ray Solomonoff and Anatol Rapoport. "Connectivity of random nets." *The Bulletin of Mathematical Biophysics*, **13**(2):107–117, 1951.

[SSL19] Piotr Sapiezynski, Arkadiusz Stopczynski, David Dreyer Lassen, and Sune Lehmann. "Interaction data from the copenhagen networks study." *Scientific Data*, **6**:315, 2019.

[STK11] Péter L Simon, Michael Taylor, and István Z Kiss. "Exact epidemic models on graphs using graph-automorphism driven lumping." *Journal of Mathematical Biology*, **62**(4):479–508, 2011.

[STS08] Hans-Ulrich Stark, Claudio J Tessone, and Frank Schweitzer. "Decelerating microdynamics can accelerate macrodynamics in the voter model." *Physical Review Letters*, **101**(1):018701, 2008.

[STW06] Michael Small, Chi Kong Tse, and David M Walker. "Super-spreaders and the rate of transmission of the SARS virus." *Physica D: Nonlinear Phenomena*, **215**(2):146–158, 2006.

[SV00] James A Sethian and Alexander Vladimirsky. "Fast methods for the Eikonal and related Hamilton–Jacobi equations on unstructured meshes." *Proceedings of the National Academy of Sciences of the United States of America*, **97**(11):5699–5703, 2000.

[SV03] James A Sethian and Alexander Vladimirsky. "Ordered upwind methods for static Hamilton–Jacobi equations: Theory and algorithms." *SIAM Journal on Numerical Analysis*, **41**(1):325–363, 2003.

[SVB11] Juliette Stehlé, Nicolas Voirin, Alain Barrat, Ciro Cattuto, Vittoria Colizza, Lorenzo Isella, Corinne Régis, Jean-François Pinton, Nagham Khanafer, Wouter Van den Broeck, et al. "Simulation of an SEIR infectious disease model on the dynamic contact network of conference attendees." *BMC Medicine*, **9**(1):87, 2011.

[SVB21] Massimo Stella, Michael S. Vitevitch, and Federico Botta. "Cognitive networks identify the content of English and Italian popular posts about COVID-19 vaccines: Anticipation, logistics, conspiracy and loss of trust." *arXiv preprint arXiv:2103.15909*, 2021.

[SVC19] Paulo Cesar Ventura da Silva, Fátima Velásquez-Rojas, Colm Connaughton, Federico Vazquez, Yamir Moreno, and Francisco A Rodrigues. "Epidemic spreading with awareness and different timescales in multiplex networks." *Physical Review E*, **100**(3):032313, 2019.

[SVV16] Clara Stegehuis, Remco Van Der Hofstad, and Johan SH Van Leeuwaarden. "Epidemic spreading on complex networks with community structures." *Scientific Reports*, **6**:29748, 2016.

[TCO03] Yen-Hsi Richard. Tsai, Li-Tien. Cheng, Stanley. Osher, and Hong-Kai. Zhao. "Fast sweeping algorithms for a class of Hamilton–Jacobi equations." *SIAM Journal on Numerical Analysis*, **41**(2):673–694, 2003.

[TF20] Paulo Trevisani and Juan Forero. "Illegal loggers undercut Brazil forest efforts." *The Wall Street Journal*, p. 18, Oct 2020.

[Tsi95] John N Tsitsiklis. "Efficient algorithms for globally optimal trajectories." *IEEE Transactions on Automatic Control*, **40**(9):1528–1538, Sep 1995.

[VC12] Piet Van Mieghem and Eric Cator. "Epidemics in networks with nodal self-infection and the epidemic threshold." *Physical Review E*, **86**(1):016116, 2012.

[VKR03] Federico Vazquez, Paul L Krapivsky, and Sidney Redner. "Constrained opinion dynamics: Freezing and slow evolution." *Journal of Physics A: Mathematical and General*, **36**(3):L61, 2003.

[Von10] Heinrich Von Stackelberg. *Market Structure and Equilibrium*. Springer, Berlin, Heidelberg, 2010.

[VPD21] André L M Vilela, Luiz Felipe C Pereira, Laercio Dias, H Eugene Stanley, and Luciano R da Silva. "Majority-vote model with limited visibility: An investigation into filter bubbles." *Physica A: Statistical Mechanics and its Applications*, **563**:125450, 2021.

[VVC20] Fátima Velásquez-Rojas, Paulo Cesar Ventura, Colm Connaughton, Yamir Moreno, Francisco A Rodrigues, and Federico Vazquez. "Disease and information spreading at different speeds in multiplex networks." *Physical Review E*, **102**(2):022312, 2020.

[VWB16] Frederik Verelst, Lander Willem, and Philippe Beutels. "Behavioural change models for infectious disease transmission: A systematic review (2010–2015)." *Journal of The Royal Society Interface*, **13**(125):20160820, 2016.

[VWN19] André LM Vilela, Chao Wang, Kenric P Nelson, and H Eugene Stanley. "Majority-vote model for financial markets." *Physica A: Statistical Mechanics and its Applications*, **515**:762–770, 2019.

[WAW15] Zhen Wang, Michael A Andrews, Zhi-Xi Wu, Lin Wang, and Chris T Bauch. "Coupled disease–behavior dynamics on complex networks: A review." *Physics of Life Reviews*, **15**:1–29, 2015.

[WH10] Zhi-Xi Wu and Petter Holme. "Majority-vote model on hyperbolic lattices." *Physical Review E*, **81**(1):011133, 2010.

[WL08] Xiaoyan Wu and Zonghua Liu. "How community structure influences epidemic spread in social networks." *Physica A: Statistical Mechanics and its Applications*, **387**(2-3):623–630, 2008.

[WMA13] Lilian Weng, Filippo Menczer, and Yong-Yeol Ahn. "Virality prediction and community structure in social networks." *Scientific Reports*, **3**:2522, 2013.

[WTY14] Wei Wang, Ming Tang, Hui Yang, Younghae Do, Ying-Cheng Lai, and GyuWon Lee. "Asymmetrically interacting spreading dynamics on complex layered networks." *Scientific Reports*, **4**:5097, 2014.

[WXL12] Yubo Wang, Gaoxi Xiao, and Jian Liu. "Dynamics of competing ideas in complex social systems." *New Journal of Physics*, **14**(1):013015, 2012.

[YFT14] Rong Yang, Benjamin Ford, Milind Tambe, and Andrew Lemieux. "Adaptive resource allocation for wildlife protection against illegal poachers." In *Proceedings of the 13th International Conference on Autonomous Agents and Multiagent Systems*, 2014.

[YKK08] Jae-Suk Yang, In-mook Kim, and Wooseop Kwak. "Existence of an upper critical dimension in the majority voter model." *Physical Review E*, **77**(5):051122, 2008.

[YPH21] Kai-Cheng Yang, Francesco Pierri, Pik-Mai Hui, David Axelrod, Christopher Torres-Lugo, John Bryden, and Filippo Menczer. "The COVID-19 infodemic: Twitter versus Facebook." *Big Data & Society*, **8**(1):20539517211013861, 2021.

[YZR20] Yang Ye, Qingpeng Zhang, Zhongyuan Ruan, Zhidong Cao, Qi Xuan, and Daniel Dajun Zeng. "Effect of heterogeneous risk perception on information diffusion, behavior change, and disease transmission." *Physical Review E*, **102**(4):042314, 2020.

[YZR21] Mengbin Ye, Lorenzo Zino, Alessandro Rizzo, and Ming Cao. "Game-theoretic modeling of collective decision making during epidemics." *Physical Review E*, **104**(2):024314, 2021.

[Zar20] John Zarocostas. "How to fight an infodemic." *The Lancet*, **395**(10225):676, 2020.

[Zha05] Hongkai Zhao. "A fast sweeping method for Eikonal equations." *Mathematics of Computation*, **74**(250):603–627, 2005.

[Zha07] Hongkai Zhao. "Parallel implementations of the fast sweeping method." *Journal of Computational Mathematics*, pp. 421–429, 2007.

[ZLL20] Juanjuan Zhang, Maria Litvinova, Yuxia Liang, Yan Wang, Wei Wang, Shanlu Zhao, Qianhui Wu, Stefano Merler, Cécile Viboud, Alessandro Vespignani, Marco Ajelli, and Hongjie Yu. "Changes in contact patterns shape the dynamics of the COVID-19 outbreak in China." *Science*, **368**(6498):1481–1486, 2020.

[ZOM00] Hong-Kai Zhao, Stanley Osher, Barry Merriman, and Myungjoo Kang. "Implicit and nonparametric shape reconstruction from unorganized data using a variational level set method." *Computer Vision and Image Understanding*, **80**(3):295–314, 2000.